GREEN WATER FLOW KINEMATICS AND IMPACT PRESSURE ON A THREE DIMENSIONAL MODEL STRUCTURE

A Dissertation

by

HANCHAPOLA APPUHAMILAGE KUSALIKA SURANJANI ARIYARATHNE

Submitted to the Office of Graduate Studies of
Texas A&M University
in partial fulfillment of the requirements for the degree of

DOCTOR OF PHILOSOPHY

August 2011

Major Subject: Civil Engineering

Green Water Flow Kinematics and Impact Pressure on a Three Dimensional Model Structure

GREEN WATER FLOW KINEMATICS AND IMPACT PRESSURE ON A THREE DIMENSIONAL MODEL STRUCTURE

A Dissertation

by

HANCHAPOLA APPUHAMILAGE KUSALIKA SURANJANI ARIYARATHNE

Submitted to the Office of Graduate Studies of
Texas A&M University
in partial fulfillment of the requirements for the degree of

DOCTOR OF PHILOSOPHY

Approved by:

Chair of Committee,	Kuang-An Chang
Committee Members,	Richard Mercier
	Hamn-Ching Chen
	Achim Stossel
Head of Department,	John Niedzwecki

August 2011

Major Subject: Civil Engineering

ABSTRACT

Green Water Flow Kinematics and Impact Pressure on a Three Dimensional Model Structure.

(August 2011)

Hanchapola Appuhamilage Kusalika Suranjani Ariyarathne,

B.S.; M.S., University of Peradeniya; M.S., Texas A&M University

Chair of Advisory Committee: Dr. Kuang-An Chang

Flow kinematics of green water due to plunging breaking waves interacting with a simplified, three-dimensional model structure was investigated in the laboratory. Two breaking wave conditions were tested: one with waves impinging and breaking on the vertical wall of the model at the still water level and the other with waves impinging and breaking on the horizontal deck surface. The Bubble Image Velocimetry (BIV) technique was used to measure the flow velocity. Measurements were taken on a vertical plane located at the center of the deck surface and a horizontal plane located slightly above the deck surface.

The evolution of green water flow kinematics in time and space is revealed in the study. It was observed that the maximum velocity appears near the green water wave front and is 1.44C with C being the wave phase speed for the deck impingement case and 1.24C for wall impingement case. The velocity variations in the present study were compared with that in an earlier study using a two-dimensional model with the same

wave condition as in the wall impingement condition. The applicability of dam-break theory on green water velocity prediction for the three-dimensional model was also investigated.

Furthermore, pressure measurements were performed at two vertical planes: one at the centre and the other at 0.05 m away from the centre. Ensemble averaged pressure variations were compared. Impact pressure was successfully related to the pressure rising time. Void fraction was measured for few locations near the model front edge. After correcting the density considering void ratio, predictions of maximum impact pressure based on the measured pressure and flow velocity were investigated linking pressure with kinetic energy. It was also found that there is a linear relationship between the rising pressure gradient and the impact coefficient.

DEDICATION

With Love and Respect,

To My Family Members: Father, Mother, Husband and Two Sisters.

ACKNOWLEDGEMENTS

The following is my heartfelt appreciation to all those who gave me inspiration, advice, direction and insight to begin, continue and complete my Ph.D. studies.

I would like to express my deep gratitude to my advisor, Dr. Kuang-An Chang, for his guidance, advice, continuous support, encouragement, patience and understanding at all times.

I would like to thank Dr. Richard Mercier, Dr. Hamn-Ching Chen and Dr. Achim Stossel for serving as committee and for their guidance and support throughout the course of this research.

Thanks also go to Dr. Yong-Uk Ryu, Dr. Ho-Joon Lim, Arthur Antoine and John Reed for their support while working in the lab.

Thanks go to all colleagues for making my time at Texas A&M University a great experience.

I wish to thank the Sri Lanka President's Fund for providing financial support for my living expenses.

I would like to extend my deep gratitude to my father, mother, and two sisters for their love and relentless support from oversees.

Finally, thanks to my husband, R.T. Amarasinghe, for his love, patience, understanding, kind support, encouragement, and for making this work interesting and a success.

TABLE OF CONTENTS

Page

LIST OF FIGURES

Page

Page

Page

LIST OF TABLES

CHAPTER I

INTRODUCTION AND LITERATURE REVIEW*

Interactions between extreme waves and offshore structures are of primary interest to ocean and coastal engineers. In heavy storm conditions wave heights increase. If wave heights reach above the free board, waves overtop the structure and form green water. Green water may cause stability, integrity, safety and operability failures to offshore structures. In most offshore structures, facilities and equipment are located on the deck. It is thus important to study the green water flow. Due to the severity of recent hurricanes, such as Hurricanes Ivan, Rita, and Katrina in the Gulf of Mexico, and the popularity of permanently moored offshore structures, the importance of understanding green water phenomena is heightened.

This dissertation follows the style of Coastal Engineering.

* Part of the data reported in this chapter is reprinted with permission from "Three-dimensional green water velocity on a model structure" by Chang, Ariyarathne and Mercier (2011). Experiments in Fluids, DOI: 10.1007/s00348-011-1051-0, Copyright [2011] Springer.

The green water problem has been studied both numerically and experimentally for decades. Most of these studies are limited to motions (surge, heave, and pitch), impact loads, and probability of deck wetness. It is very difficult to simulate the flow due to its multiphase and turbulent nature. Similarly, in most laboratory work measurements were limited to wave height and pressure with few reports providing flow velocity field measurements.

Buchner (1995a,b) conducted an experimental investigation on the effect of green water on Floating Production Storage and Offloading (FPSO) units. Occurrence of green water due to the influence of wave height, wave period, and current velocity, and related design aspects of FPSOs were discussed. Relation between relative motion and deck wetness, behavior and loading of green water on the deck, and impact loading on deck structures were also investigated. He identified the sequence of green water occurrence as: the relative wave motions around the bow, the water flow onto the deck, the shallow water wave over the deck, and the final impact of the water to the structure. Furthermore, he mentioned that the dynamic pressure is contributed from the vertical acceleration and rate of change of water height. Design aspects in terms of influence of the bow shape, position of equipments on deck, and shape of break waters were also discussed. Buchner (1996) later discussed the influence of the bow shape of FPSO on the drift force and green water loading. A traditional tanker bow, a sharp alternated bow without flare, and the same alternated bow with a significant flare above the still waterline were tested. He concluded that the mean wave drift force and low frequency drift force are smaller for the sharper alternated bows if compared to the traditional bow.

However, the relative motion around the bow is the largest for alternated bows, hence more water flows on to the deck. He further concluded that the impact pressure is significantly higher for the alternated bow.

Hamoudi and Varyani (1998) performed laboratory tests and investigated the probability of green water occurrence as a function of Froude number and significant wave height. Wan and Wu (1999) developed a numerical model to investigate two-dimensional (2D) green water flows. In their model a longitudinal section of a typical ship was considered. Navier-Stokes equations were solved with fully non-linear boundary condition on the free surface, and the evolution of free surface was solved by the volume of fluid (VOF) method. The analysis allows the waves to overturn and break. Results were given for velocity, elevation, and pressure along a vertical section at the deck center. Fekken et al. (1999) developed a numerical model to solve Navier-Stokes equations with three-dimensional (3D) cartesian grid. The VOF method was used to track the free surface. Green water loading on the foredeck of a ship, water heights, pressure, and water contour forces on different structures placed on the deck were produced and compared to experimental results.

Cox and Scott (2001) conducted laboratory measurements to examine the instantaneous free surface elevation, velocity, and overtopping rate at the leading edge of a model deck. Based on experimental results the probability distributions of the extreme water level and wave overtopping rate were obtained, and theory for statistics of extreme wave crests was developed. Subsequently, Cox and Ortega (2002) quantified wave overtopping a horizontally fixed deck surface above the free surface level based on

laboratory experiments. Free surface and velocity measurements were taken for the conditions with and without the deck to examine the effects of deck surface on flow kinematics. It was observed that both the free surface above the leading edge and maximum horizontal velocity increase with the existence of the deck. Moreover, Mori and Cox (2003) developed a statistical model for predicting the wave overtopping volume and rate of extreme waves on a fixed deck.

Schonberg and Rainey (2002) developed a numerical model based on the potential flow assumption to calculate velocity of water on the deck area. The model simulates a shelf submerging into a pool. The resulting flow was modeled using a desingularized boundary integral equation method combined with an implicit time stepping algorithm. Faltinsen et al. (2002) developed a numerical model to predict green water loading and investigated the influencing factors on green water loading. The use of dam-break model in green water predictions was also discussed.

Nielsen and Mayer (2004) developed a numerical model employing a Navier-Stokes solver and a free surface capturing scheme to model green water loads on a moored FPSO exposed to head sea waves. Green water on a fixed vessel and a moving vessel was investigated, and the water height on the deck and impact pressure were obtained. Kleefsman et al. (2005) developed a numerical model to estimate green water load. The model is based on Navier-Stokes equations, and the equations were discretized using the finite volume method. The predictions of water surface, pressure, and velocity were compared with experimental data, and the model was successfully validated with the laboratory data for wave elevation and impact pressure. Xu et al. (2008) performed

an experimental investigation on wave impact and dynamic response on a FPSO. Xu and Barltrop (2008) later developed a numerical model to calculate the impact load.

Even though the green water problem has been studied for a long time, there are not many studies focusing on flow kinematics. Among those, most are numerical studies based on linear wave theory and single phase assumption. The multiphase, turbulent nature of green water flow is therefore not realistically simulated. Bubble formation and defragmentation in highly nonlinear multiphase green water continue to pose great challenges to numerical modeling. Lack of laboratory data on green water flow velocities for validation of numerical models also hinders progress.

Not only does bubble formation challenge numerical modeling of flow kinematics, it also causes problems in experimental measurements. Available methods such as Acoustic Doppler Velocimetry (ADV), Laser Doppler Velocimetry (LDV), and Particle Image Velocimetry (PIV) are incapable of measuring highly aerated flow due to uncontrollable acoustic and laser scattering caused by bubbles.

Ryu et al. (2005) recently developed and successfully applied a technique called Bubble Image Velocimetry (BIV) that combines PIV and the shadowgraphy method for velocity measurement in aerated regions of multiphase flow. Instead of correlating images of small seeding particles as in the traditional PIV technique, the BIV technique obtains velocity by correlating the "texture" in images created by bubbles and air-water interfaces. The technique has been validated using velocities measured by Fiber Optics Reflectometer (FOR) developed by Chang et al. (2003).

Using BIV, Ryu et al. (2007a) performed an experimental study to measure the

green water velocity on a 2D model structure due to a plunging breaking wave impact. Flow kinematics and turbulence properties were examined, and a similarity model for the green water velocity distribution was developed. Based on the measured velocity distribution, Ryu et al. (2007b) examined the applicability of dam-break theory for predicting the horizontal velocity of green water over the deck. Moreover, Ryu and Chang (2008) measured the void fraction in the green water flow using FOR. Based on the void ratio they examined the flow rate, momentum flux, and water volume of the overtopping flow.

All studies mentioned above are relevant for understanding the green water phenomenon. However, clear conclusions have not been available, and some studies are in contradiction with others due to the involved parameters. In this regard, experimental studies would play a fundamental role in verification. The most common way of analyzing green water events is to apply probability analysis with linear wave theory. The relative vertical motion is a main parameter which decides the green water occurrence. In calculating the relative motion, in most studies the incident wave height is used but not the local wave height, while the structure's vertical motion (heave) and the ship speed are not considered. Using linear wave theory completely omits the turbulent and highly nonlinear green water nature. So far, there is no reliable theoretical method for predicting the height of water on deck and water particle velocities across the deck.

The objective of the present study is to investigate the flow kinematics of a plunging wave breaking and impinging on a 3D model structure in the laboratory. Velocities of green water due to breaking waves were measured using the BIV

technique. Two different wave impact conditions were selected. Velocity measurements were taken on both a horizontal plane and a vertical plane. Ensemble averaged velocity fields were obtained from repeated measurements. The time history of maximum velocity in the green water flow was analyzed and compared. Application of dam-break theory for predicting the horizontal flow velocity over the deck surface was examined. The present velocity measurements on the 3D structure were compared with that measured on a similar two-dimensional structure.

Pressure measurements were also taken for both wave conditions. Ensemble averaged pressure variations in time and space were examined. The maximum impact pressure was successfully related to the rise time. Void fraction was measured using FOR technique. After corrections were made for the flow density, possibility of predicting the maximum impact pressure using the measured velocity was investigated.

In this report, the experimental setup and conditions for flow kinematics measurements are presented in Chapter II. Details of flow kinematics are discussed in Chapter III. Application of dam-break theory to predict the green water velocity is presented in Chapter IV. Measurement of green water impact pressure and void ratio, comparison of the spatial and temporal variations of these parameters, and relating impact pressure with velocity are discussed in Chapter V. Chapter VI concludes the study.

CHAPTER II

EXPERIMENTAL SETUP*

Laboratory experiments were conducted in a glass-walled tank located at Zachry Department of Civil Engineering at Texas A&M University. The wave tank is 36 m long, 0.9 m wide and 1.5 m deep. The wave generator is a Sea Sim Rolling Seal absorbing wavemaker (RSW 90-85). It is a dry back, aluminum space frame, and PVC cased, modular, hinged flap type. The flap is sealed by a low friction rolling seal and is driven by a precision, electronically commutated synchronous servo meter, while being hydrostatically balanced using an automatic near constant force, pneumatic control system (Sea Sim Rolling Seal Absorbing Wavemaker manual, data sheet RSW 382). The wavemaker was controlled by a computer equipped with a National Instruments AT-MIO-16E-2 data acquisition board and an in-house developed National Instruments LabVIEW program. There is a 1:5.5 sloping beach at the other end of the tank with a layer of horsehair to absorb the wave energy and to reduce wave reflection. Water depth was kept constant at 0.80 m throughout the tests. Fig. 2.1 shows a schematic sketch of the experimental setup.

---

* Part of the data reported in this chapter is reprinted with permission from "Three-dimensional green water velocity on a model structure" by Chang, Ariyarathne and Mercier (2011). Experiments in Fluids, DOI: 10.1007/s00348-011-1051-0, Copyright [2011] Springer.

The breaking waves were generated by using the wave focusing technique, the waves are consisted of a train of waves of various frequencies and amplitudes. The wave focusing method generates short waves followed by long waves; the faster moving longer waves catch up with the slower moving shorter waves at a desired location and form the breaking waves. The characteristics of the breaking waves were controlled by modification of the software input parameters in the LabVIEW signal diver program. Waves were generated by a DC voltage analog output signal sent by the signal driver.

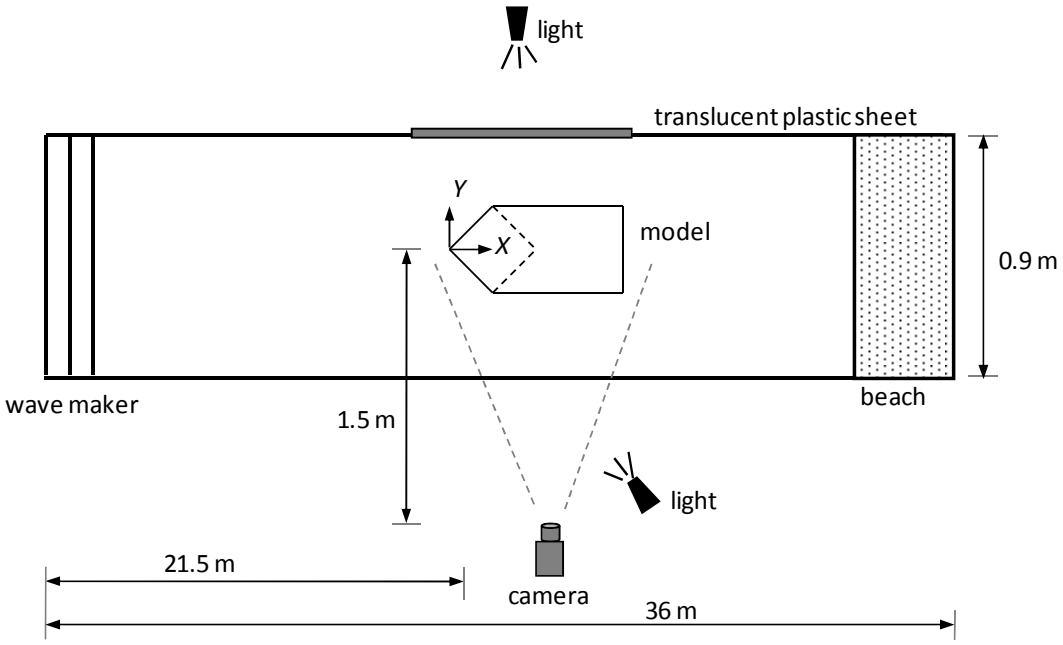

Fig. 2.1. Experimental setup (top view, not to scale).

A simplified 1:169 scale model structure that may be considered as a ship bow or a square column of a platform was constructed using Plexiglas and was located at 21.5 m away from the wavemaker. A sketch of the model structure is shown in Fig. 2.2. The model was supported by an aluminum frame which was fixed to the tank bottom. The draft of the model structure is 0.20 m and the freeboard is 0.11 m. The origin of coordinate system (X, Y, Z) = (0, 0, 0) is at the leading edge, centerline, and surface of the deck, respectively, as shown in Fig. 2.2. The still water level is thus at Z = -0.11 m. Two wave conditions were tested: one with breaking waves impinging on the vertical wall of the model at the still water level (hereafter called the *wall impingement* case) and the other with breaking waves impinging on the horizontal deck surface (hereafter called the *deck impingement* case). A schematic of the two wave conditions is shown in Fig. 2.3.

Breaking waves were generated using a wave focusing technique. The waves are nearly identical to that in Ryu et al. (2007a). A wave train that consists of wave components ranging from 0.7 Hz to 1.3 Hz with shorter waves followed by longer waves was generated by the wavemaker. Only one breaking event occurred in the wave train. The breaking waves were carefully controlled so they break at a desired location on the model structure. The breaking waves were designed in such a way that the waves resemble the measured maximum wave in Hurricane Ivan which has a wave height of 27.7 m and a wave period of 16.8 s (Wang et al., 2005). The laboratory generated waves were verified as being highly repeatable.

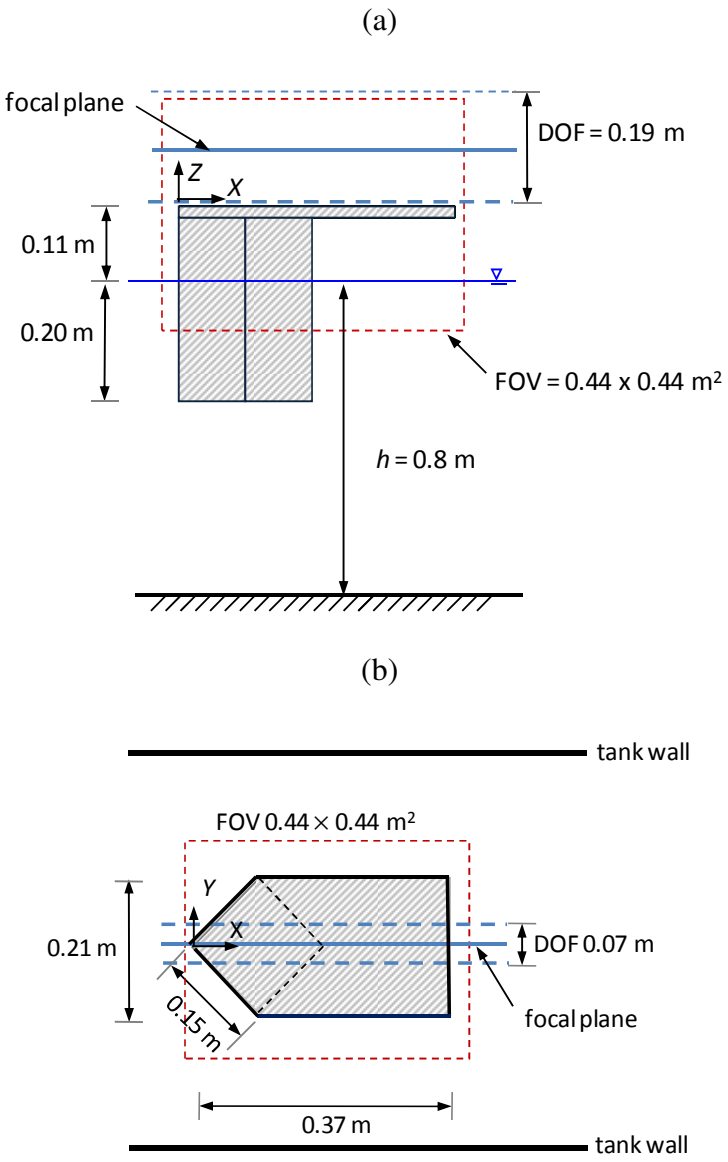

Fig. 2.2. Model structure and FOV: (a) side view with a vertical-plane FOV; (b) top view with a horizontal-plane FOV.

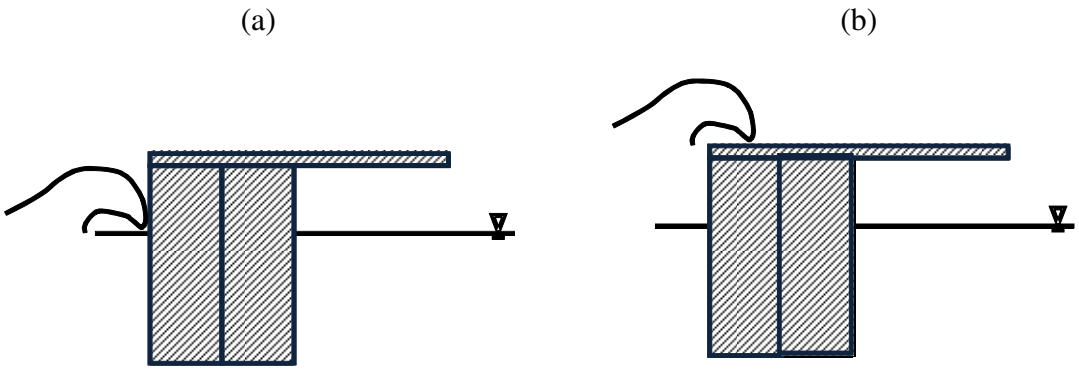

Fig. 2.3. The two test wave conditions: (a) wall impingement case with waves impinging on the vertical wall at the still water level; (b) deck impingement case with waves impinging on the horizontal deck surface.

Control and trigger signals to the wavemaker, the BIV system, the pressure and void ratio sensor control units were created by an in-house developed National Instruments LabVIEW program. This setup synchronizes data acquisition for the systems in the experiment. To ensure repeatability of the test condition, water in the wave tank was allowed to settle for twenty minutes in between test runs.

2.1. Wave elevation measurement

The free surface elevation was measured using double-wired resistance type wave gauges located at 5 m (X = -16.5 m), 15 m (X = -6.5 m), and 21.5 m (at the leading edge of the model structure at X = 0) away from the wavemaker. Water elevation was measured with and without the presence of the model structure. The measured water elevation with the presence of the structure at X = -16.5 m was considered in calculating

incoming wave parameters and at $X = 0$ was considered as the water elevation at the front edge of the model. These wave gauges are more effective in measuring the wave elevation in the non aerated region since they basically measure the total wetted length of the wires that are in contact with water. Signals from the wave gauges were converted to voltage and sent to a data acquisition board. The measured surface elevations for the tested waves are shown in Fig. 2.4 and Fig. 2.5.

The water surface elevation of each wave gauge was recorded at a sampling rate of 25 Hz for a duration of 100 seconds for twenty trials before the ensemble averaged water elevation was calculated. The primary wave period was obtained by zero up crossing. The primary wave is the specific wave in the wave train which has the largest wave amplitude and leads to the breaking event.

The wave period (T), wave height (H), and phase speed (C) for the breaking wave of the wall impingement case are $T = 1.37$ s (equivalent to 17.8 s in prototype based on Froude scaling), $H = 0.17$ m (equivalent to 28.7 m in prototype), and $C = 2.02$ m/s (equivalent to 26.3 m/s or 95 km/hr in prototype). The breaking wave condition for the deck impingement case is nearly identical to that of the wall impingement case with a slight difference of 0.01 s (0.7%) in wave period and 0.02 m/s (1.0%) in phase speed so the wave conditions for the two cases may be considered as identical. They are also considered as identical to that in Ryu et al. (2007a). The wave period is obtained from the zero up-crossings of the free surface record while the phase speed is calculated using the linear dispersion relationship.

If the water elevation measurement measured at X = -16.5 m without the presence of the model structure is used for calculating the incoming parameters, the wave period (T), wave height (H), and phase speed (C) for the breaking wave of the wall impingement case are T = 1.17 s (equivalent to 15.2 s in prototype based on Froude scaling), H = 0.25 m (equivalent to 42.2 m in prototype), and C = 1.79 m/s (equivalent to 23.3 m/s or 84 km/hr in prototype). The breaking wave condition for the deck impingement case is nearly identical to that of the wall impingement case with a slight difference of 0.04 s (3%) in wave period and 0.05 m/s (3.0%) in phase speed so the wave conditions for the two cases may be considered as identical.

As Figs. 2.4 and 2.5 show, the measured surface elevation is almost the same for both with and without the presence of the model structure. However, for the measurements near the model, the time history of the surface elevation is smoother for measurements without the presence of the model structure for both wall impingement and deck impingement waves.

Fig. 2.6 and Fig. 2.7 show the calculated standard deviation for wall impingement and deck impingement waves respectively. Standard deviation was calculated for both measurements with and without the presence of the model structure. As Fig. 2.6 shows, the highest standard deviation of about 0.01 m was observed for wall impingement wave condition, for measurements at X = 0. For the deck impingement wave the highest standard deviation of 0.06 m was observed for measurement at X = 0. For both wall impingement and deck impingement waves, the standard deviation for X = -16.5 is very small, and lies around 0.02 m.

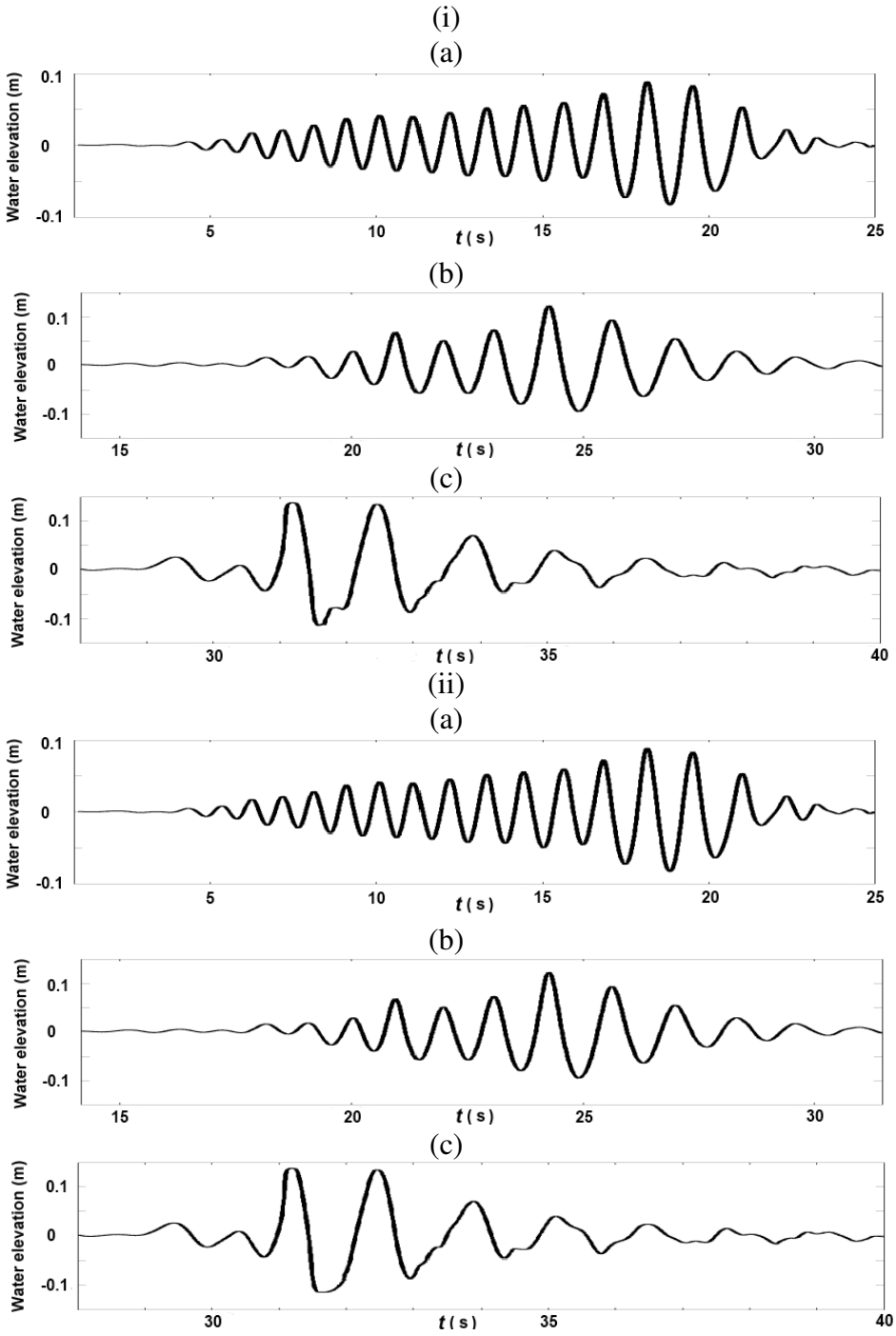

Fig. 2.4. Measured free water elevation for the wall impingement wave. (i) With the model structure, (ii), without the model structure. (a) Close to the wavemaker at X = -16.5 m; (b) at X = -6.5 m (c) at the model at X = 0 m.

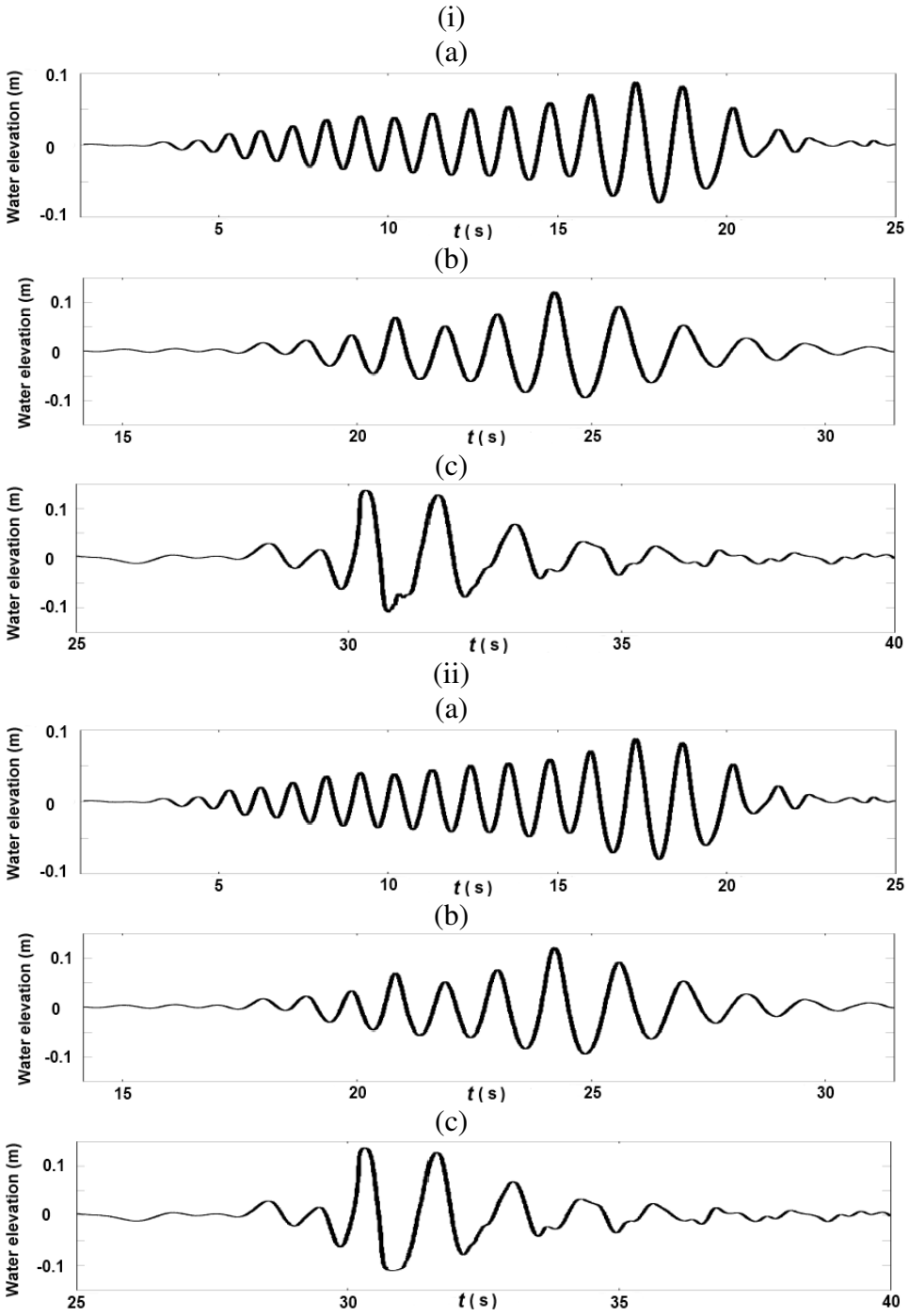

Fig. 2.5. Measured free water elevation for the deck impingement wave. (i) With the model structure, (ii), without the model structure. (a) Close to the wavemaker at X = -16.5 m; (b) at X = -6.5 m (c) at the model at X = 0 m.

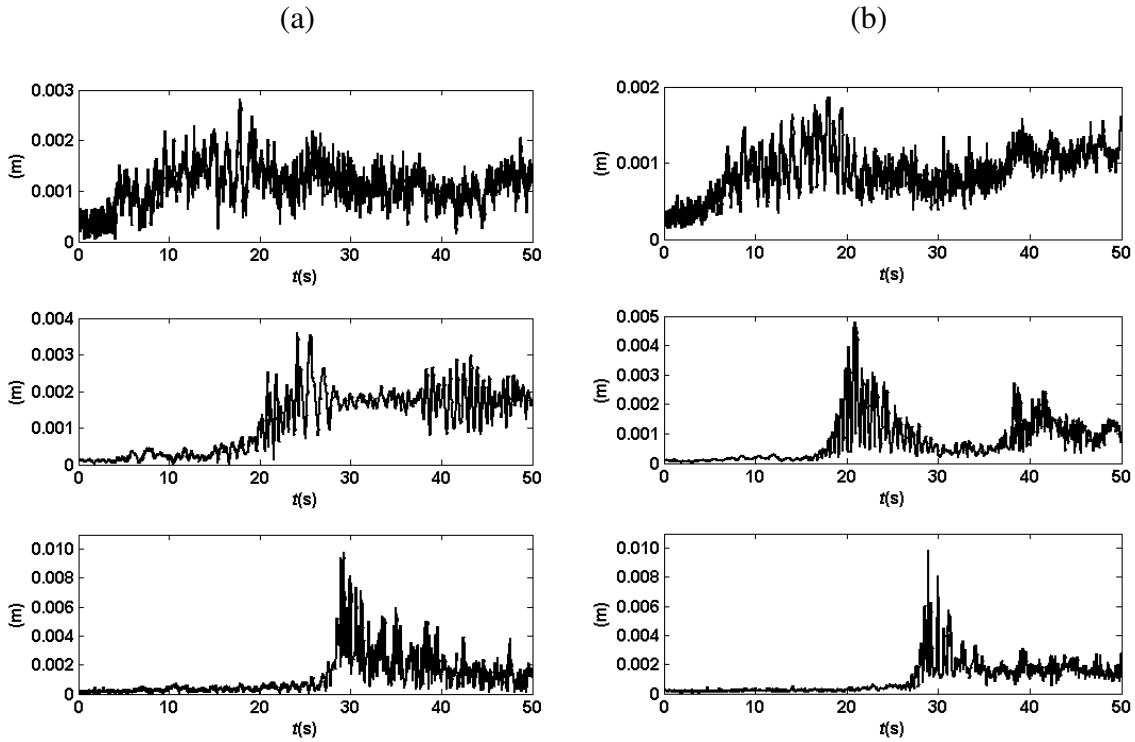

Fig. 2.6. Calculated standard deviation for the wall impingement wave. Upper raw at X = -16.5 m; middle raw at X = -6.5 m; lower raw at the model at X = 0 m. Left column, with the model structure; right column, without the model structure.

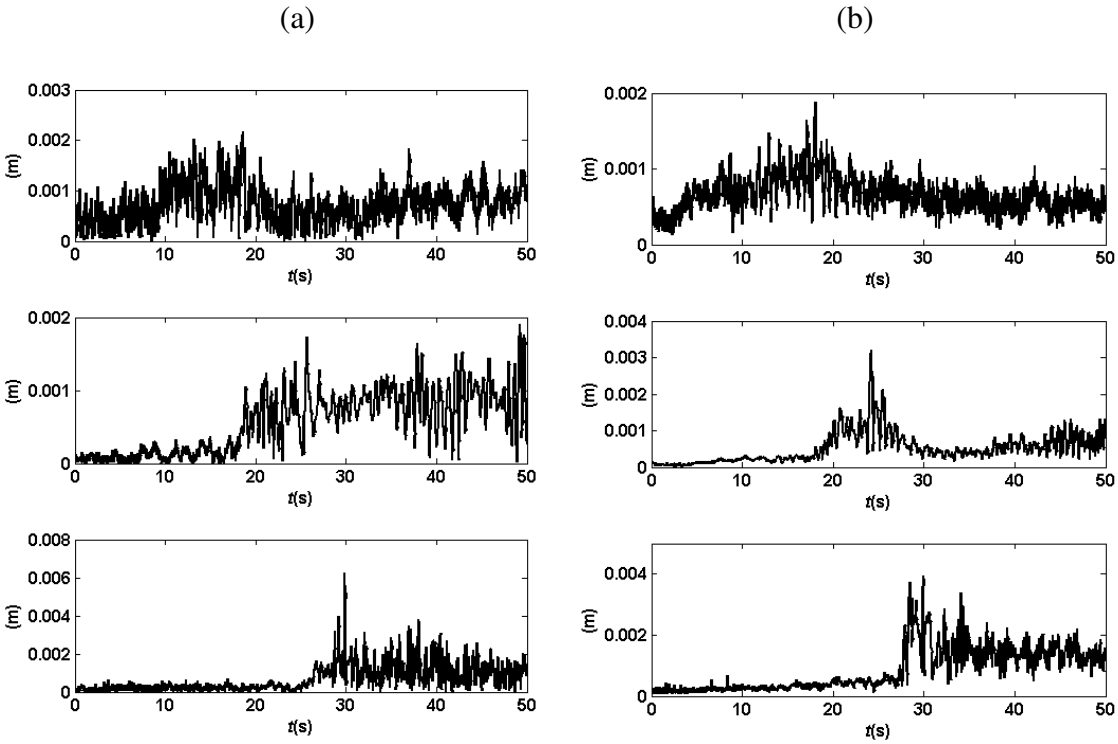

Fig. 2.7. Calculated standard deviation for the deck impingement wave. Upper raw at X = -16.5 m; middle raw at X = -6.5 m; lower raw at the model at X = 0 m. Left column, with the model structure; right column, without the model structure.

2.2. Velocity measurement

The flow became highly turbulent and aerated after the breaking waves impinged on the structure. Conventional methods for velocity measurements like PIV and LDV do not work well in situations with bubble formation. There have been few studies with successful velocity measurements in the aerated region. The BIV technique introduced by Ryu et al. (2005) was used in the present study. The technique combines the PIV and shadowgraphy technique, and correlates images formed by bubbles and air-water interfaces for velocity determination.

Images were captured using a high speed camera (Vision Research, Phantom 5.1) mounted with a Nikon 50 mm focal lens. The camera has a resolution of 1024×1024 pixels, 8 bit dynamic range, and a maximum framing rate of 1200 frames per second (fps). The framing rate was set to 1000 fps throughout the experiment. Flow velocities covering a field of view (FOV) of 0.44×0.44 m^2 were measured on both a vertical plane (side view) along the centerline of the deck surface, and a horizontal plane (plan view) above the deck surface, as illustrated in Fig. 2.2(a) and (b), respectively. For the vertical-plane measurements, flow illumination was achieved by using 600 W lights at the back side of the tank. A thin, white translucent sheet was attached to the back side of the tank wall so the back lit light became more uniform (see Fig. 2.1). For regions with very high bubble concentration, the images may appear as dark. To reduce this effect and to increase the texture in the images, a light was also placed at the front side of the tank with an angle. For the horizontal-plane measurements, the lights were placed on both

sides of the tank facing downward towards to the tank bottom. The reflected light from the white tank bottom created a near uniform back-lit effect that is similar to the illumination in the horizontal plane measurements for BIV image acquisition.

The BIV technique does not require the use of a laser light sheet; the location of the measurement plane was controlled by minimizing the Depth of Field (DOF) in images by adjusting the aperture and the distance between the model and the camera. The DOF is the distance where the captured objects are focused and sharp. According to Ray (2002), the nearest limit is $R = Lf^2 / \left(f^2 + NLC_c \right)$ and farthest limit is $S = Lf^2 / \left(f^2 - NLC_c \right)$, where L is the distance from the camera to the object, f is camera focal length, C_c is circle of confusion, and N is the f-number of the camera aperture. The DOF is $D = S - R$.

In the present study the DOF for the vertical plane measurements was limited to 0.07 m and for the horizontal plane measurements was limited to 0.19 m. They were calculated as below. For the vertical-plane measurements, L = 1.5 m, f = 50 mm, N = 1.4, and C_c = 0.03 mm. The calculated S is about 1.53 m and R is about 1.46 m, therefore the corresponding DOF in the present study is D = 0.07 m. For the horizontal-plane measurements, L = 2.0 m, f = 50 mm, N = 2.0, and C_c = 0.03 mm. The calculated S is about 2.10 m and R is about 1.91 m, therefore the corresponding DOF is D = 0.19 m.

For the vertical-plane measurements, the camera was located 1.5 m in front of the focal plane with the center of the focal plane coincident with the centerline of the model structure. Ryu et al. (2005) concluded that objects located in front and behind the DOF appear as blur and do not affect the velocity calculation. The uncertainty in the location

of bubble images in the cross tank direction is half of the DOF, hence the error due to limited thickness of DOF in the velocity measurements is $D/2L$. For the horizontal-plane measurements, the camera was located 2.0 m above the deck surface with the center of the focal plane at Z = 0.10 m. Due to wave motion in the vertical direction, the DOF was limited to 0.19 m, as indicated in Fig. 2.2(a). The calculated uncertainties as of the measured velocities due to the limited thickness of the DOF are 2.3% and 4.8% for the vertical plane and horizontal plane velocity measurements, respectively. Note that certain effects that result in only out of focus images (but without in-focus images) and cause a greater or unknown uncertainty in some measurement areas will be specifically pointed out in the study.

Commercial software from La Vision Inc. and MPIV software developed by Mori and Chang (2003) were used to analyze BIV images and obtain velocity vectors. An adaptive multi-pass algorithm with an initial window size of 64×64 pixels and a final window size of 32×32 pixels was employed with 50% overlap between adjacent windows. For the second pass with window shift, the calculated velocity in the first pass was used, hence improving the signal to noise ratio. Raw images were first inverted so that high intensity (bright) represents bubbles. Cross correlation was then applied to compute velocity vectors. Fig. 2.8 demonstrates the procedure. Note that the BIV technique does not work in the areas where there are no bubbles or air-water interfaces. The technique captures the wave front velocity well, which is typically the maximum velocity. For each wave condition, measurements were repeated 30 times with identical initial and boundary conditions. Mean velocities were calculated by ensemble averaging

the 30 instantaneous velocities obtained from the 30 repeated measurements. A median filter was used to remove spurious vectors, and Kriging interpolation was applied to fill the removed vectors.

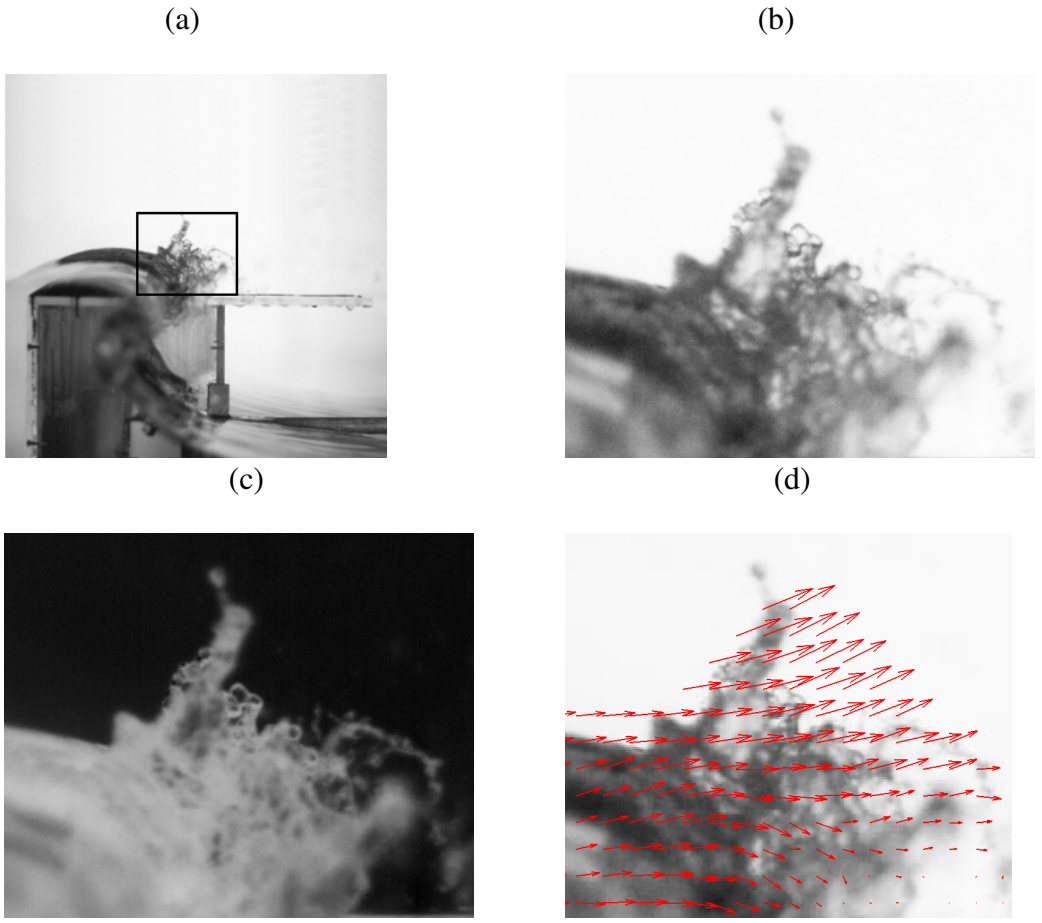

Fig. 2.8. Velocity determination in the BIV technique. (a-b) Original image and its close up, (c) inverted image, (d) calculated velocity.

CHAPTER III

GREEN WATER FLOW KINEMATICS*

3.1. Flow kinematics - wall impingement case

Flow fields and evolution of the wall impingement case are demonstrated in Figs. 3.1 and 3.2 for the vertical-plane (side view) and horizontal-plane (top view) mean velocities, respectively. The left column shows normalized velocity vectors whereas the right column shows velocity contours, normalized by the phase speed C. The location of the maximum velocity can thus be identified from the right column. Note that the velocity fields are the ensemble averaged mean velocities using 30 repeated instantaneous velocity measurements, while the background images were arbitrarily selected from one of the 30 realizations. The time $t = 0$ was defined as the moment when the wave front crosses $X = 0$ at the leading vertical front wall.

---

* Part of the data reported in this chapter is reprinted with permission from "Three-dimensional green water velocity on a model structure" by Chang, Ariyarathne and Mercier (2011). Experiments in Fluids, DOI: 10.1007/s00348-011-1051-0, Copyright [2011] Springer.

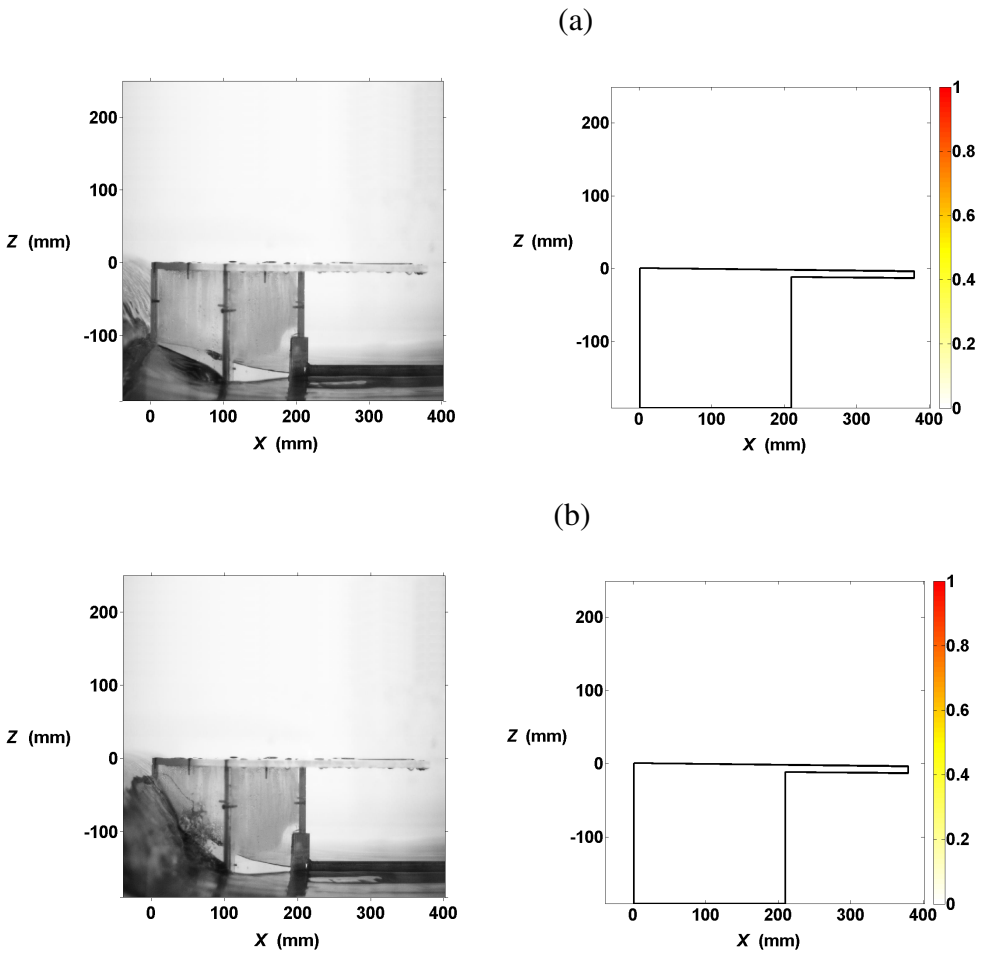

Fig. 3.1. Mean velocity fields on the vertical plane for the wall impingement case at t = (a) 0.000 s, (b) 0.025 s, (c) 0.050 s, (d) 0.075 s, (e) 0.100 s, (f) 0.125 s, (g) 0.150 s, (h) 0.175 s, (i) 0.200 s, (j) 0.225 s, (k) 0.250 s, (l) 0.275 s. Left column: normalized velocity (normalized using phase velocity, C) vectors; right column: velocity contours. The scale of the contour color bar is C.

(c)

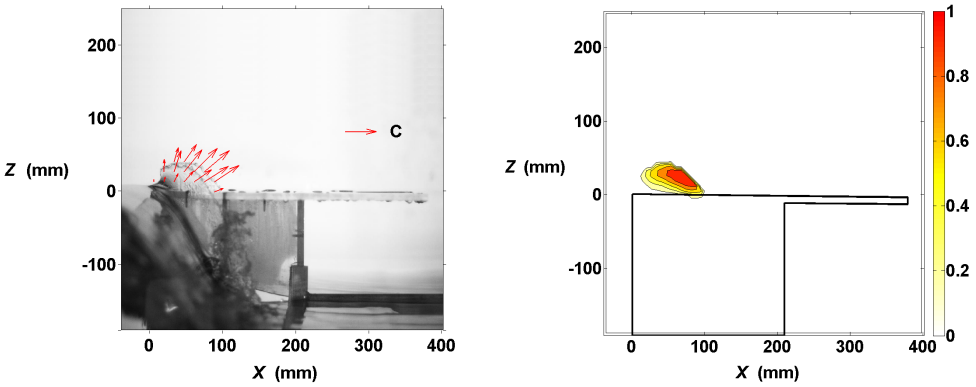

(d)

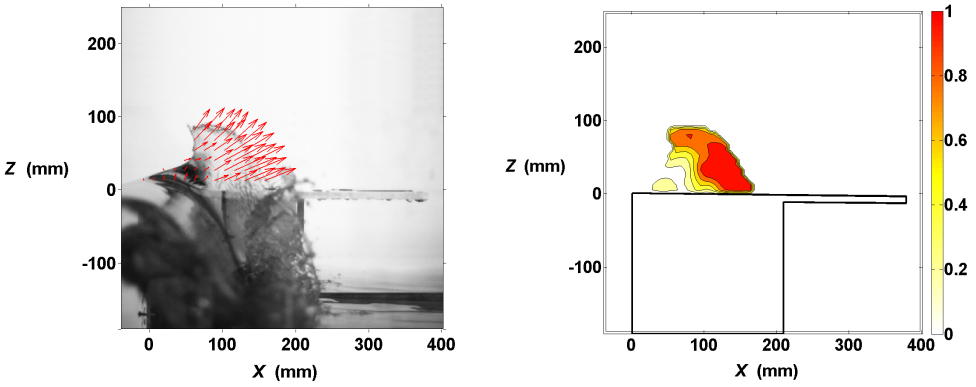

(e)

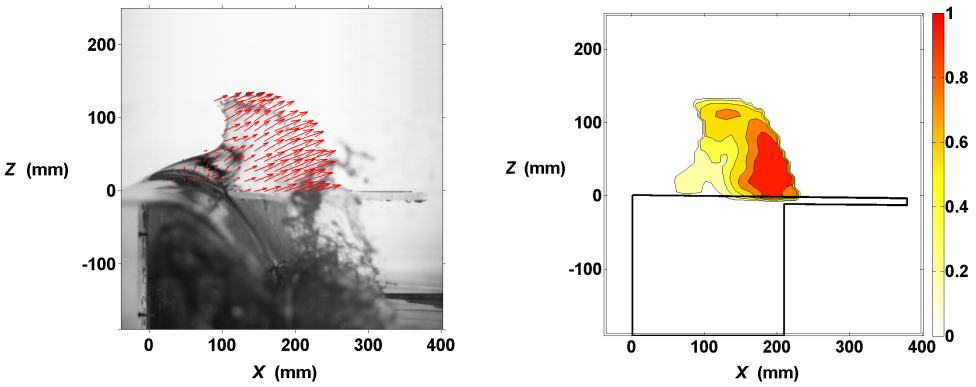

Fig. 3.1 continued.

(f)

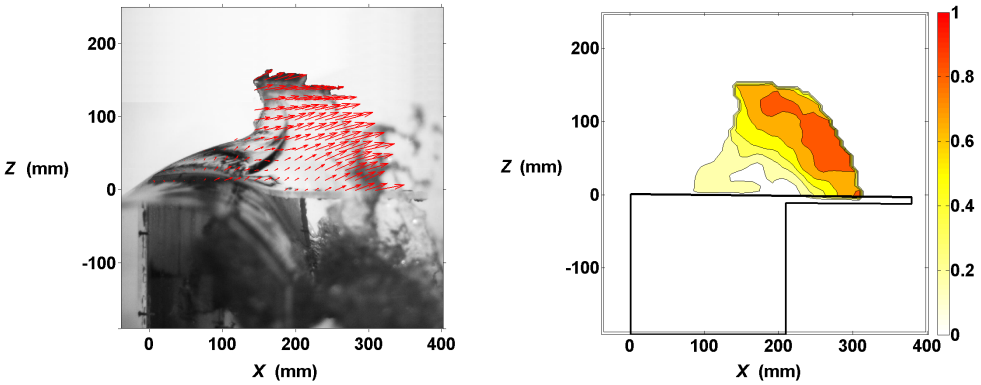

(g)

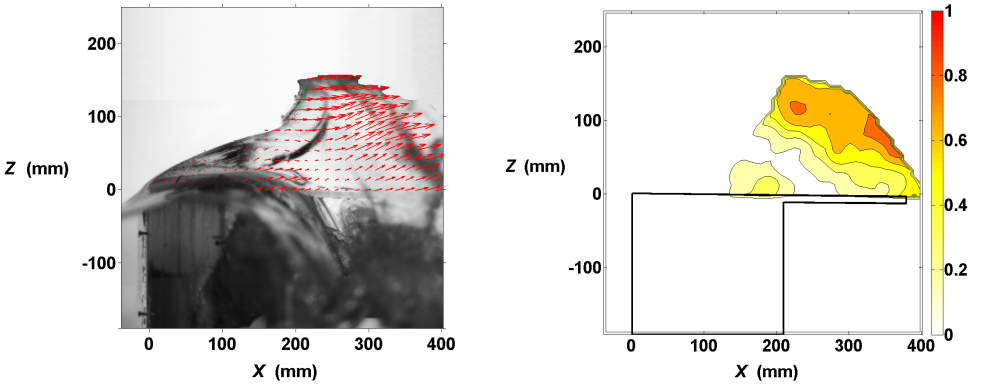

(h)

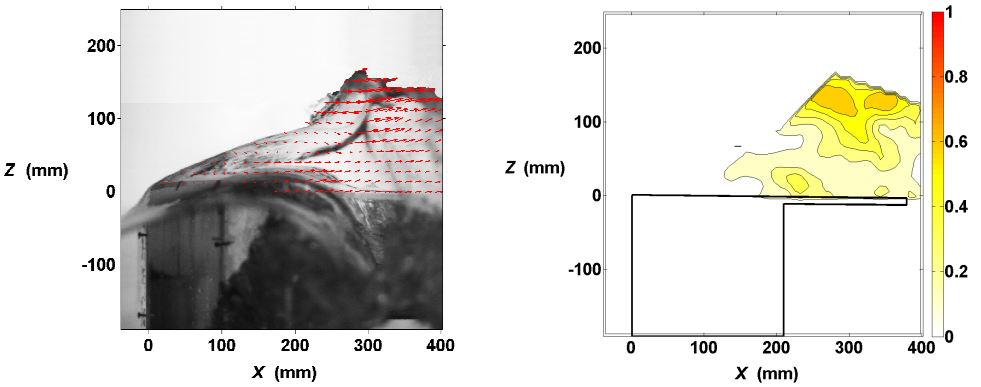

Fig. 3.1 continued.

(i)

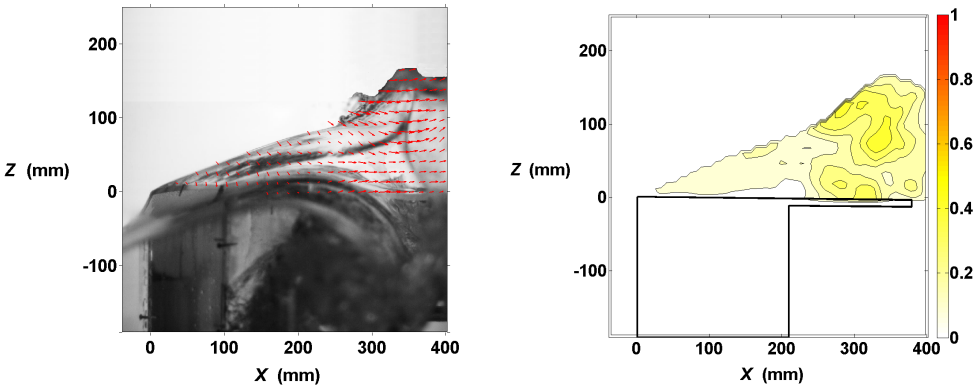

(j)

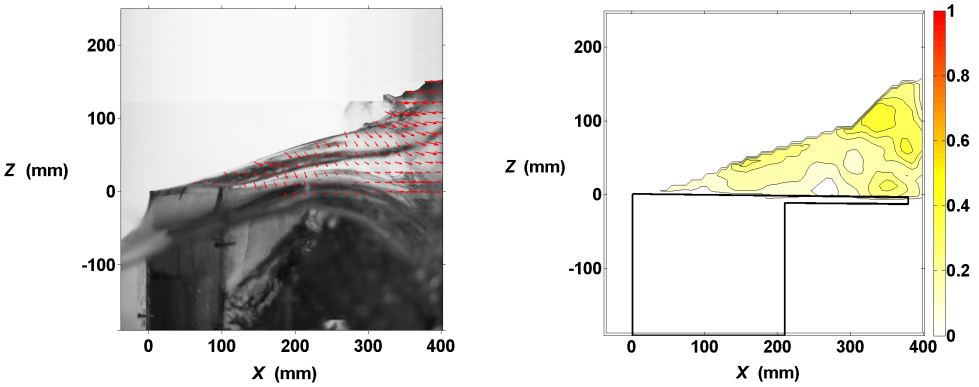

(k)

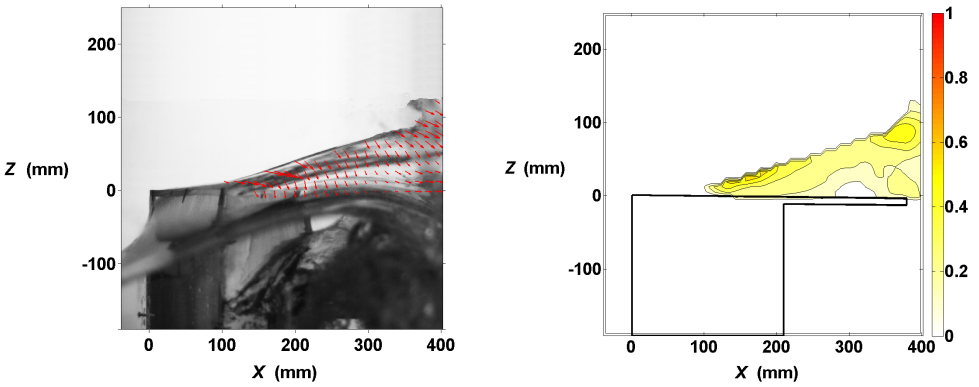

Fig. 3.1 continued.

(l)

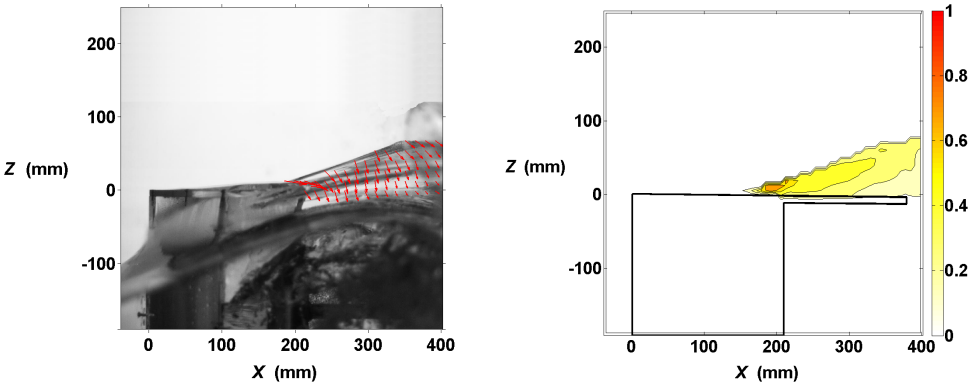

Fig. 3.1 continued.

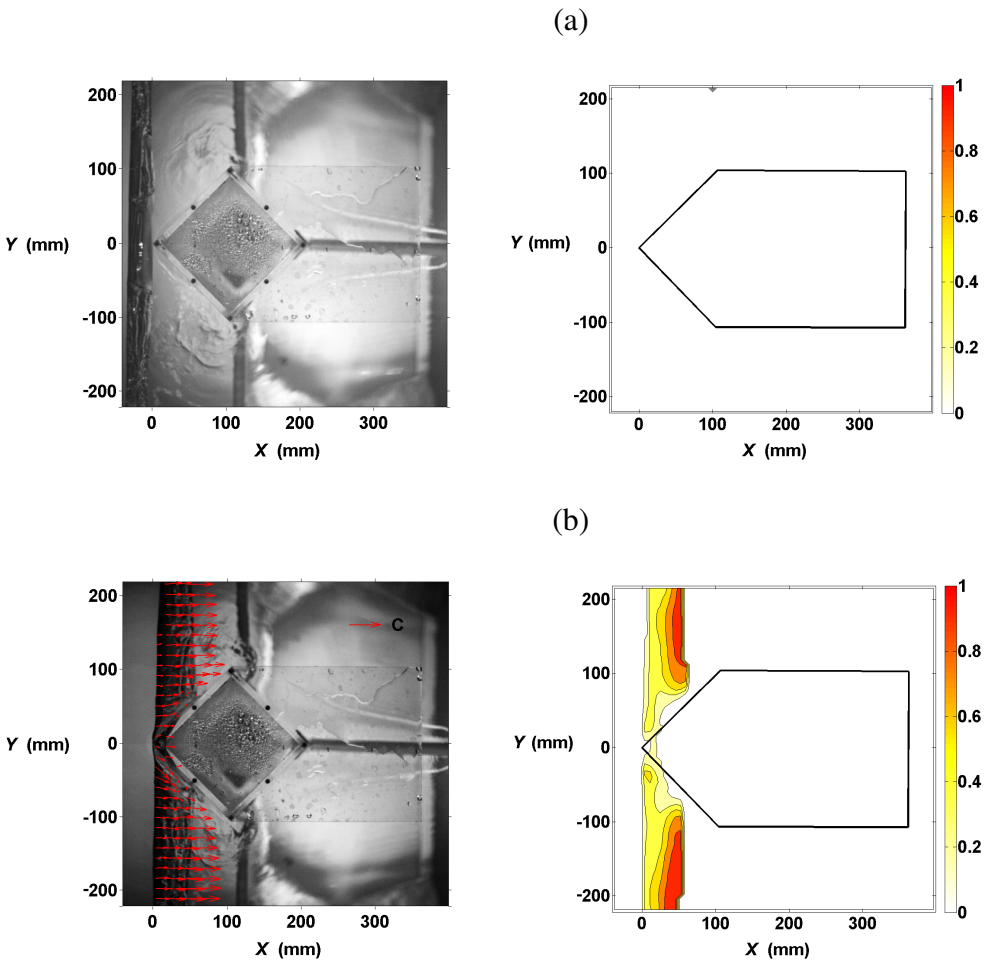

Fig. 3.2. Mean velocity fields on the horizontal plane for the wall impingement case at t = (a) 0.000 s, (b) 0.025 s, (c) 0.050 s, (d) 0.075 s, (e) 0.100 s, (f) 0.125 s, (g) 0.150 s, (h) 0.175 s, (i) 0.200 s, (j) 0.225 s, (k) 0.250 s, (l) 0.275 s. Left column: normalized velocity (normalized using phase velocity, C) vectors; right column: velocity contours. The scale of the contour color bar is C.

(c)

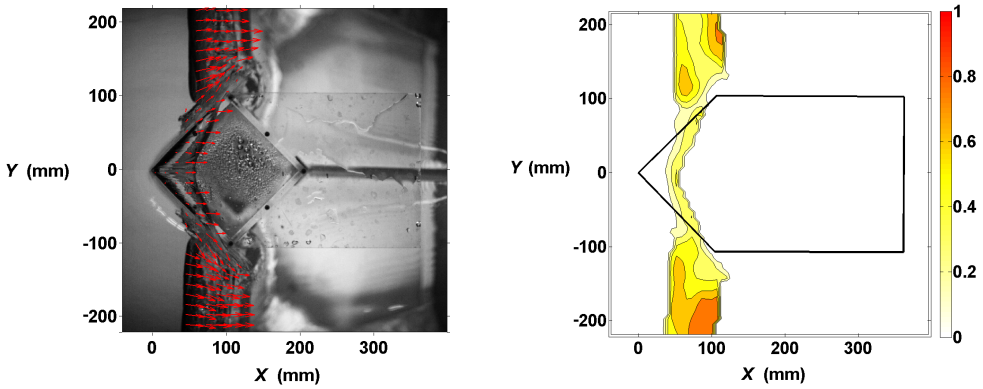

(d)

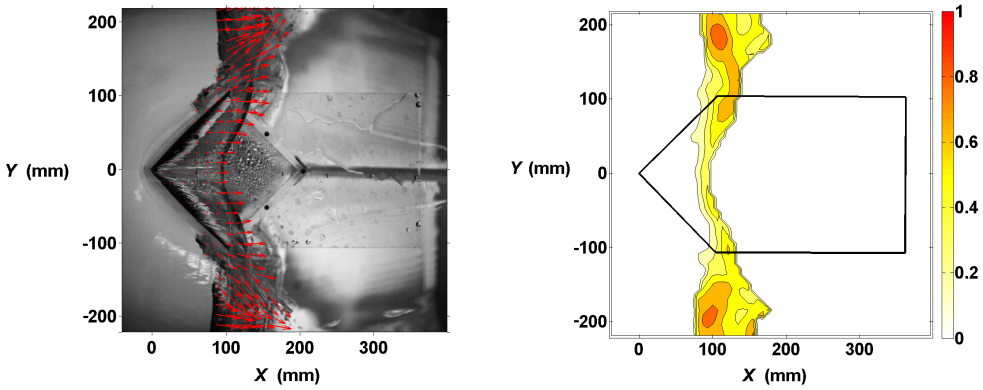

(e)

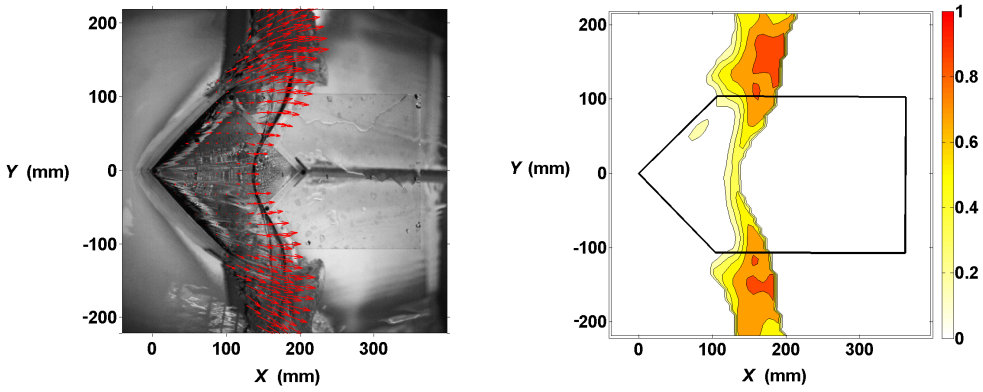

Fig. 3.2 continued.

(f)

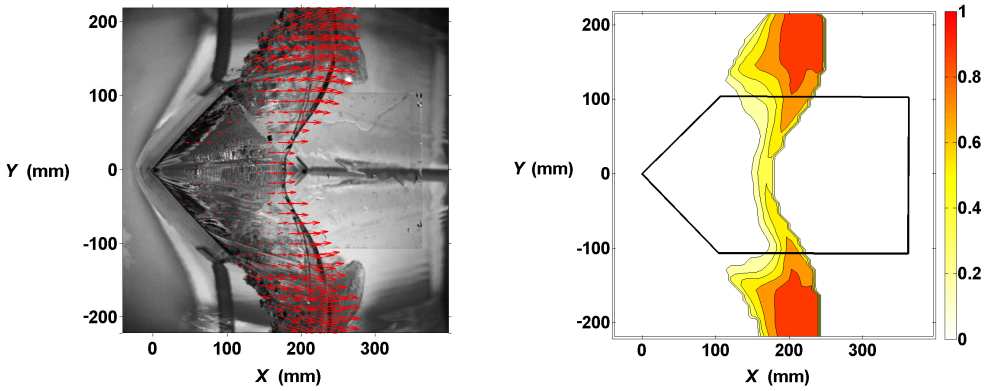

(g)

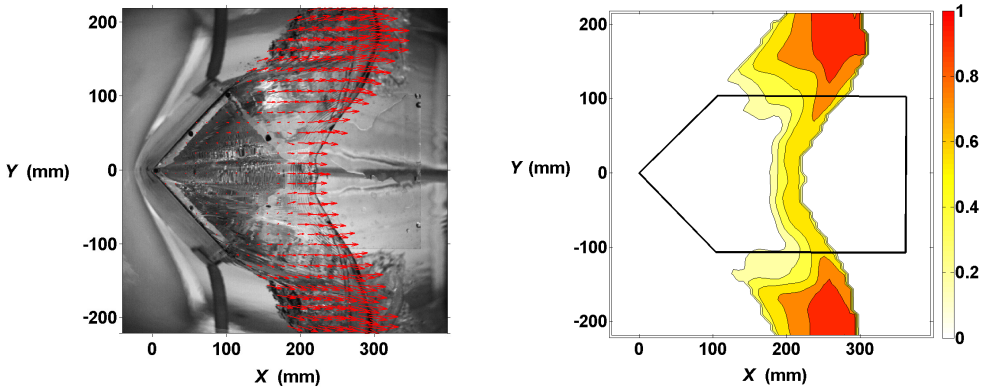

(h)

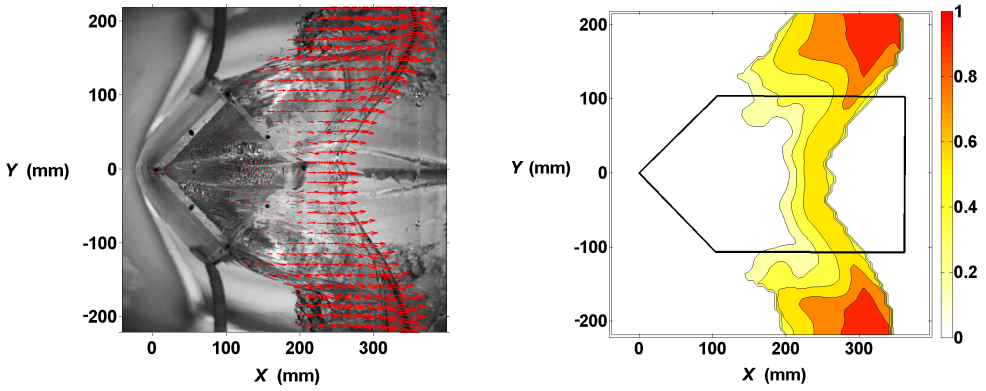

Fig. 3.2 continued.

(i)

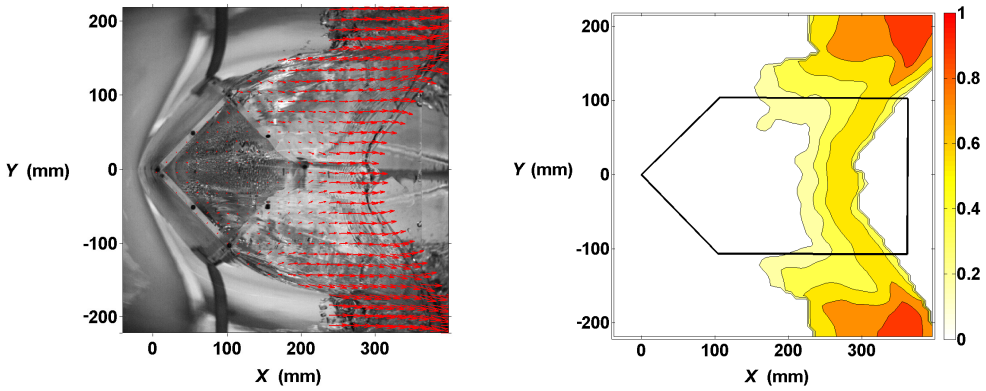

(j)

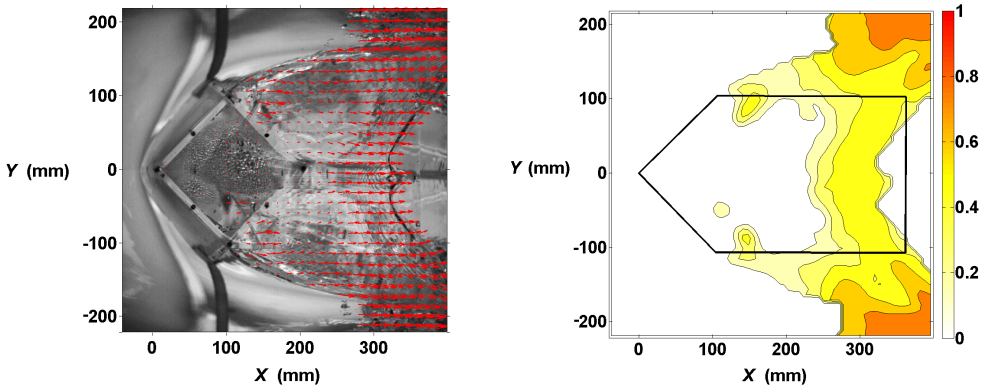

(k)

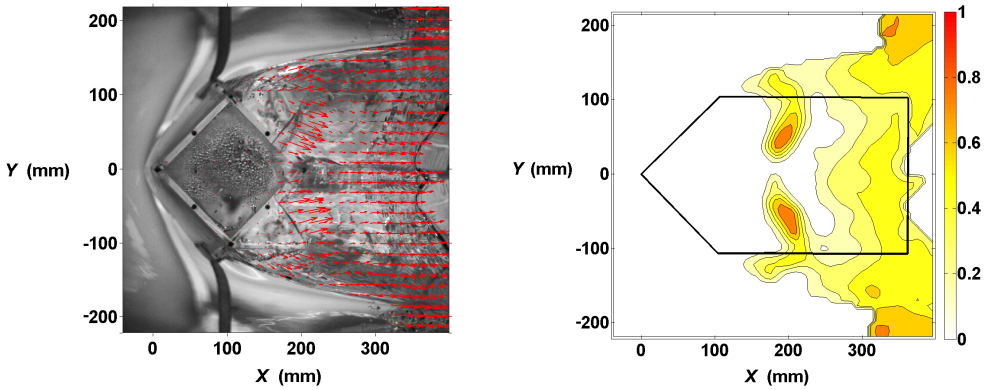

Fig. 3.2 continued.

(l)

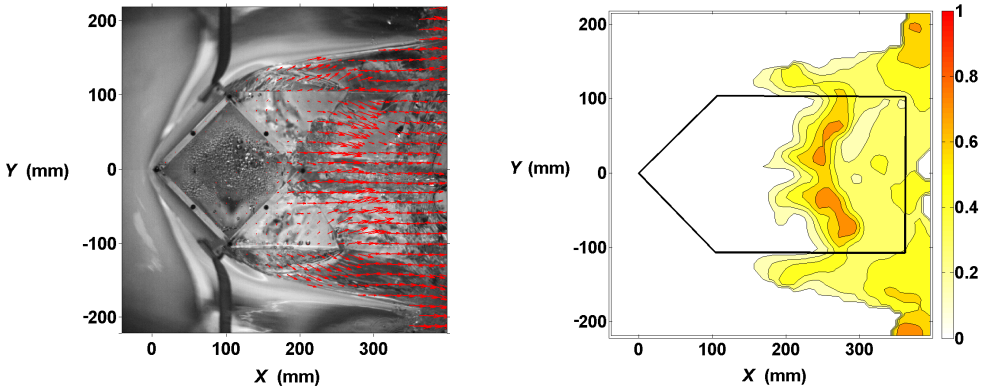

Fig. 3.2 continued.

Figs. 3.1(a) and 3.2(a) show the moment when the breaking wave front touched the structure wall (at the still water level). Immediately after 0.032 s (not shown here), the wave rushed upward with a large vertical velocity component, and reached the horizontal deck surface. The wave front was also deflected around the leading edge of the structure, as shown in Fig. 3.2(b), due to the three-dimensional nature of the structure. The up rushing wave front near the centerline continued to move up and onto the deck with a significant vertical component, as shown in Fig. 3.1(d-e), but the horizontal component near the centerline was much smaller than the ambient velocity near the two side edges of the structure, as shown in Fig. 3.2(d-e). Fig. 3.2(e) also demonstrates that the flow on the deck had a mainly *X*-direction velocity, but outside the deck area the flow had a significant *Y*-direction velocity component due to deflection by the structure. The velocity near the leading edge of the structure, i.e., at (*X*, *Y*) = (0, 0), was indeed relatively small due to the sharp edge that deflected the flow to both sides

and allowed only a small amount of the flow to directly move upward along the centerline. This can be seen from Fig. 3.2(e-g). However, Fig. 3.1(e-g) shows the *X*- and *Z*-direction velocities are quite large, especially near the front. The contradiction is due to the limited DOF used in the vertical plane measurements that captures velocity at a certain distance away from the centerline but within the DOF. Fig. 3.2(i-k) shows that the horizontal profile of the wave front is a bell shape with the flow near the centerline moving slower than that near the side edges. Fig. 3.1(i-k) shows the vertical velocity profile with an unknown uncertainty due to its view at the centerline being blocked by the water near the front tank wall. Even so, Fig. 3.1(e-g) shows the velocity started to lose its vertical momentum and became more horizontally orientated; the velocity might start to move downward as depicted in Fig. 3.1(i-k).

By examining the velocity fields in Figs. 3.1 and 3.2, it can be concluded that the maximum velocity occurred near the front of the flow as it moved onto the deck, regardless of whether the maximum is near the centerline (see Fig. 3.1(c-g)) or away from it (see Fig. 3.2(c-g)). Note that the velocities near (*X*, *Y*) = (150, 200) mm and (150, -200) mm in Fig. 3.2(e) were not at the front; they are associated with flow below the deck surface. This is due to the fact that velocities may still be obtained from out of focus (flatter) images if there are no in focus (sharp) images in the correlation window. The scenario can be identified by checking the raw images. Careful examination of the images confirmed that the front velocities above the deck are indeed the maximum velocities near (*X*, *Y*) = (100, 200) mm and (100, -200) mm.

Based on the vertical plane measurements, the flow accelerated vertically after the breaking jet in Fig. 3.1(a) impinged the vertical wall of the structure at $t = 0$. The jet then took about 0.032 s (at $t = 0.032$ s, not shown here) to move from the impact location at the still water level to the deck level at 0.11 m above. By assuming the front of the jet consists of the same fluid particle, this is equivalent to a vertical velocity of 3.4 m/s (or $1.7C$). Shortly after the wave front moved onto the deck, the front reached the maximum total velocity of 2.5 m/s (or $1.24C$) at $t = 0.086$ s at about $X = 0.17$ m, with a horizontal component of $1.17C$. More details about maximum velocities will be shown in the figures on pages 51 and 53. Fig. 3.2(b) corresponds to the moment immediately after the water appeared on the deck. A close-up of this figure is shown in Fig. 3.3(a). The green water inundated the deck with an angle mainly in the X direction, while the water moved around the structure below the deck. At the edge of water run-up (midway at the 45 degree structure front edges), the entering velocity (onto the deck) is nearly perpendicular to the edges. This transverse component (converging towards the centerline) caused water to gather at the middle of the deck surface during the early run-up process, and subsequently gave rise to the formation of a protruding “tongue” of about 30 mm length at the middle (centerline) of the deck surface, as shown in Fig. 3.3(b), which is a close up of Fig. 3.2(i) at around $X = 300$ mm. This tongue was observed in all 30 repeated tests so it is a repeatable phenomenon. This flow pattern was also observed by Buchner (1995a) and Nielsen and Mayer (2004).

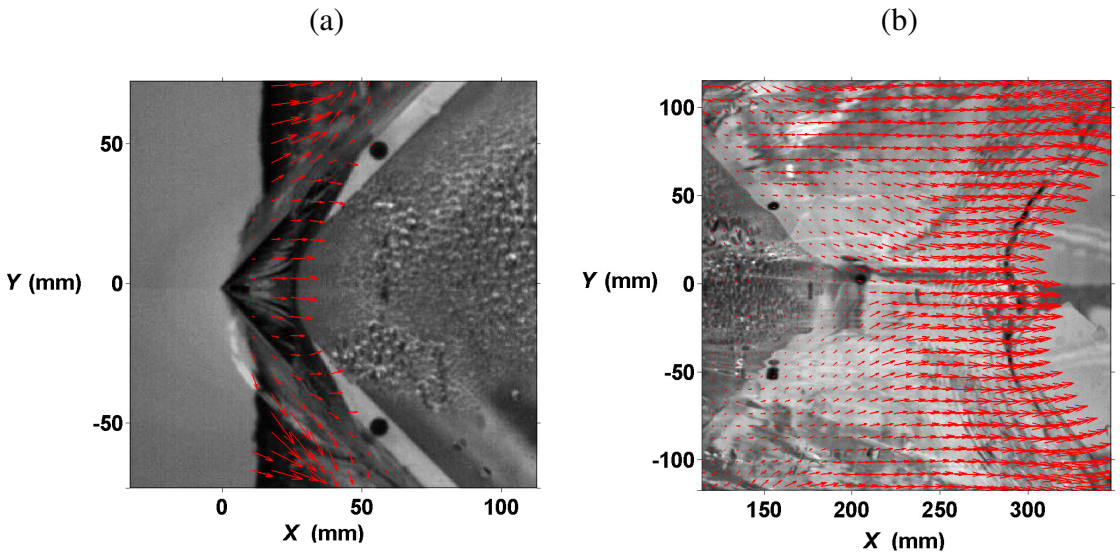

Fig. 3.3. Close up view of green water front corresponding: (a) Figure 3.2(b); (b) Figure 3.2(i).

Based on the horizontal plane measurements, the flow accelerated with time, and attained its maximum horizontal velocity of 1.69 m/s (or 0.84C, about 0.83C in the X component) at t = 0.09 s (close to the moment in Fig. 3.2(e)) and about X = 190 mm. The maximum velocity appeared mostly at the wave front but away from the deck centerline (near the deck side edge).

3.2. Flow kinematics - deck impingement case

The flow fields of the deck impingement case are shown in Figs. 3.4 and 3.5. Similar to that in Figs. 3.1 and 3.2 for the wall impingement case, the velocities are ensemble averaged mean quantities from 30 repeated instantaneous velocity measurements, and the background images are instantaneous and selected from one of the 30 realizations. The time t = 0 was defined as the moment when the wave crossed the leading edge of the deck.

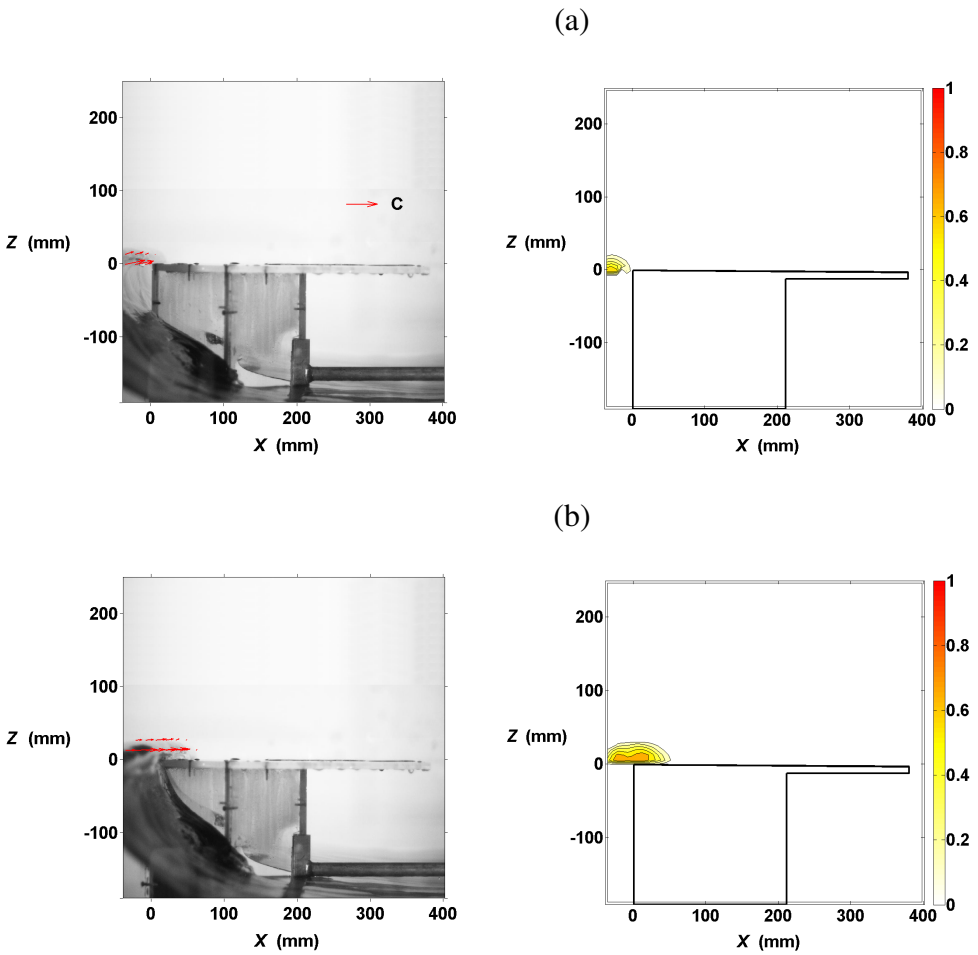

Fig. 3.4. Mean velocity fields on the vertical plane for the deck impingement case at t = (a) 0.000 s, (b) 0.025 s, (c) 0.050 s, (d) 0.075 s, (e) 0.100 s, (f) 0.125 s, (g) 0.150 s, (h) 0.175 s, (i) 0.200 s, (j) 0.225 s. Left column: normalized velocity (normalized using phase velocity, C) vectors; right column: velocity contours. The scale of the contour color bar is C.

(c)

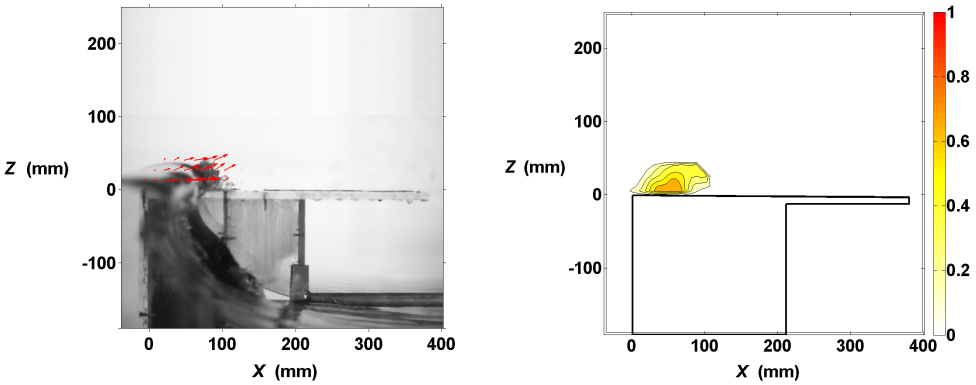

(d)

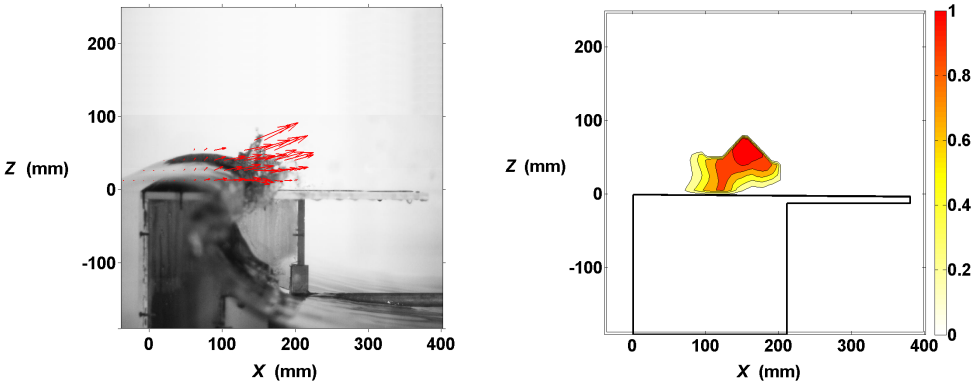

(e)

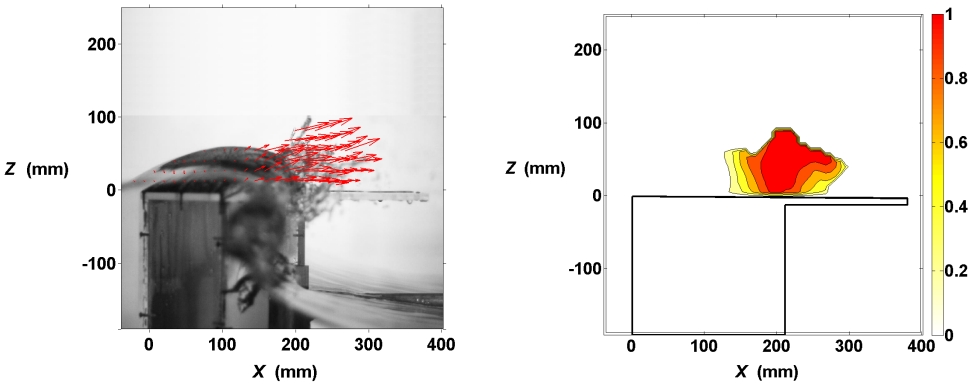

Fig. 3.4 continued.

(f)

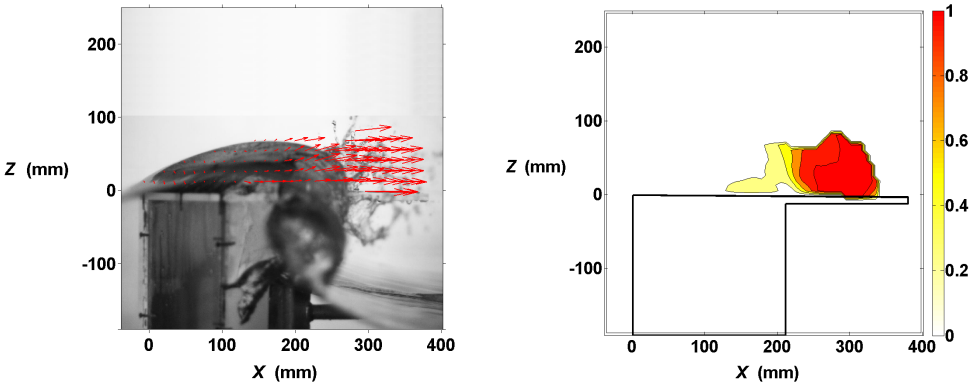

(g)

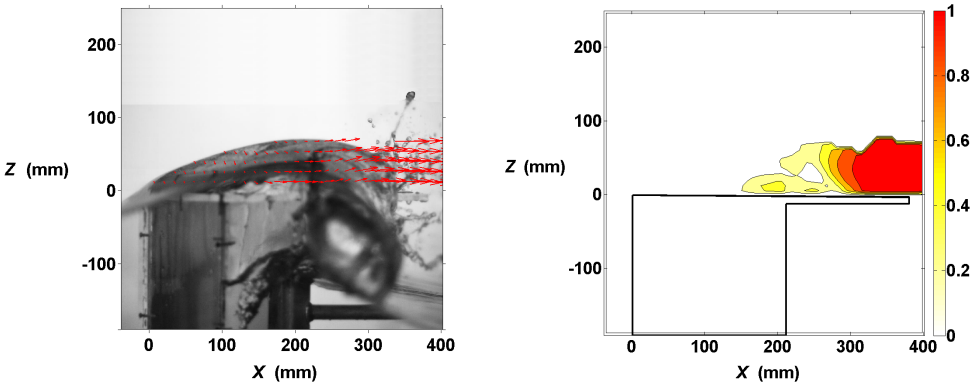

(h)

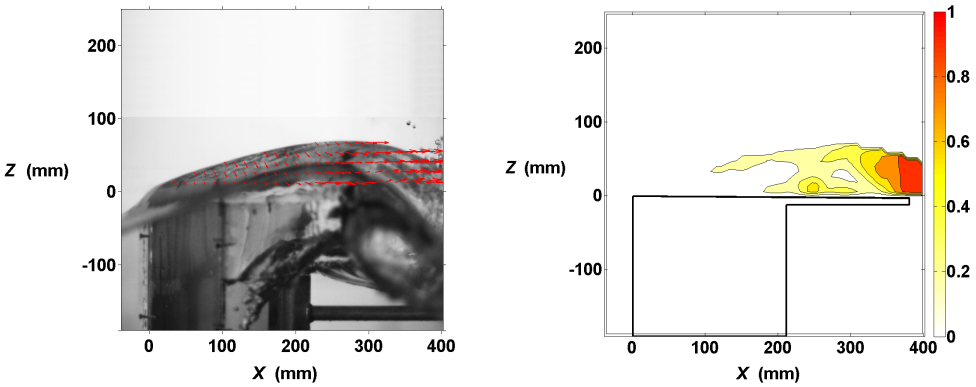

Fig. 3.4 continued.

(i)

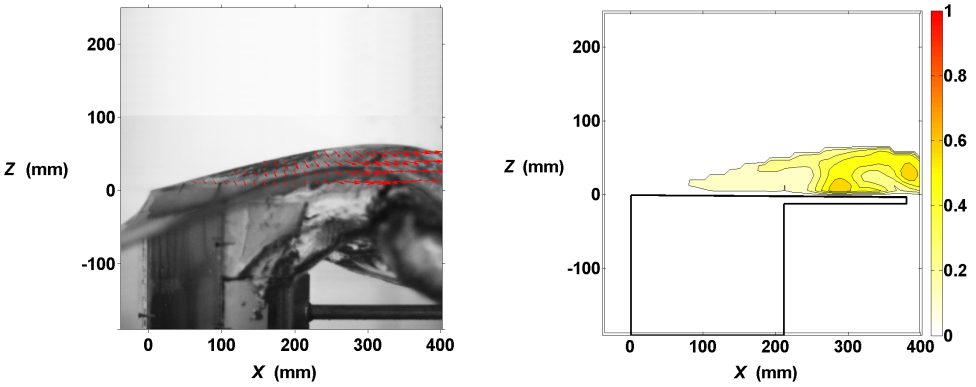

(j)

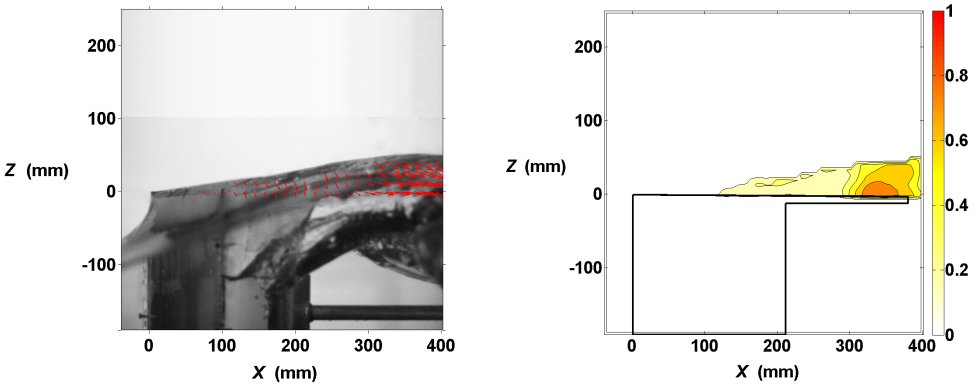

Fig. 3.4 continued.

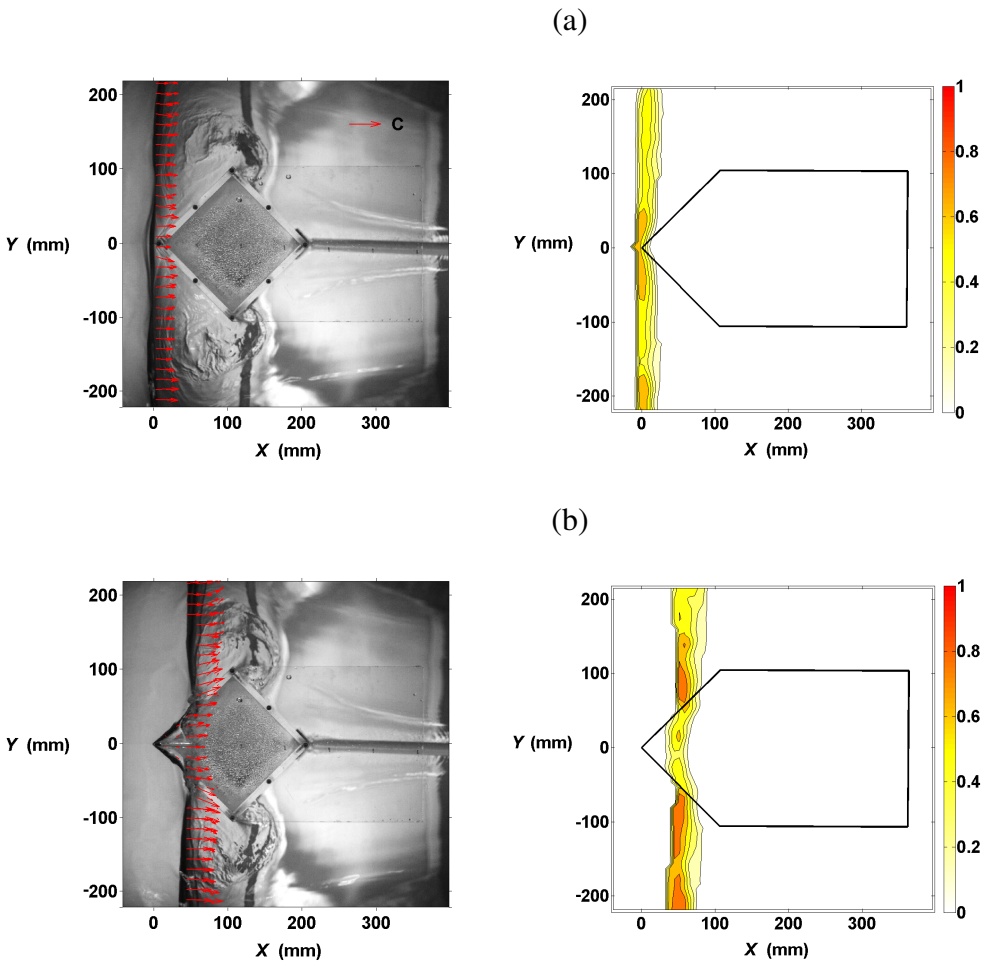

Fig. 3.5. Mean velocity fields on the horizontal plane for the deck impingement case at t = (a) 0.000 s, (b) 0.025 s, (c) 0.050 s, (d) 0.075 s, (e) 0.100 s, (f) 0.125 s, (g) 0.150 s, (h) 0.175 s, (i) 0.200 s, (j) 0.225 s. Left column: normalized velocity (normalized using phase velocity, C) vectors; right column: velocity contours. The scale of the contour color bar is C.

(c)

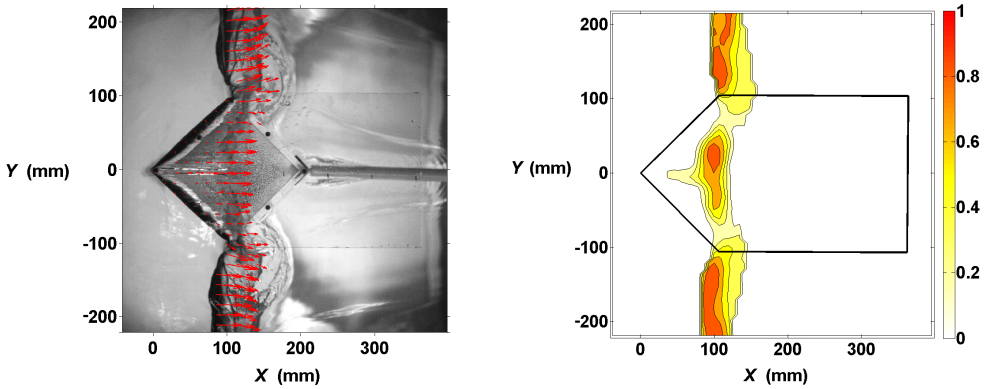

(d)

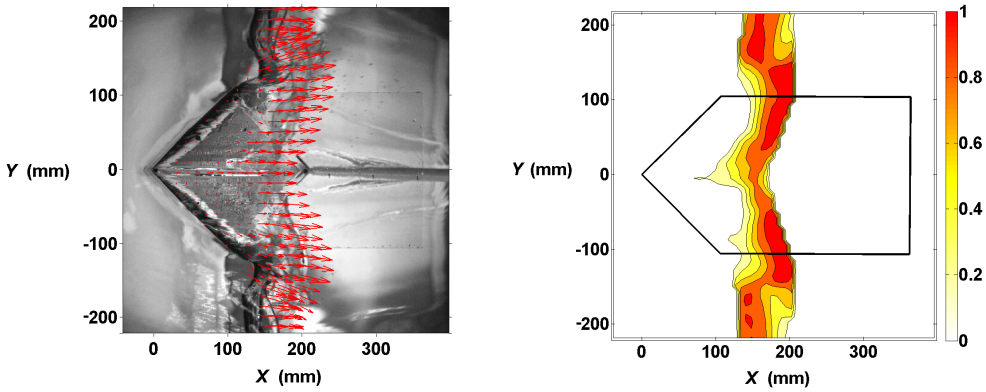

(e)

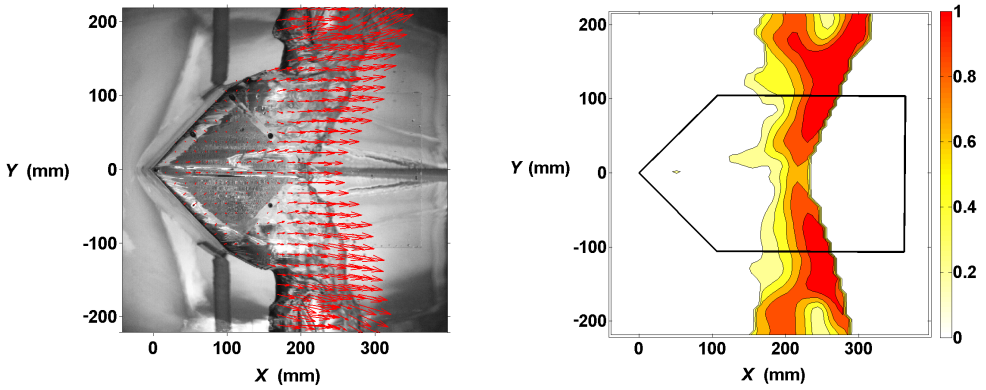

Fig. 3.5 continued.

(f)

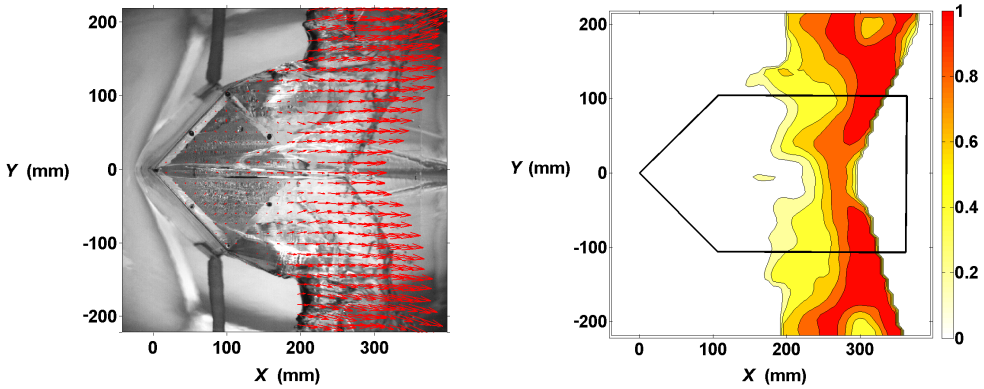

(g)

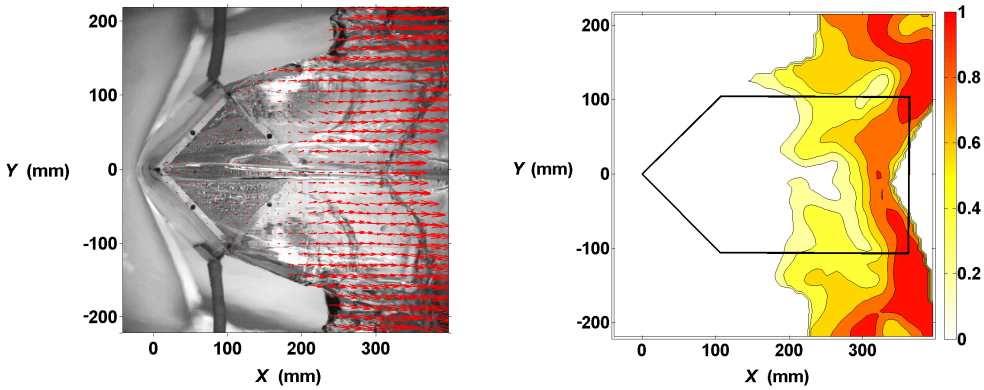

(h)

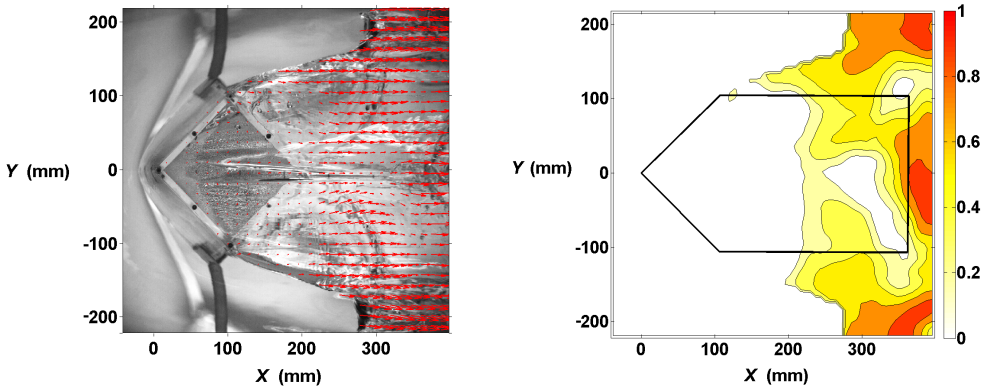

Fig. 3.5 continued.

(i)

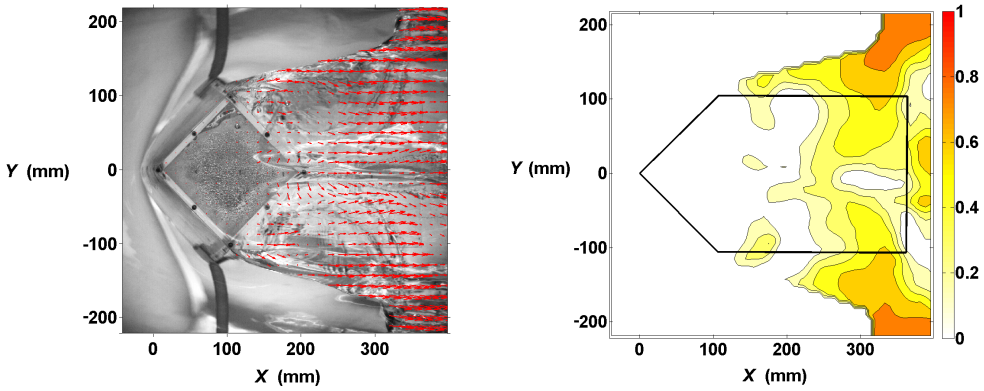

(j)

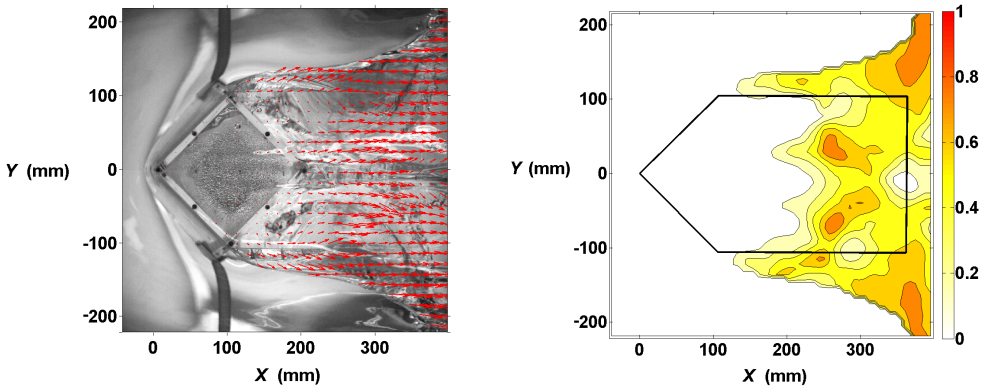

Fig. 3.5 continued.

In Figs. 3.4(a-b) and 3.5(a-b), the overturning jet of the breaking wave is higher than the deck level; the jet impinged the deck surface at about X = 30 mm. The wave front profile above the deck was more or less a straight line in the early process, as shown in Fig. 3.5(a-b). The horizontal velocity profile of the wave front then rapidly changed to a triangular shape, then a bell shape, as shown in Fig. 3.5(e-g). The front profile after this moment seems to become similar to that in the wall impingement case. Similar to the wall impingement case, the maximum velocity appeared at the wave front. However, unlike the wall impingement case, the velocities in the deck impingement case were horizontally dominant on deck without a large Z component, as shown in Fig. 3.4(e-g). In addition, the water in the deck impingement case seems to move as a bulk fluid body above the deck surface, in contrast to the wall impingement case in which the water moves mainly as a water jet above the deck surface. The deck impingement condition hence would produce more adverse effects on objects located on the deck area.

There are several distinct features between the deck impingement case in Fig. 3.4 and the wall impingement case in Fig. 3.1. The wall impingement case features a large vertical velocity component due to the impact of the jet on the vertical front wall of the structure. As expected, the splash reached a much higher elevation above the deck surface, as shown in Fig. 3.1(c-g). The maximum water level above the deck surface reached 0.17 m in the wall impingement case, whereas it reached only 0.08 m (about 50% lower) in the deck impingement case. On the contrary, the horizontal velocity in the deck impingement case is higher, so the green water front required a shorter time to pass the deck surface. In the deck impingement case, the wave front reached a maximum

velocity of 2.94 m/s (or 1.44C) at t = 0.112 s and at about X = 240 mm, close to the moment in Fig. 3.4(e). The maximum velocity was lower at 2.5 m/s (1.24C) in the wall impingement case. Detailed velocity comparisons will be made and discussed in the next section.

Fig. 3.6(a) shows the water front just after impinging on the deck (at a time in between Fig. 3.5(a) and 3.5(b)). Notice that, due to the shape of the model, once the wave impinges on the horizontal deck surface the water at the middle tends to flow straight, while the water near middle tends to flow with a transverse component. The water tongue formed in the wall impingement case as shown in Fig. 3.3(b) was not observed in the deck impingement case here in Fig. 3.6(b). However, Fig. 3.6(c) shows a narrow needle-like water jet protruding out at the center of the wave front. It is indeed the 40 degree jet near the wave front above Z = 50 mm in Fig. 3.4(e-g). This narrow jet was observed in 21 out of the 30 repeated tests.

Note that the BIV technique did not result in velocity measurements in the whole measurement area. For example, the velocity measurements were unsuccessful in the region with no bubbles, and uncertain in the region with flow blocking part of the focal plane in the FOV due to the three-dimensional nature of the problem. Note that if an area in the image is out of focus and blurry without sharp and well focused objects (such as bubbles) inside it, the blurry area may still result in velocities through correlation due to its intensity being the highest. However, the technique captured velocities of the wave front quite well; these velocities are perhaps the most crucial and relevant in the study of green water flow.

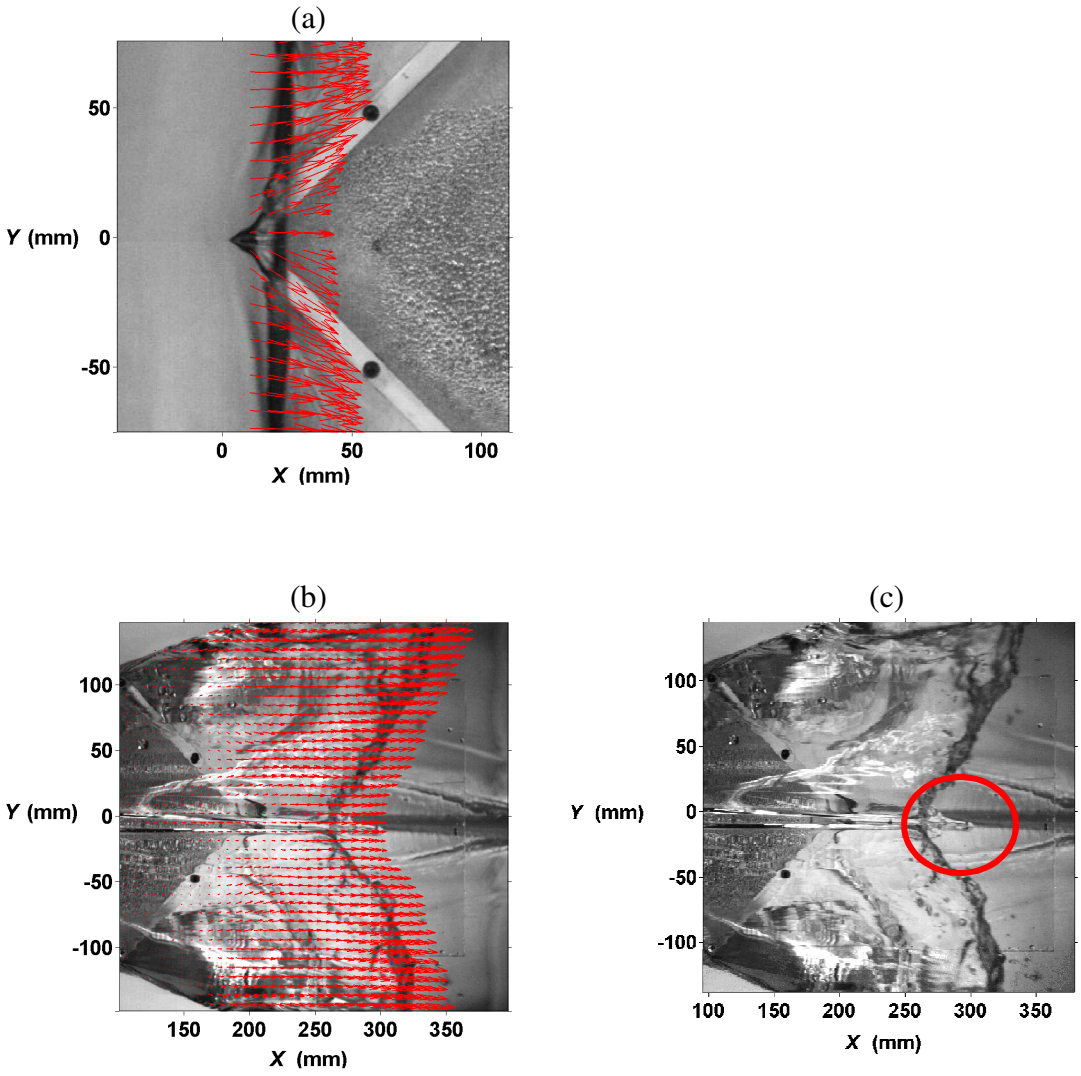

Fig. 3.6. Close up view of green water front for the deck impingement case: (a) just after the impingement; (b), (c) wave front image with the narrow jet in circle.

3.3. Maximum velocities and comparisons

The evolution of the green water flow has been measured. To quantify possible adverse effects to a structure, the maximum velocities, usually at the front of green water, were extracted from the measurements at each time step for both the wall and deck impingement cases. Since the flow is three-dimensional but the measurements are two-dimensional, the velocities measured on the vertical plane and horizontal plane are plotted separately. The plotted velocities are therefore $(UU+WW)^{1/2}_{\max}$ and $(UU+VV)^{1/2}_{\max}$ for the vertical-plane and horizontal-plane measurements, respectively, with (U, V, W) being the mean velocities in the (X, Y, Z) directions. In addition, only velocities vertically above the deck are included in the plots; higher velocities outside the deck area are not included as they have neither impact nor influence on the structure.

Fig. 3.7(a) and 3.7(b) show the maximum velocities for the wall impingement and deck impingement cases, respectively. Velocity components from both the horizontal and vertical plane measurements were plotted, so there are four velocities in each plot with two being the X components. By comparing the X-direction horizontal velocities in Fig. 3.7(a) and 3.7(b), the deck impingement case, as discussed earlier, has a higher maximum U of $1.44C$ (about 16% higher) compared to the maximum U of $1.24C$ in the wall impingement case, whereas the maximum vertical velocity in the deck impingement case is slightly lower (about 8% lower) than that in the wall impingement case. Note that the two X-direction velocities in each case are not identical. The reason is that the two velocities were measured at different locations: one near the centerline of

the structure (the vertical measurement plane) and the other on or near the water surface (the horizontal measurement plane). The maximum velocity on the vertical measurement plane was found to be beneath the water surface, and the maximum velocity on the horizontal measurement plane was found to be away from the centerline and near the outer edges of the structure. As a result, the difference between these two *X*-direction velocities is quite significant, especially in the wall impingement case.

In Fig. 3.7(a-b), the vertical upward velocity (*W*) in the wall impingement case rose to its maximum immediately after the wave impacted the vertical structure wall, whereas in the deck impingement case the wave front traveled a certain distance before it impacted the deck surface and increased its vertical velocity to the maximum. The magnitude of the maximum vertical velocity is 0.81*C* in the wall impingement case, which is higher by 9% than the value of 0.74*C* for the deck impingement case. In addition, the transverse velocities (*V*) are quite small in both cases. The maximum value of *V* is no greater than 23% and 29% of the maximum *U* (based on the values measured from the horizontal plane) in the wall and deck impingement cases, respectively.

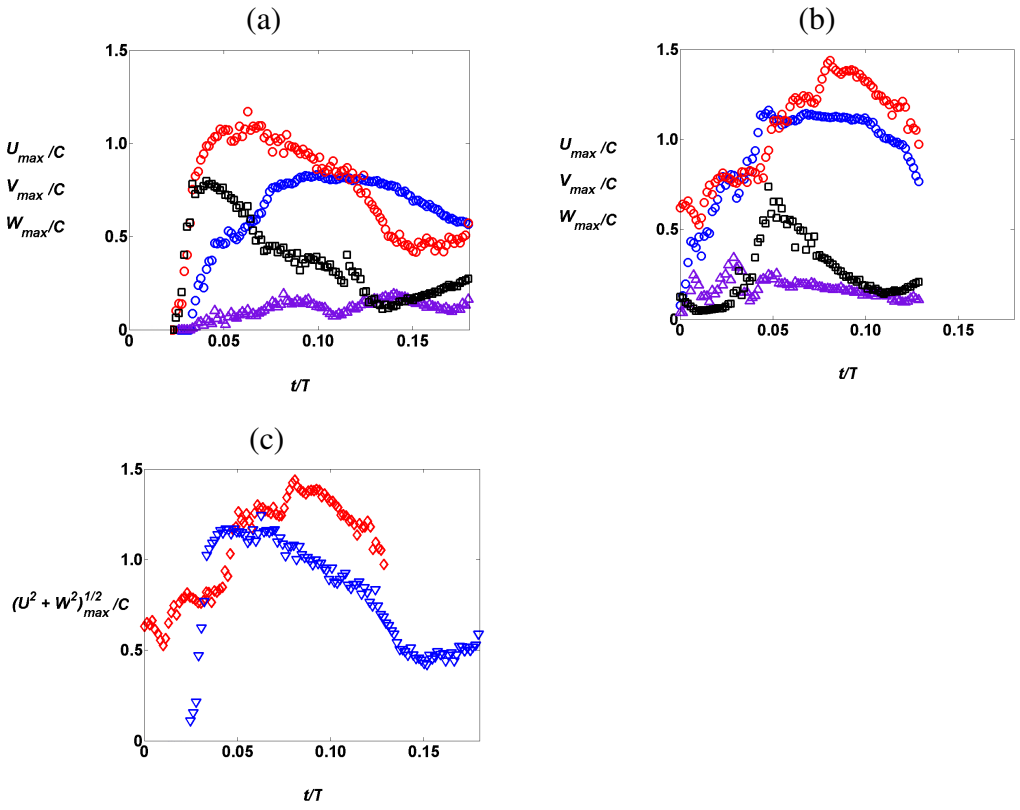

Fig. 3.7. Time history of maximum velocities. (a) Wall impingement case; (b) deck impingement case; (c) comparison of $(UU+WW)^{1/2}_{\max}$. ○, U_{max} from vertical plane; ○, U_{max} from horizontal plane; △, V_{max}; □, W_{max}; ▽, $(UU+WW)^{1/2}_{\max}$ wall impingement; ◇, $(UU+WW)^{1/2}_{\max}$ deck impingement.

Fig. 3.7(c) plots the time history of maximum velocity $(UU+WW)^{1/2}_{\max}$ in the wall and deck impingement cases. Since the dominant velocities are mainly in the *X* direction while the *Y* direction velocity is relatively small, the magnitude of $(UU+WW)^{1/2}_{\max}$ may not be too different from that of $(UU+VV+WW)^{1/2}_{\max}$ (as stated above, $V<0.3U$ so $V^2<0.1U^2$). By comparing the results, the deck impingement case again has a maximum value of $1.44C$, which is 16% higher than the maximum value of $1.24C$ in the wall impingement case. It is thus reasonable to believe that deck impingement is more likely to cause more damage due to the high velocity and therefore momentum and impact loads on objects on the structure deck.

An offshore structure is not fixed in space in ocean, but is allowed to move with six degrees of freedom. This causes the geometry of interaction and, thus the flow to change continuously with waves. The ship wave interaction is important as it may increase the diffraction of the incoming wave and it will affect the flow onto the deck. The relative ship motion is the key parameter in most of the present methods for determining green water loads. However allowing the model to move freely would have considerably increased the complexity of the current study. Therefore the model was kept stationary in the present study.

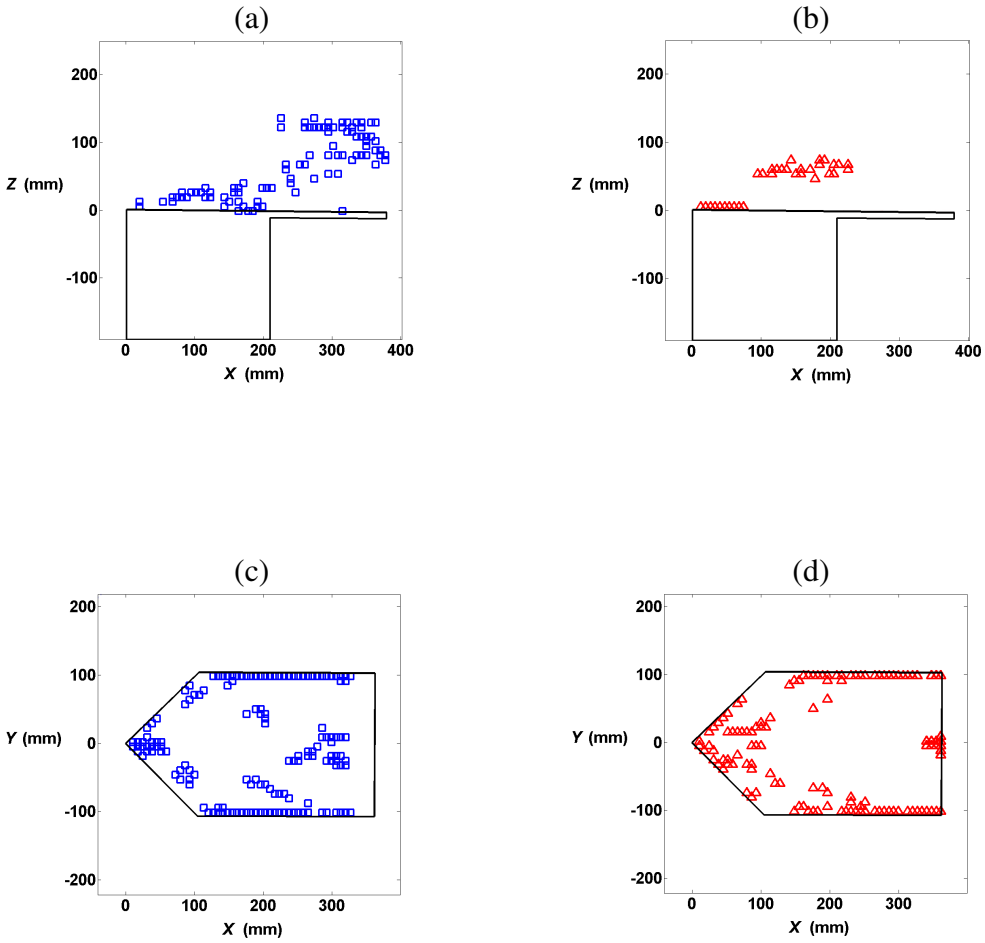

Fig. 3.8. Locations of maximum *X*-direction horizontal velocities. (a) center vertical plane velocities in wall impingement case; (b) center vertical plane velocities in deck impingement case; (c) horizontal plane velocities in wall impingement case; (d) horizontal plane velocities in deck impingement case. □, wall impingement; △, deck impingement.

Fig. 3.8 demonstrates the locations of the maximum *X*-direction horizontal velocities, which can be considered as close to that of the maximum velocity magnitude. Fig. 3.8 (a-b) shows the location of maximum horizontal velocities on the vertical measurement planes for the two cases. For the wall impingement case (Fig. 3.8(a)), it is observed that the highest horizontal velocity near the structure front appears to be above the deck surface. This may be caused by higher vertical momentum as the wave impacts the front wall and rushes upward. On the contrary, Fig. 3.8(b) shows that the location of maximum horizontal velocity near the structure front for the deck impingement case seems to be close to the deck surface before the wave impacts the deck surface. The location then elevates after the impact (the wave reflects upward after impact).

Fig. 3.8(c-d) shows the location of maximum horizontal velocities on the horizontal measurement planes for the two cases. In both cases, the locations are consistently near or at the edges of the structure. This is expected since the horizontal velocity profiles of the wave front are bell shaped or triangular, as shown in Figs. 3.2 and 3.5, implying higher horizontal velocities are away from the centerline and toward the edges.

Similar to the present three-dimensional (3D) experimental study, a two-dimensional (2D) experimental study was conducted by Ryu et al. (2007a) for the wall impingement wave condition. The wave parameters (wave height, wave period, and water depth) are approximately the same for the present study and Ryu et al.'s study. The only difference between these two studies is the shape of the structure, i.e., 3D versus 2D. In Ryu et al. the model structure has a vertical plane-front wall spanning the

width of the tank (i.e., the structure looks like a rectangular box). The experiment is therefore considered as two-dimensional, in contrast to the three-dimensional geometry and flow structure of the present study. The free board (0.11 m) and draft (0.20 m) are also the same for both studies, and so is the location of wave impingement (on the still water level of the structure vertical wall).

The comparison of maximum velocities for the 2D and 3D studies is shown in Fig. 3.9. Interestingly, both the 2D and 3D studies observed a maximum horizontal velocity of 1.2*C* above the deck after the wave rushed onto the deck. However, the maximum vertical velocity, after the wave impinged the vertical front structure wall, reached only 1.7*C* in the 3D study, whereas it reached 2.9*C* in the 2D study. The huge difference is due to the sharp leading edge of the 3D structure that diverges the flow to the sides and significantly reduces the up-rushing component of the flow. If the front edge happens to be a flat edge instead of the sharp leading edge, the vertical run up velocity would be higher than the present observation, since the incoming flow will be more disturbed and the vertical run up component will be larger. The 2D results may be considered as a conservative scenario.

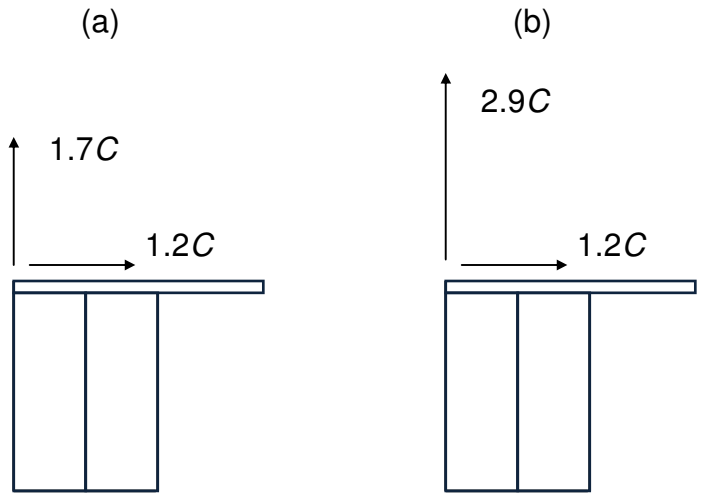

Fig. 3.9. 3D and 2D maximum velocities in the wall impingement case. (a) 3D result in the present study, (b) 2D result in Ryu et al. (2007a).

CHAPTER IV

MODELING GREEN WATER AS A DAM-BREAK FLOW*

4.1. Introduction and literature review

It is known that dam-break flow theory may be used to predict wave overtopping an offshore structure and the associated green water flow. Buchner (1995a) demonstrated the resemblance of a dam-break flow to green water. Due to possible similarity between these two flows, there have been many studies that applied dam-break theory to green water predictions.

Certain design and analysis in estimating the velocity in a green water incident is to use dam-break solutions (Schoenberg and Rainey, 2002). The dam-break flow is a classic problem with many solutions being proposed for various cases of the flow.

---

* Part of the data reported in this chapter is reprinted with permission from "Three-dimensional green water velocity on a model structure" by Chang, Ariyarathne and Mercier (2011). Experiments in Fluids, DOI: 10.1007/s00348-011-1051-0, Copyright [2011] Springer.

Ritter's solution is perhaps the most widely used analytical solution; it is considered as the simplest for a frictionless dry flat bed (Lauber and Hager, 1998).However, Lauber and Hager (1998) found, based on their experimental result, that the front velocity of a dam-break flow is unsteady and decreasing with time, disagreeing with the constant front velocity in Ritter's solution. However, Ritter's solution has been used for green water predictions by industry and in many studies (Buchner, 1995a; Schoenberg and Rainey, 2002). Even so, quantitative validations have not yet been accomplished, mainly due to the difficulty in measuring and modeling green water velocity.

Fekken et al. (1999) and Kleefsman et al. (2005) simulated green water incidents using a Navier-Stokes solver with a volume-of-fluid method for free surface modeling. They modeled a dam-break flow to mimic the water flow on a ship deck. The effects of ship-wave interaction and ship motion were not considered in these studies.

Schonberg and Rainey (2002) developed a numerical model to calculate water velocity on a deck due to green water. The flow was modeled as a shelf submerging into a pool, thus incorporating the fact that the green water inflow on the deck is finite. The numerical model utilizes potential flow theory in desingularized boundary integral equation method combined with an implicit time-stepping algorithm.

Yilmaz et al. (2003) developed a numerical model to simulate green water on a deck. A nonlinear dam-break problem was formulated using equations of motion in the Lagrangian form and solved as an infinite series in time. A semi-analytical solution for pressure was also obtained. Based on calculated pressure, object displacements were computed using equation of motion. The solution was compared with results obtained

based on shallow water assumption. They observed that the shallow water assumption causes some errors in the water elevation profile.

Shigematsu et al. (2004) developed a numerical model to investigate the dam-break waves during the initial stage of green water process. The model is based on Reynolds averaged Navier-Stokes equations with k-ε turbulence closure. The effect of water depth in front of the dam was investigated. They mentioned that the dam-break generated waves during the initial stage cannot be modeled adequately by a long wave model because in the long wave model the vertical velocity and turbulence are ignored. Furthermore, they concluded that, depending on the ratio of water depth in the reservoir and the water depth in front of the dam, the waves can behave like a plunger or spiller.

Pham and Varyani (2005) investigated the use of a dam-break model for estimating green water loading. They used measured wave elevation data to estimate the initial green water velocity. They later used this information as the initial condition in their numerical model for dam-break calculation. They concluded that the dam-break model, with an appropriate initial velocity, predicts the horizontal green water velocity well.

Ryu et al. (2007b) investigated the applicability of dam-break theory based on their measured green water velocities over a two-dimensional model structure. Two approaches were introduced and compared to define the initial water depth behind the dam. They concluded that the dam-break theory predicted velocity agrees surprisingly well with the measured front velocity (which is also the maximum velocity), even though the spatial and temporal distributions of the velocity profile match poorly.

Even though there are many studies that investigated similarities between the dam-break flow and the green water flow, there are some obvious differences between these two flows. For example, green water is three dimensional with water coming from underneath the deck, whereas the dam-break flow is two-dimensional with water coming from above the bed. The amount of water entering the deck is finite, whereas dam-break theory assumes the water input is infinite. In reality the deck moves and the height of free board varies with time, whereas the dam-break flow assumes a stationary, horizontal bed. Furthermore, the green water flow is very complex due to bubbles formation and turbulence, while the dam-break theory neglects these effects. Even though there are some differences between the dam-break flow and the green water flow, application of the dam-break theory to green water velocity prediction may still be viable in practical design. The dam-breaking theory has a simple analytical solution and, according to previous studies, provides a reasonable approximation to the green water flow, at least to the front maximum velocity. It is far workable in comparison to complex and expensive numerical and experimental modeling of the phenomenon.

In the present study, applicability of Ritter's dam-break flow solution for predicting green water velocity over the same three-dimensional structure as in Chapters II and III was investigated. Laboratory measurements on the three-dimensional model structure for both the wall impingement and deck impingement wave conditions were compared with the theory. Both horizontal plane measurements and vertical plane measurements were considered in the study. The theory was compared with the following measurement data: the spatial variations of the maximum horizontal velocity

and averaged horizontal velocity, and measurements from the two-dimensional structure in Ryu et al. (2007b), as stated in Chapter III.

4.2. Results and discussion

Green water has been modeled as a dam-break flow in practice for many years. The dam-break flow has many solutions based on different assumptions. Among the available solutions, Ritter's solution is considered as the simplest.

Applying the conservation of mass equation and the one-dimensional conservation of momentum equation for dam-break flow leads to

$$\frac{\partial h}{\partial t}+\frac{\partial (Uh)}{\partial X}=0$$
$$\frac{1}{g}\frac{\partial U}{\partial t}+\frac{\partial}{\partial X}\left(h+\frac{U^2}{2g}\right)=S_0-S_f \qquad (4.1)$$

where X is the downstream distance from the dam, t is time after the dam breaks, h is the water depth, U is the horizontal velocity, g is gravity, S_0 is the bottom slope, and S_f is the friction slope. Ritter (1892) presented an analytical solution for the dam-break flow by assuming that the flow is one-dimensional, the velocity distribution is uniform over the depth, and pressure is hydrostatic.

According to Ritter's analytical solution, the water depth and velocity can be found as:

$$h = \frac{1}{9g}\left(2\sqrt{gh_0} - \frac{X}{t}\right)^2 \qquad (4.2)$$

$$U = \frac{2}{3}\left(\sqrt{gh_0} + \frac{X}{t}\right) \qquad (4.3)$$

where h_0 is the initial water depth behind the dam. Note that the front of the dam-break flow moves at a constant velocity of

$$U_f = 2\sqrt{gh_0} \qquad (4.4)$$

the above equations thus are valid for $\frac{X}{t} \le 2\sqrt{gh_0}$, and the water depth $h = 0$ for $\frac{X}{t} > 2\sqrt{gh_0}$. See Fig. 4.1 for a sketch of the theoretical dam break flow after time *t*. The constant water depth at the dam at $X = 0$ is thus

$$h_{X=0} = \frac{4}{9}h_0 \qquad (4.5)$$

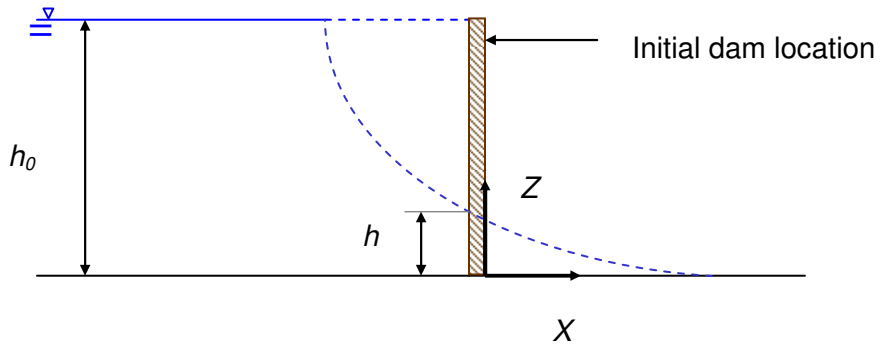

Fig. 4.1. Theoretical dam break flow after time *t*.

Before applying the Ritter's dam-break flow solution, it is required to match the variables between the dam-break flow solution and the present green water measurements. The location of the dam at $X = 0$ is set as the leading edge of the model structure. The initial time of dam breaking at $t = 0$ is set as the moment when the water front is passing the front vertical edge of the model structure.

In the application of dam-break theory to green water prediction, there is no clear definition given in selecting certain required parameters. For example ambiguity exists when choosing the equivalent initial water depth h_0 in the green water flow. Following Ryu et al. (2007b), the initial depth was calculated using two approaches: using the free board exceedance, and matching the green water front velocity.

In the first approach in Ryu et al. (2007b), it was assumed that the wave reflects perfectly. Based on linear wave theory, the amplitude of a perfectly reflected wave equals to the incoming wave height. Thus the initial depth may be calculated based on the difference between the wave height and the free board, i.e.,

$$h_0 = H - z_{deck} \tag{4.6}$$

where z_{deck} is the height of the free board. Ryu et al. (2007b) directly used this difference as the initial depth h_0, treating it as the water level far behind the dam.

On the other hand, Schonberg and Rainey (2002) and Buchner (2002) used the difference of local water level at the dam and the free board height as the constant water level at the dam, and applying Equation (4.5) to obtain

$$h_0 = \frac{9}{4}\left(H - z_{deck}\right) \tag{4.7}$$

In the present study, the primary wave heights are 172.8 mm and 169.0 mm for the wall impingement and deck impingement wave conditions, respectively. The free board was kept at 110 mm for both tested wave conditions. Accordingly, applying Eq. (4.6) we obtained h_0 = 62.8 mm and 59.0 mm for the wall impingement and deck impingement cases, respectively. Alternatively, applying Eq. (4.7) the initial water depths behind the dam were calculated as h_0 = 141.2 mm and 132.7 mm for the wall impingement and deck impingement cases, respectively.

In the second approach in Ryu et al. (2007b), the measured green water front velocity was used to calculate the initial water depth behind the dam. The dam-break theory predicts that the front velocity is constant as shown in Eq. (4.4). This fact was employed by matching the measured green-water front velocity. For both the wall impingement and deck impingement cases, based on the recorded images on the vertical plane the wave front was tracked so its location versus time was obtained. The result of front location verses time is shown in Fig. 4.2. In the figure, the relation between the front location and time is linear, indicating the front velocity is indeed constant. The slopes in the figure are the green water front velocities U_{FG}. They are 2.56 m/s (1.27C) for the wall impingement case and 2.84 m/s (1.39C) for the deck impingement case. It is slightly higher (less than 6%) than the value of 1.2C found by Ryu et al. (2007a) for the wall impingement case on a 2D structure.

Since the green water front velocity is constant and consistent with the dam-break theory calculation, Ryu et al. (2007b) obtained the following equation by replacing the front velocity of the dam-break flow U_f by that of the green water flow U_{FG}.

$$h_0 = \frac{\left(\frac{1}{2}U_{FG}\right)^2}{g} \tag{4.8}$$

Based on matching the front velocities between the dam-break theory and the measurements, the initial water depth behind the dam can be back calculated using Eq. (4.8). Accordingly, we obtained h_0 = 167.0 mm and 205.5 mm for wall impingement and deck impingement cases, respectively. These depths from Eq. (4.8) are somewhat comparable to the initial water depths of h_0 = 141.2 mm and 132.7 mm for the wall impingement and deck impingement cases, calculated based on free board exceedance using Eq. (4.7), although they are 15% and 35% higher. On the other hand, the depths calculated using Eq. (4.8) are 62% and 71% higher than the depth of 62.8 mm and 59.0 mm in the wall impingement and deck impingement cases, respectively, based on Eq. (4.6).

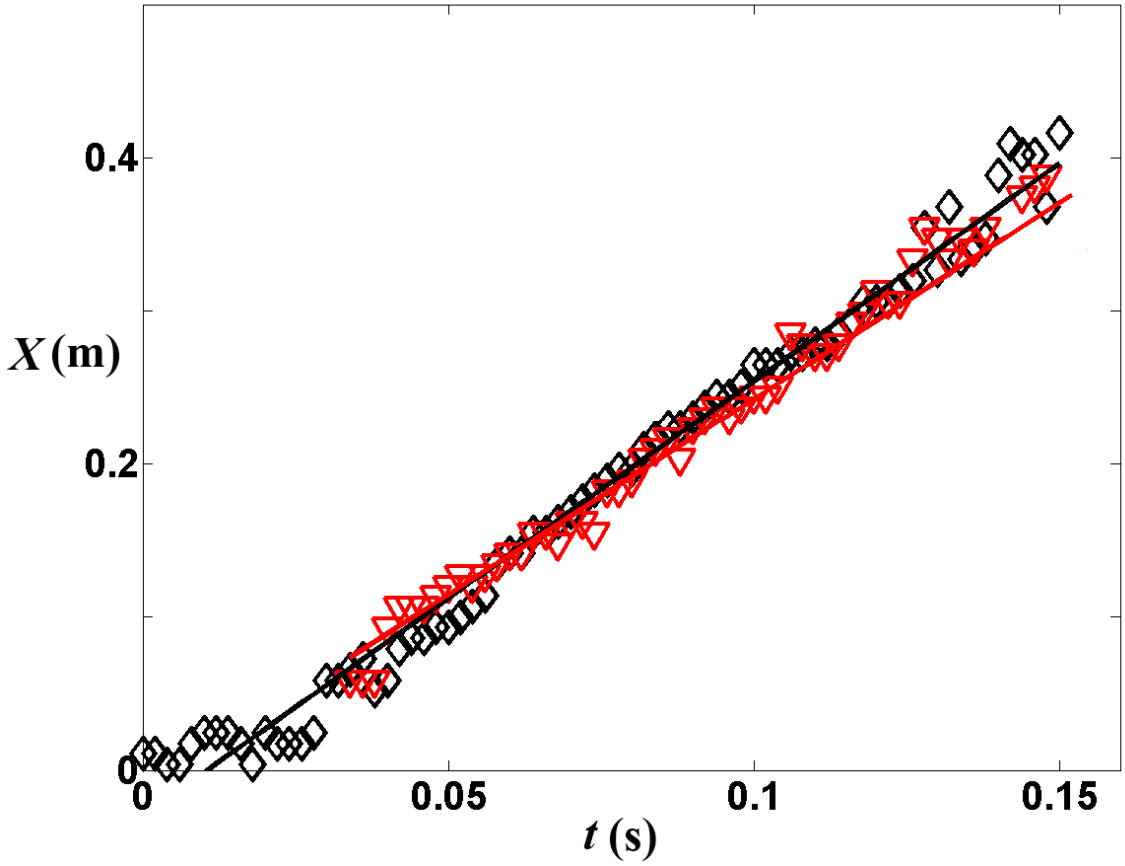

Fig. 4.2. Time history of green water front location based on the vertical-plane images. ◇, deck impingement case; ▽, wall impingement case.

Fig. 4.3 shows the spatial distributions of measured maximum horizontal velocity U_{max} and cross-averaged velocity U_C and their comparison with the dam-break theory based on Eqs. (4.6-4.8) for the wall impingement case. The horizontal plane measured velocity was used for the comparison. The cross-average velocity U_C is defined as,

$$U_C = \frac{1}{y_2 - y_1} \int_{y_1}^{y_2} U dY \tag{4.9}$$

in which y_1 and y_2 are the edges of the horizontal deck surface in the Y direction.

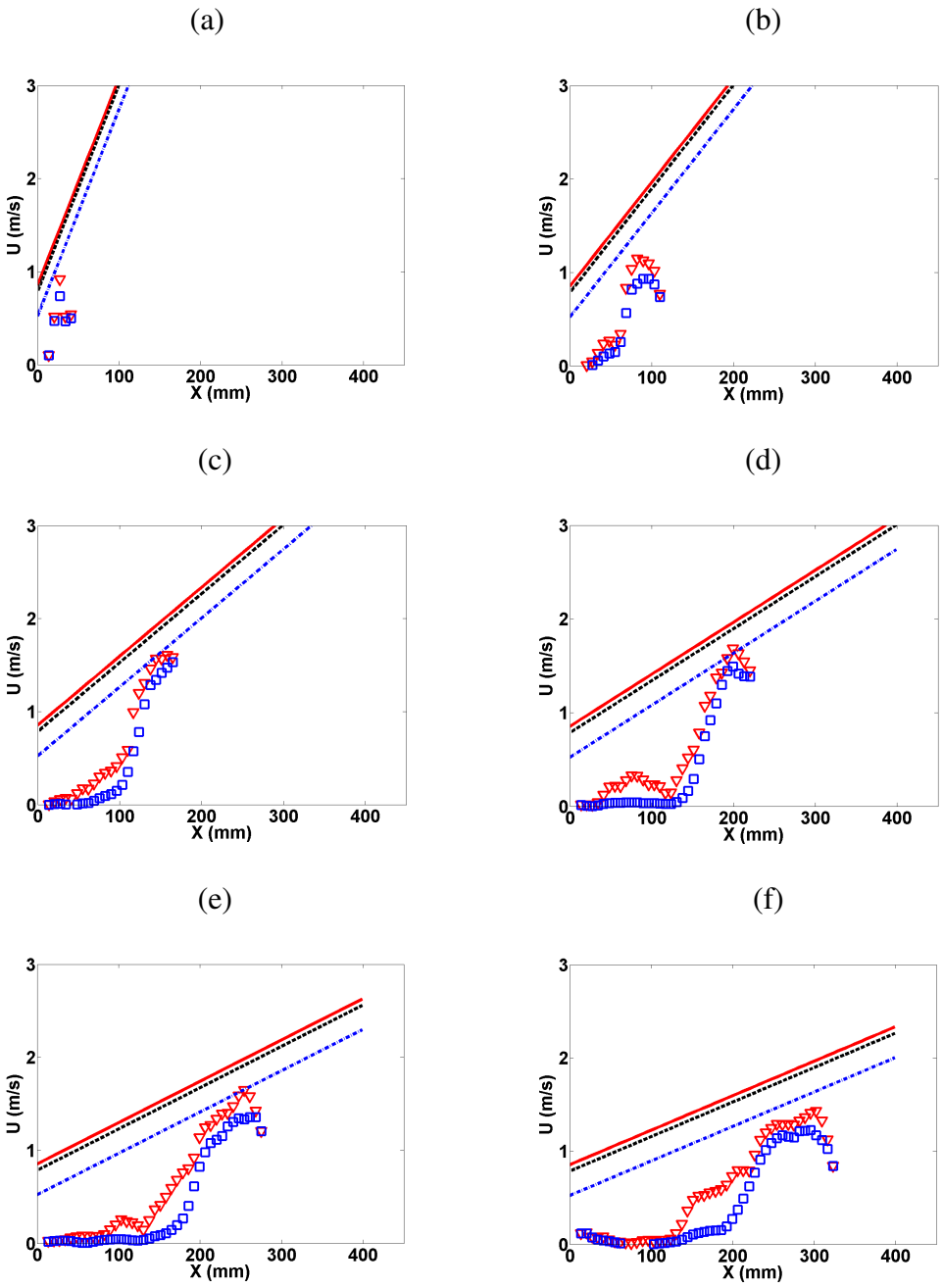

Fig. 4.3. Comparison between the dam-break theory predictions and the horizontal plane velocity measurements for the wall impingement case at t = (a) 0.03 s; (b) 0.06 s; (c) 0.09 s; (d) 0.12 s; (e) 0.15 s; (f) 0.18 s. ▽, U_{max}; □, U_C; ▬ ▮ ▬ ▮ ▬, Ritter's solution based on Eq. (4.6); ▮ ▬ ▬ ▬ ▮, Ritter's solution based on Eq. (4.7); ▬, Ritter's solution based on Eq. (4.8).

As Fig. 4.3 shows the profiles from the dam-break theory predictions are linear, whereas the measured velocity profiles are not. It is clear that the theory predictions are higher compared to measured values except for the lowest velocity prediction using Eq. (4.6). The dam-break predictions are thus conservative and may be safe for design purpose. The measured maximum green water velocity agrees with Eq. (4.6) the best, whereas Eqs. (4.7-4.8) over predict.

One may wonder why the comparison by matching the velocities between the dam-break flow and the green water flow does not work too well. The problem is cause by the variation of green water front velocity due to the 3D geometry of the structure. The front velocity of U_{FG} = 2.56 m/s (1.27C) based on images on the vertical plane in Fig. 4.2 and used in Eq. (4.8) is different from that based on images on the horizontal plane. Fig. 4.4 shows the time history of green water front locations for the wall impingement case based on horizontal plane images. In the figure, lines (1a) and (2a) show consistent slopes (i.e., velocities) between the front most (on or outside the deck surface) velocity and edge velocity at the front most (angled section) of the structure. These two velocities of about 2.3 m/s (1.14C) measured on the horizontal plane is close to (or 10% lower than) the velocity U_{FG} = 2.56 m/s (1.27C) measured on the vertical plane. However, beyond a short distance, the slopes or front velocities reduce to 1.70 m/s (0.84C) and 1.66 m/s (0.82C) at the edge and center of the structure, respectively, after water reaching the constant-width section of the deck and moving out of the deck from the side edges. In Fig. 4.3, results from the horizontal plane images were used in the comparison so the measured front velocities appear to be lower when compared with

the dam-break velocity calculated based on Eq. (4.8). Note that slope 2(c) (the front velocity at the center of the deck) and slope 2(b) (the front velocity at the edge of the deck) in the wall impingement case are quite close to each other with a difference only about 2%.

Fig. 4.5 shows the spatial distributions of U_{max} and U_C and their comparison with the dam-break theory based on Eqs. (4.6-4.8) for the deck impingement case. Since the differences among the three dam-breaking predictions are relative small, they all predict the maximum velocity well, although Eq. (4.8) agrees the best. Similar agreement was also found in measurements on a 2D structure by Ryu et al. (2007b).

Unlike the wall impingement case, the deck impingement case does not have the problem of lower measured front velocity on the deck as seen in Fig. 4.4. This is the fundamental difference between the wall impingement and deck impingement cases. Green water was deflected by the vertical and angled front wall in the wall impingement case before it rushes onto the deck. Once water is on the deck, the deflection effect causes water to move side way and out of the deck surface within a short distance. On the other hand, green water rushes directly onto the deck in the deck impingement case without a significant deflection effect caused by water hitting the structure vertical wall. The front velocity on the deck remains consistent. The flow patterns can be seen in Figs. 3.2 and 3.5.

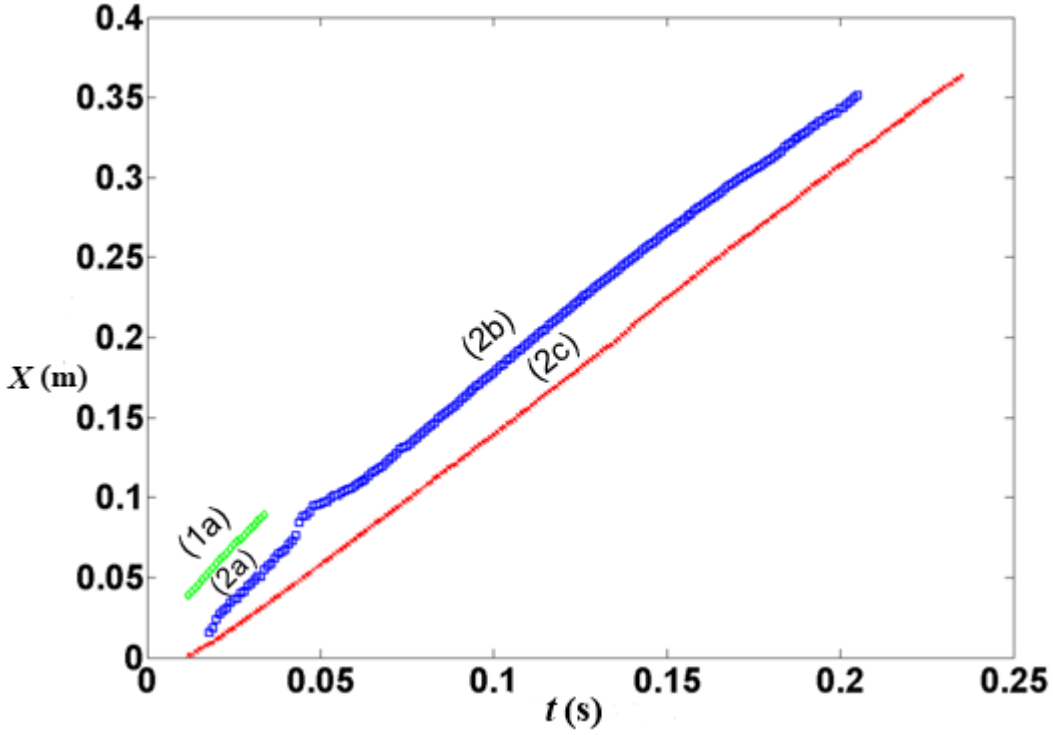

Fig. 4.4. Front locations of green water on the horizontal plane in the wall impingement case. Line (1a): at the front most (on or outside the deck surface area) with a slope 2.30 m/s; lines (2a-b), at the edge of the deck with slopes 2.27 m/s at the front most (angled section) and 1.70 m/s beyond that (constant width section); line (2c), at the centerline with a slope of 1.66 m/s.

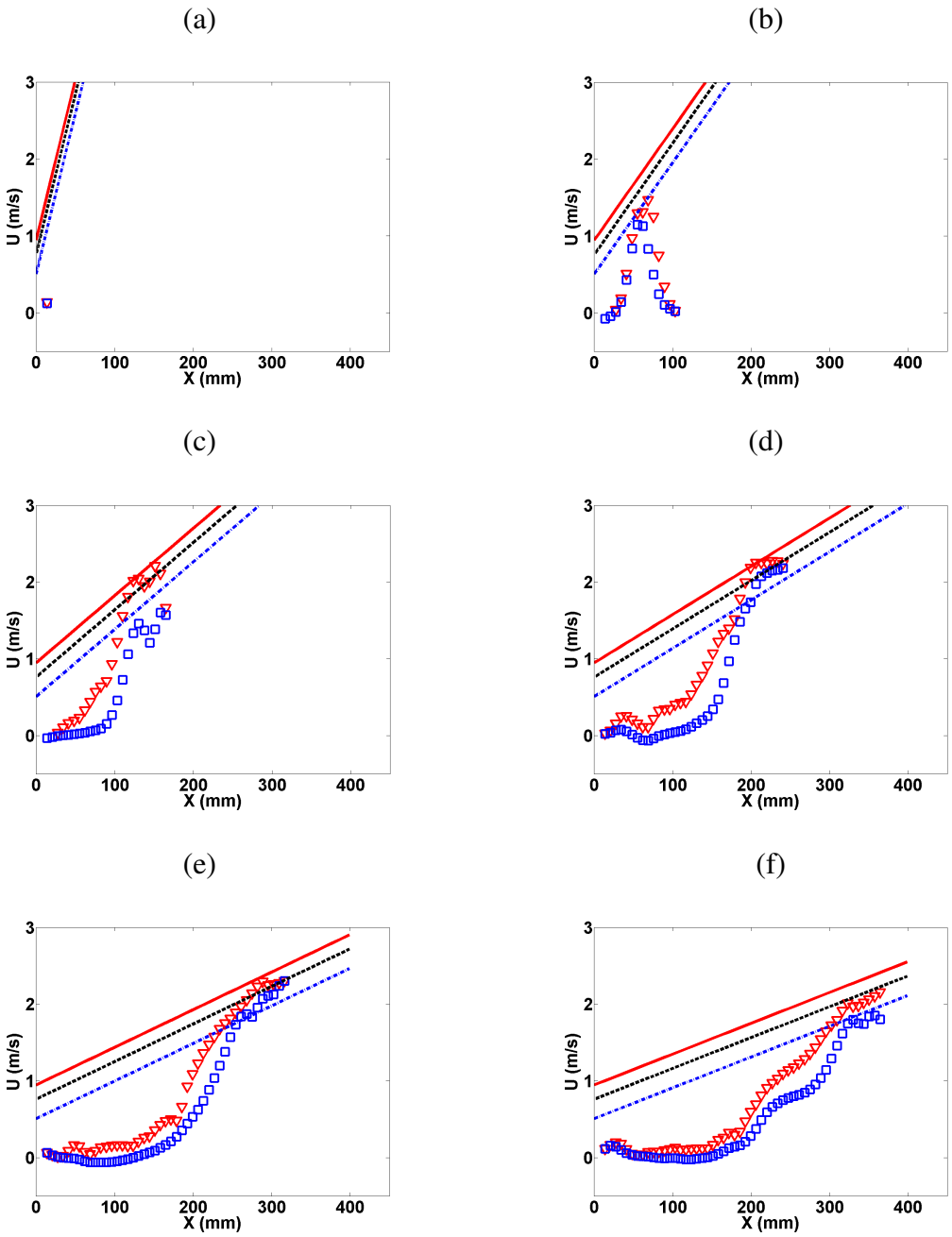

Fig. 4.5. Comparison between the dam-break theory predictions and the horizontal plane velocity measurements for the deck impingement case at t = (a) 0.03 s; (b) 0.06 s; (c) 0.09 s; (d) 0.12 s; (e) 0.15 s; (f) 0.18 s. ▽, U_{max}; □, U_C; ▬ ▪ ▬ ▪, Ritter's solution based on Eq. (4.6); ▪ ▪ ▪ ▪, Ritter's solution based on Eq. (4.7); ▬, Ritter's solution based on Eq. (4.8).

Fig. 4.6 shows that the green water front velocity based on vertical plane images is 2.84 m/s (1.39C) and the front velocity based on horizontal plane images is 2.60 m/s (1.27C) which is about 9% lower than that from the vertical plane measurements. The velocity measurements are thus consistent between these two planes. This can also be considered as a validation of the BIV measurement technique. A slightly lower velocity from the horizontal plane measurements is expected since the maximum velocity is not on the water surface but below the surface, as shown in the vertical plane measurements in Figs. 3.1 and 3.4.

Ryu et al. (2007b) examined the applicability of dam-break theory on a 2D structure using the same wave parameters as the present study. The present measurements on the 3D structure were compared with Ryu et al.'s measurements. Since Ryu et al. only measured velocity on a vertical plane for the wall impingement case, the vertical plane measurements in the wall impingement case in the present study were used in the comparison for consistency.

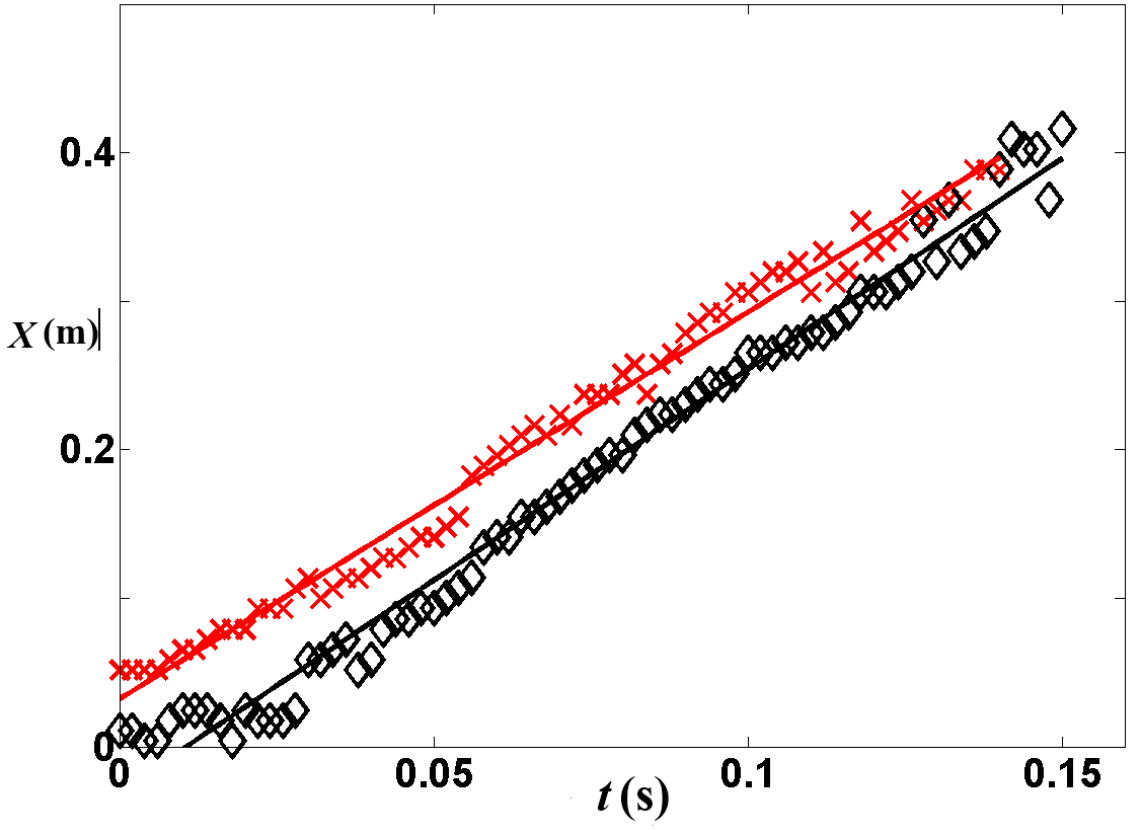

Fig. 4.6. Front locations of green water in the deck impingement case. ◇, vertical plane measurements; ×, horizontal plane measurements.

Both the maximum horizontal velocity U_{max} and the depth-averaged velocity U_D were compared. The depth-averaged velocity is defined as

$$U_D = \frac{1}{z_2 - z_1} \int_{z_1}^{z_2} U dZ \tag{4.10}$$

where z_1 and z_2 are the lower and upper surface of green water in the Z direction on the horizontal deck surface. Note that on the 2D structure in Ryu et al. (2007b), $X = 0$ was defined as the front leading edge of the model structure, and $t = 0$ was defined as the instant when the water front crosses the leading edge of the model structure, similar to the definitions in the present study.

The measured U_{max} and U_D profiles for the 2D and 3D cases are shown in Fig. 4.7. In the figure, both U_{max} and U_D in the 2D case are higher than that in the 3D case. However, the difference is not too significant, especially at the beginning of the green water process. In general Eq. (4.8) seems to provide an overall best prediction, consistent with what Ryu et al. (2007b) found in their study using the 2D structure.

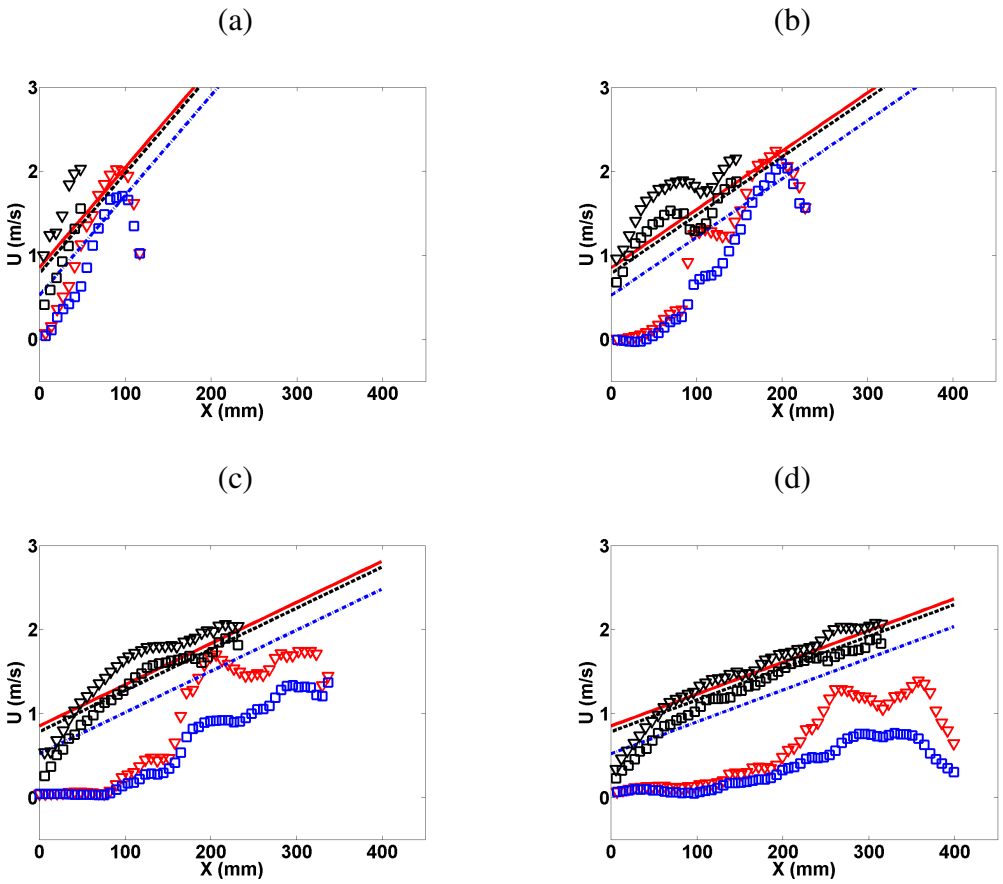

Fig. 4.7. Comparison of dam-break theory with the vertical plane velocity measurements for the wall impingement condition for the 2D and 3D cases at t = (a) 0.02 s; (b) 0.06 s; (c) 0.10 s; (d) 0.14 s. ▽, 3D U_{max}; □, 3D U_D; ▽, 2D U_{max}; □, 2D U_D; Ritter's solution based on Eq. (4.6); Ritter's solution based on Eq. (4.7); Ritter's solution based on Eq. (4.8).

CHAPTER V

GREEN WATER IMPACT PRESSURE*

5.1. Introduction and literature review

Wave impact pressure information is important in the design and safety of an offshore structure. This is especially important when the structure is under green water loading. Both numerical and experimental studies have been conducted to reveal the fundamental reasons for the huge impact pressure exerted on offshore structures by green water. Although impact pressure caused by non-breaking waves has been studied with good understanding, impact pressure caused by breaking waves is less understood and somewhat inconclusive among many studies.

Bagnold (1939) conducted a detailed laboratory experimental study to investigate the nature of the shock pressure exerted on a vertical wall. He identified three types of impact pressure due to breaking waves. Firstly, if the location of wave breaking occurs early compared to the wall location, the wave front jet collapses before reaching the wall. Secondly, if the breaking occurs a little later, the jet may strike the wall before it falls. In doing so, it encloses a large cushion of air between the wall and wave front.

---

* Part of the data reported in this chapter is reprinted with permission from "Three-dimensional green water velocity on a model structure" by Chang, Ariyarathne and Mercier (2011). Experiments in Fluids, DOI: 10.1007/s00348-011-1051-0, Copyright [2011] Springer.

In this case, when the concave front advances, the air is compressed, the water finally bursts upward with forming spray. Finally, if the breaking occurs beyond the above cases, which is the case where he observed highest impact pressure, the air cushion gets much thinner. A very flat vertical wave front hits the wall, and high impact pressure exists for a very short period of time. He observed a great variation in the pressure maxima from impact to impact, for the same incoming wave condition. With analytical approach, he proposed an equation to calculate the maximum impact pressure. He further mentioned that the impact pressure measured in the lab is higher than that observed in the field for the same wave condition due to different physical properties between sea water and fresh water.

Blackmore and Hewson (1984) measured impact pressure on seawalls in the field, and compared them to predictions using existing semi-empirical equations. They showed that values calculated using these equations are not accurate. They later derived an expression for estimating impact pressure based on the local wave parameters and a void ratio coefficient. Ochi and Tsai (1984) conducted laboratory experiments to investigate impact pressure produced by deep water waves breaking on a circular cylinder, which represents a column of an offshore structure. Two different breaking conditions were considered: one is impact associated with waves breaking in close proximity to the structure, and the other is impact caused by waves approaching the structure after they have broken. For both breaking conditions, they presented that impact pressure is proportional to the square of impact velocity. A method to statistically predict the magnitude of the impact pressure is also given.

Chan and Melville (1988) obtained simultaneous measurements of kinematics and dynamics of impact pressures on a vertical wall resulting from a plunging breaking wave in deep water. They concluded that the characteristics and distributions of impact pressure depend on the wall location relative to the wave breaking location. Further they mentioned that for each location, identical incident wave conditions could give significantly different impact pressure due to randomness of trapped air dynamics during the wave breaking process. They observed that the impact occurs through focusing of incident wave front towards a localized zone on the wall. Within the localized zone, wave impact leads to a short rise time and high pressure maxima with oscillations immediately following the impact. Further, they observed that even though the magnitude of the maximum pressure varies, the impulse, which is the integration of the pressure over time, does not vary. By conducting similar experiments with a smaller scale, they obtained qualitatively very similar pressure characteristics compared to the previous large scale impact pressure measurements but the magnitude of the impact pressure was different. Subsequently, Chan (1994) examined pressure caused by a plunging breaking wave on a vertical wall in deep water based on laboratory measurements. He identified two scales of pressure, a slowly varying component in the order of stagnation pressure and a transient impact component with higher pressure. He concluded that the former scale is associated with wave evolution and latter scale is influenced by trapped air. Later, Chan et al. (1995) conducted laboratory tests to investigate pressure associated with plunging breaking waves on a vertical cylinder. Mechanics of the impact process was explained in terms of incident wave kinematics.

Kirkgoz (1990), Kirkgoz (1991), Kirkgoz (1992), Kirkgoz (1995) measured impact pressure, and deflections due to plunging breaking waves on both vertical and inclined wall, in a laboratory. Relations between impact pressure, force, and duration were investigated. The influence of water depth on the maximum values of the above three parameters were examined. It was found that the maximum values decrease rapidly as the wave breaks with the wave front parallel to the wall during the breaking process, and the maximum pressure occurs at the still water level. He found that the longer lasting low impact forces are more effective in producing larger deflections, whereas high amplitude impact forces with short durations have minor and local influences. He mentioned that comparing the impact loads on a vertical wall and sloped walls, the resulting forces on sloped walls can be greater than those on a vertical wall. He observed the maximum pressure at slightly below the still water level for all the sloping walls.

Zhou et al. (1991) measured pressure distributions on surface piercing vertical cylinders due to breaking waves. Similar to many other researchers they noticed that the highest impact pressure is subject to considerable variability. A high impact region was found to be localized in time and space. They concluded that the variability is due to the random dynamics of the breaking wave front and the entrapped air. They also concluded that even though the repeatability of the incident wave hydrodynamics was not good, based on statistical methods the large impact pressure could be calculated with good accuracy.

Hattori et al. (1994) conducted laboratory experiments to improve the understanding of impact pressure due to breaking waves. They found that the physics

and characteristics of the impact pressure greatly depended on the colliding conditions of the breaking waves. They studied three types of colliding conditions: flip through, collision of the vertical wave front, and plunging wave collision. They found that impact pressure increases considerably when a small amount of air is entrapped between the wave and the structure wall. Highest pressure of short duration was observed when a vertical wave front strikes the structure wall while trapping a small amount of air in the form of either bubbles or a thin lens shaped air pocket. They observed that the larger the entrapped air, the lower the impact pressure and longer the time it takes to attain the maximum pressure. In addition, they found that more air is entrapped in a plunging breaker, hence the magnitude of the impact pressure is low and it takes a longer time to reach the maximum, while this air damps the pressure oscillation. Based on their experiments, they concluded that the adiabatic processes of the air pocket play an essential role in the physics of high impact pressure.

Azarmsa et al. (1996) did an experimental study on impact pressure measurements on spilling and plunging breaking waves on a vertical wall. They concluded that the impact pressure can be well expressed in terms of internal kinematics of breaking waves. Since they observed impact pressure for both spilling (without entrapped air) and plunging (with entrapped air) breaking waves, they concluded that entrapped air does not play any role in generation of the impact pressure, although pressure oscillations may be linked to entrapped air dynamics. They observed that the size of the impact zone is smaller for spilling breaker than that for plunging breaker. By applying a numerical model, they calculated the internal kinematics of breaking waves

and showed that the vertical components of velocity and acceleration of water particles should be considered in computing of the impact pressure.

Bullock et al. (2001) examined the effects of level of aeration and violence of impact on maximum impact pressure. They developed a relationship which estimates the reduction of impact pressure due to aeration. More recently, Bullock et al. (2007) conducted laboratory tests to investigate the characteristics of wave impacts due to breaking waves impinging on a vertical wall and an inclined wall. They concluded that the characteristics of the impact depend on the breaker condition. They identified two types of impact pressures: low aeration impact characterized by localized high peak pressure and short rise times, and high aeration impact characterized by longer rise periods and sub atmospheric pressures. Giving attention to entrapped air, they concluded that a high level of aeration does not always reduce the peak pressure, but it increases the rise time and duration, hence the impulse force on the structure. In addition, they reported that alternative compression and expansion of the entrapped air could generate sub-atmospheric pressure. They also observed that the highest impact pressure occurs around the still water level, and pressure on a sloping wall is lower than that on a vertical wall, even though the impulse in the entire event is independent of the slope. They found that even though the pressure distribution is different for identical waves, the impulse is almost the same.

Hull and Muller (2002) conducted detailed laboratory experiments of breaker shapes and wave impact pressure on a vertical wall. Photos were taken simultaneously with the pressure measurements. Velocity was measured using Particle Image

Velocimetry (PIV) technique. They concluded that all particles at the wave front aim at one point on the sea wall, thus most probably the high impact is caused by the impact of the horizontally moving wave crest. They observed that the maximum pressure for plunging breakers appears at the still water level, but they also observed high pressure for other breaker types above and below still water level. The point of maximum pressure was observed to shift from a position above still water level (SWL) for a flip through to SWL for breakers with small and large air pockets.

Wienke and Oumeraci (2005) examined breaking waves acting on a slender cylindrical pile. They split the load into quasi-static and dynamic components. They concluded that the quasi-static component can be approximated by the Morison equation, but the dynamic component is associated with the impact of a mass of water on the cylinder. Further they developed an analytical formula for the impact force.

Lugni et al. (2006) conducted laboratory experiments to investigate the kinematics and dynamics of impact of breaking waves on a vertical rigid wall. They observed church roof type pressure variations for most measurement locations, and the highest pressure was above the still water level. They noticed that the pressure does not depart much from the hydrostatic pressure during the wave advancement, but it differs a lot during the wave focusing stage due to intense locality and three dimensionality of the phenomenon. With the measured variations, they mentioned that for the cases without air entrapment a gradual pressure decrease appears after the impact, whereas for the cases with air entrapment the pressure oscillates.

Recently, Cuomo et al. (2010) conducted laboratory experiments to quantify wave impact forces on a steeply-battered wall. They compared the results with predictions from various empirical and analytical methods. They concluded that no existing methods are able to provide accurate predictions over the range of measurements. They introduced prediction formulae for quasi-static impact forces and overturning moments. The formulae were validated with existing measured data.

Although most of the impact pressure studies are experimental, there exist a few numerical studies. Bredmose et al. (2009) developed a numerical model to calculate the impact pressure, with waves being modeled as irrotational flow. They considered different types of impact that may or may not lead to air entrapment. Impact pressure was calculated using a flow model based on energy conservation of a homogeneous mixture of incompressible liquid and ideal gas. They presented wave propagating towards a vertical wall, forming flip through type (no air is trapped), and overturning breakers (trapping large air packets) by varying the initial offshore wave height. They concluded that the impact pressure is very sensitive to the incident wave conditions. Further they concluded that even though the maximum pressure is sensitive to the wave conditions, the force and impulse are less sensitive to the wave conditions. Based on experiments they observed sub atmospheric pressure due to expansion of the trapped air following its initial violent compression. They observed highest impact pressures for waves that trapped a small amount of air.

Duan et al. (2009) developed a numerical model to investigate impact pressure due to a plunging breaking wave hitting obliquely on a coastal structure. The problem

was modeled as an oblique collision of an asymmetrical water wedge and an asymmetrical solid wedge. Variations of wave elevation, pressure distribution, forces, and effects of different impact angles were investigated. Khayyer and Gotoh (2009) developed a numerical model based on a modified Moving Particle Semi-implicit (MPS) method to study impact pressure. By introducing new formulations for pressure gradient and the source term in Poisson pressure equation and by allowing a slight compressibility, they proposed a modified MPS method for the prediction of wave impact pressure on a coastal structure. The improved performance was verified by comparisons with experimental data.

Even though a number of numerical models have been developed to predict impact pressure, most of them are based on simplified assumptions in both governing equations (such as inviscid and incompressible fluid, and single-phase flow) and in boundary conditions. None of the models is able to predict impact pressure with a high accuracy. The understanding of impact pressure is still poor due to the complex and violent process of wave breaking.

Estimating impact pressure is difficult not only in numerical models but also in laboratory measurements. In laboratory studies a common limitation is the spatial resolution of measurements. Since impact occurs locally over a small area whereas the location varies with a slight variation of the incident wave parameters and the turbulent nature of the flow, it is difficult to obtain impact pressure accurately. Further difficulties arise in inaccurate high frequency response of pressure sensors and data acquisition devices. Measuring impact pressure due to breaking waves is even harder. In most of the

experimental studies, it is very difficult to measure impact pressure due to complex temporal and spatial dependence of impact zone. According to observations, the shape of the wave which affects rise of high impact pressure is also uncertain. Some researchers observed the high impact pressures when there is a large packet of entrapped air, whereas some researchers observed high impact pressure when there is a small amount of entrapped air. The location of the high impact pressure is also inconclusive. In some studies it was observed that high impact pressure appears at the still water level, while in some studies it was observed that high impact pressure appears above the still water level.

When a wave breaks near a structure the flow becomes turbulent and two-phase. Knowledge of void ratio is necessary to correctly define the flow parameters such as density, mass, or momentum in two-phase flows. However due to the difficulties in measuring the void ratio in breaking waves, little information is available regarding this. Most of these studies are limited to breaking waves. Void ratio for flows where breaking waves interacting with a structure has been rarely studied.

So far, measurements of void ratio are obtained by using variety of different techniques including video techniques, acoustic techniques and conductivity techniques and using a single probe or double probes. Lamarre and Melville (1992) developed an impedance probe and measured the temporal and spatial variation of void ratio for breaking waves in laboratory and in field. The probe is capable of measuring the void ratio in the initial period after wave breaking, where large void ratio prevails. Further, with the underwater video photography in field they demonstrated the evolution of

distinct bubble plumes and the presence of large bubbles with a radius of 6 mm and above.

Chanson et al. (1997) studied air bubble entrainment at a pseudo plunging breaker and bubble detrainment process. They observed unsteady air water flow patterns and high levels of aeration. Subsequently, Chanson and Manasseh (2003) carried out laboratory experiments to measure air entrainment in a plunging jet. They used a conductivity probe and an acoustic technique to measure void ratio. Comparing the measurements of the two techniques they concluded that the acoustic technique can provide accurate void ratio data in high void ratio flows, and this acoustic technique could be used in hostile industrial or in the field where more delicate instruments are impractical. Deane (1997) did acoustic and optical measurements of individual breaking waves in the surf zone. He took pictures of the bubble plume formed beneath the breaking surf, which provided plume size, bubble size distribution and void ratio. Void ratios of 0.3-0.4 were measured.

Deane and Stokes (2002) conducted laboratory experiments and field measurements to investigate bubble size distribution in breaking waves using a video technique. They provided a quantitative description of bubble formation mechanisms in the laboratory and identified two mechanisms controlling the size distribution. They concluded that after the initial injection phase the large and small bubble parts of the bubble size distribution followed a power law with exponents of -10/3 and -3/2 respectively, where as after about 1.5 s these values fall to -6 and -2.3. Mori et al. (2007) carried out a series of laboratory experiments and simultaneously measured free surface

elevation, water velocity, void ratio and bubble distribution for a regular breaking wave on a plane slope using a dual tip resistivity probe. They made measurements in two wave flumes to check the scale effects on air entrapment. They mentioned that the effect of scale on void ratio is significant, where the void ratio of the mid scale experiments was 2-4 times larger than the small scale experiments. Further, they observed that the bubble size follows a power law, the slope of the time and space averaged bubble size spectrum was independent of scale, and also observed that time averaged void ratio is linearly related to time averaged total kinetic energy. Rojas and Loewen (2007) conducted experiments to measure the temporal and spatial variations of void ratio and bubble size distribution under breaking waves. Measuring the void ratio using single tip fiber optic probe and a double tip fiber optic probe, they concluded that single tip fiber optic probe is able to provide accurate measurement. They provided data in the dense bubble plumes located just below the free surface and also in the disperse parts of bubble plume.

Blenkinsopp and Chaplin (2010) measured size of bubbles entrained in the dense plumes generated by breaking waves using a pair of highly sensitive optical fiber phase detection probes. Details of spatial and temporal evolution of bubble sizes within breaker were discussed. They successfully compared the measurements with previous measurements in low void ratio parts of the flow, and also measured the void ratio within highly aerated regions present in the period shortly after wave breaking. They concluded that some large air cavities with diameters of tens of millimeters are entrapped. They observed that the bubbles resident within the plume rapidly decrease in

size with time and distance away from the point of primary entrainment as the large cavities initially entrained are broken to smaller bubbles.

Even though there is some experimental work on measuring the void ratio of breaking waves, there are few studies of void ratio measurements for flows where the breaking wave interacts with a structure. Ryu and Chang (2008) measured overtopping green water void ratio over a two dimensional model structure in a laboratory. Fiber Optic Reflectometer (FOR) technique was applied. Temporal and spatial distribution of the void ratio over the deck surface was obtained and discussed. They concluded that the void ratio is high near the green water front where as it is low near the deck surface. Similarity profile for depth averaged void ratio is also given.

The objective of the present study is to examine the maximum impact pressure on the deck area of the model structure, and to relate the pressure with the measured velocity on the deck. The spatial and temporal variations of impact pressure were investigated at two vertical planes: one at the center of the horizontal deck surface and the other at 50 mm away from the center for both the wall impingement and deck impingement wave conditions. Ensemble averaged pressure variations as a function of time and space were shown and compared for the two vertical planes and the two wave conditions. Normalized pressure variations were also presented. Two types of pressure variations were identified: impulsive type with high impact pressure and short rising time, and non impulsive type with a bell shape variation of pressure over time. The magnitude of the maximum impact pressure was tabulated and the location where it occurs was extracted. Possibility of obtaining a relationship between the maximum

impact pressure and the rising time was investigated. In the present study, the void ratio was measured for a few pressure measurement locations located near the front of the model. The ensemble averaged spatial and temporal variations of the void ratio are presented and discussed. It was observed that for most of the measurement locations, void ratio stays at a constant value over time. The objective of the study was to relate the measured impact pressure with the measured velocity, after correcting the density of the flow. Based on the images in the BIV measurements (Chapter III), it was observed that the green water flow over the deck behaves like a jet for both the wall impingement and deck impingement wave conditions. Hence, the kinetic energy was related with measured pressure for calculating impact pressure. With the measurements of void ratio, the density of the mixture of water and air was corrected, and the jet impact pressure was predicted based on the momentum of incoming wave and was compared with the measured impact pressure data.

5.2. Experimental setup

In the present study, pressure measurements were taken at two vertical planes for both wall impingement and deck impingement wave conditions: one at the center of the horizontal deck surface and the other 50 mm away from the center. For each plane, locations were selected at every 50 mm in the X direction along the horizontal deck surface starting from the leading front ($X = 0$) of the model, and at every 50 mm in the Z direction starting from $Z = 20$ mm above the deck surface to the highest water level. See

Figs. 5.1 and 5.2 for the pressure measurement locations for the wall impingement and deck impingement cases, respectively. At X = 100 mm, additional measurement points were introduced at Z = 50 mm.

Pressure data was acquired using a piezo-resistive relative pressure sensor (Kistler type 4053A1). The sensor is capable of measuring the addition of hydrostatic pressure and dynamic pressure. The sensor is limited to pressure measurement up to 1 bar, and it measures pressure differential with the surrounding atmospheric pressure as the reference. The natural frequency of the sensor is higher than 15 kHz, hence it is suitable for measuring dynamic pressure in the study. The sensor requires a constant input current, which is provided by an accompanying amplifier (Kistler type 4618A). Measurements were taken at a sampling rate of 10 kHz. A National Instruments data acquisition board (6259USB) was used to acquire the data. The pressure sensor was mounted on a thin vertical Plexiglas plate with a width of 25 mm facing the flow. The sensor is oriented perpendicular to the incoming waves (see Fig. 5.3), hence it measures the impact pressure resulting from the horizontal momentum. Note that in the vertical plane velocity measurements in Chapter III, it was observed that the vertical velocity on the structure deck is much lower than the horizontal velocity after the flow reaches the deck surface. The horizontal impact force thus dominates in the green water process.

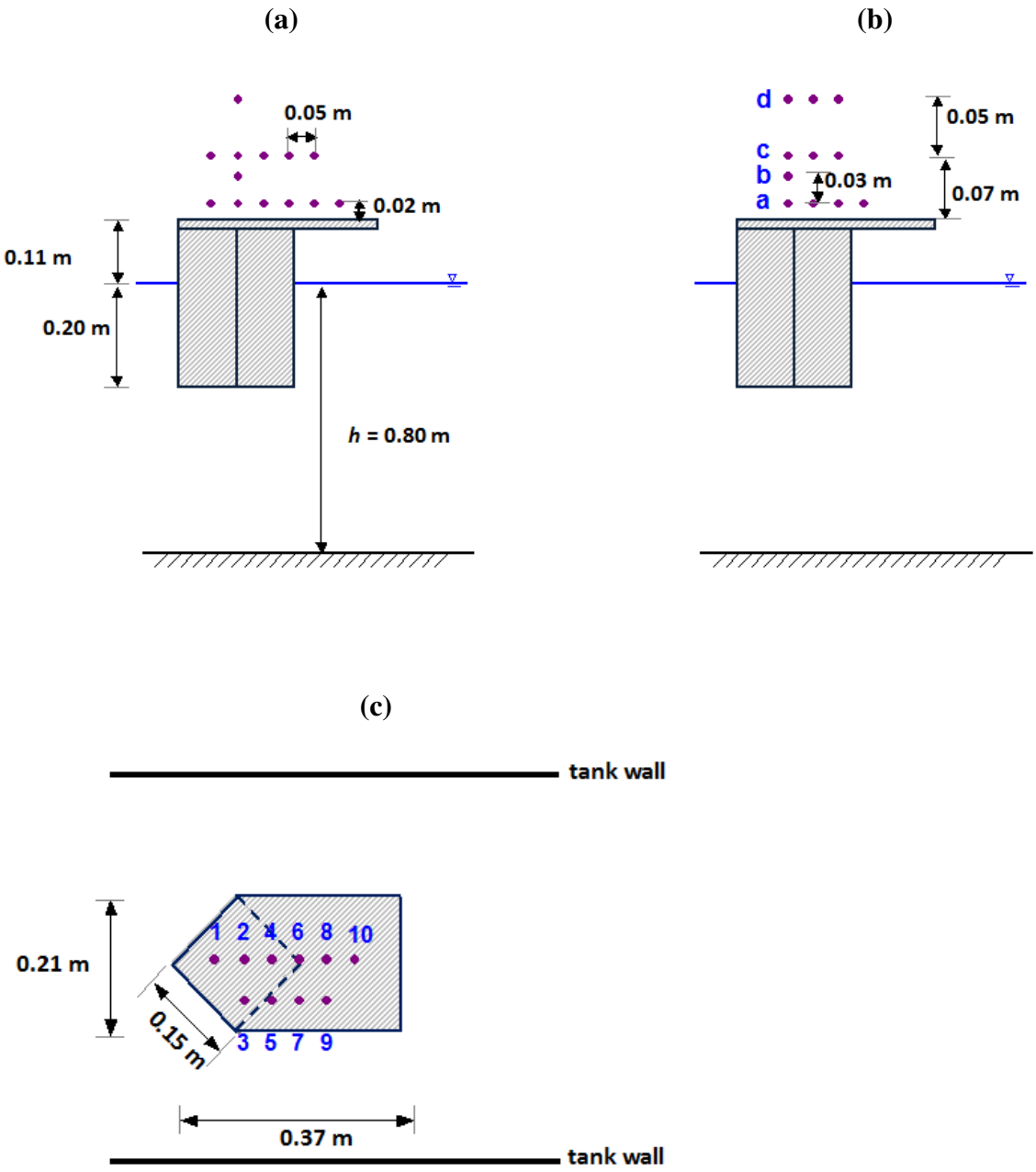

Fig. 5.1. Locations of pressure measurements for the wall impingement wave condition. (a) Side view, vertical plane at centerline; (b) side view, vertical plane at 50 mm away from the centerline; (c) plan view; • , locations of pressure measurements.

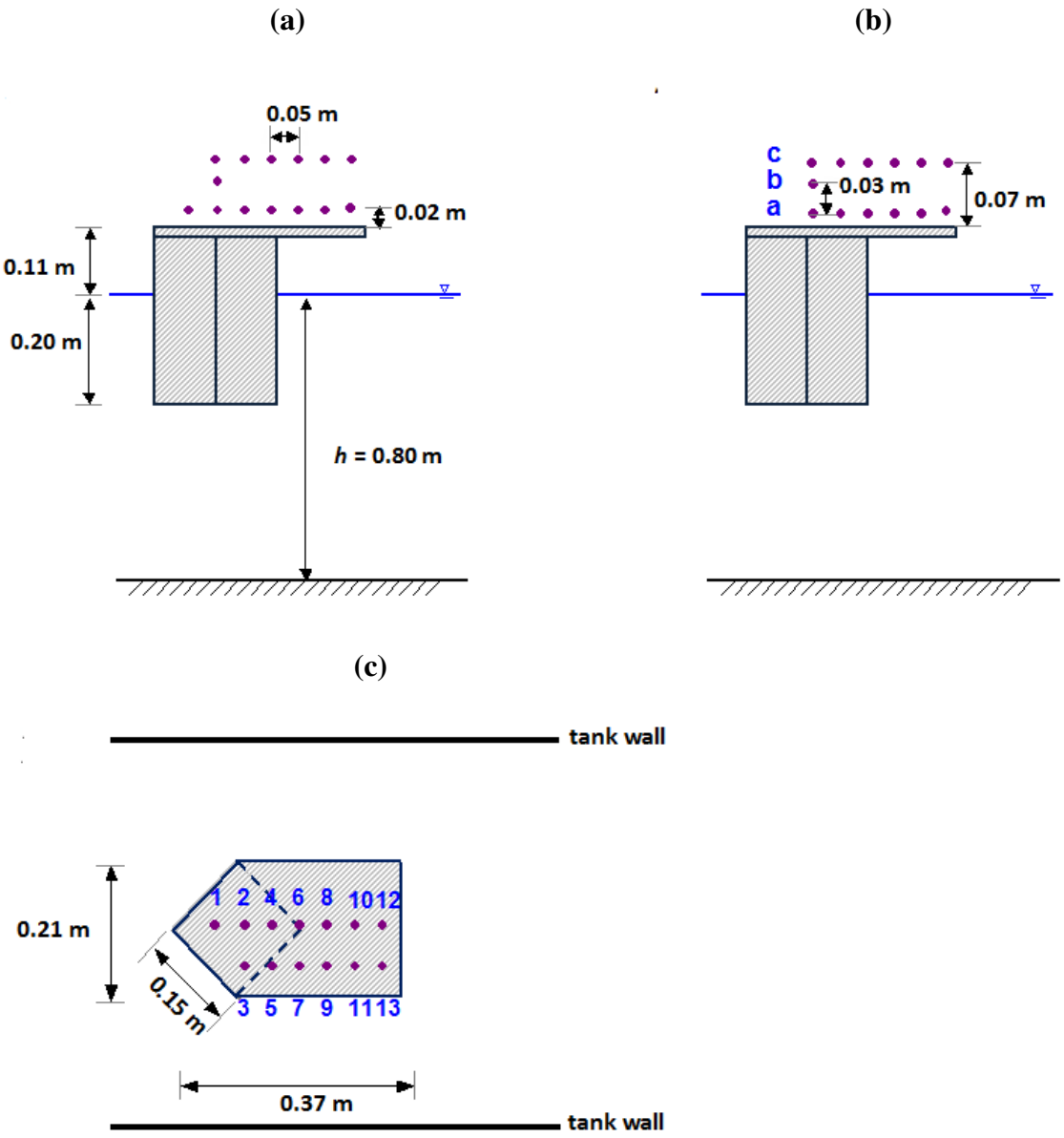

Fig. 5.2. Locations of pressure measurements for the deck impingement wave condition. (a) Side view, vertical plane at centerline; (b) side view, vertical plane at 50 mm away from the centerline; (c) plan view; •, locations of pressure measurements.

Before using the pressure sensor in the experiment, the sensor was calibrated. The calibration was performed in water under a hydrostatic pressure condition for every 0.05 m up to a maximum of 0.75 m water depth. Based on images in BIV measurements the maximum water level above the deck is 0.17 m for the wall impingement wave and 0.08 m for the deck impingement wave, thus calibrating up to 0.75 m pressure head may be adequate to cover the range of impact pressure. In the calibration the sensor was kept under water at each pre-determined depth for 10 s and the pressure readings were recorded at 10 kHz. Each test was repeated five times and averaged. The variation of averaged voltage versus hydrostatic pressure is plotted in Fig. 5.4. The figure confirms that the sensor response is linear. The standard deviation is estimated as 0.002 Volt, which is equivalent to a 2 mm pressure head in water.

Since the green water flow is turbulent, repeating measurements at each given location is needed to average out the fluctuations. The pressure measurements were repeated five times at each measurement point. To examine whether the number of repeated tests is appropriate, ten runs were repeated for the wall impingement wave condition at location 2a in Fig. 5.1. The ensemble averaged value of the ten trials was compared with that of five trials and was plotted in Fig. 5.5. It was observed that the average of five trials is very close to that of ten trials, and it captures the peak pressure reasonably well. Hence for each measurement locations, the pressure measurements were repeated for five times.

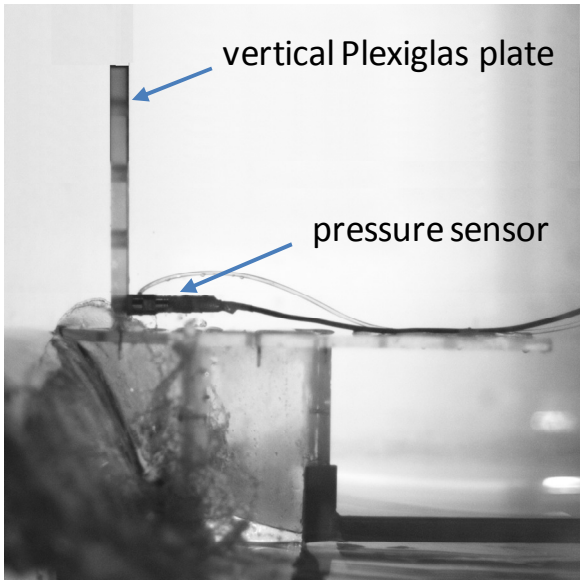

Fig. 5.3. Pressure sensor setup.

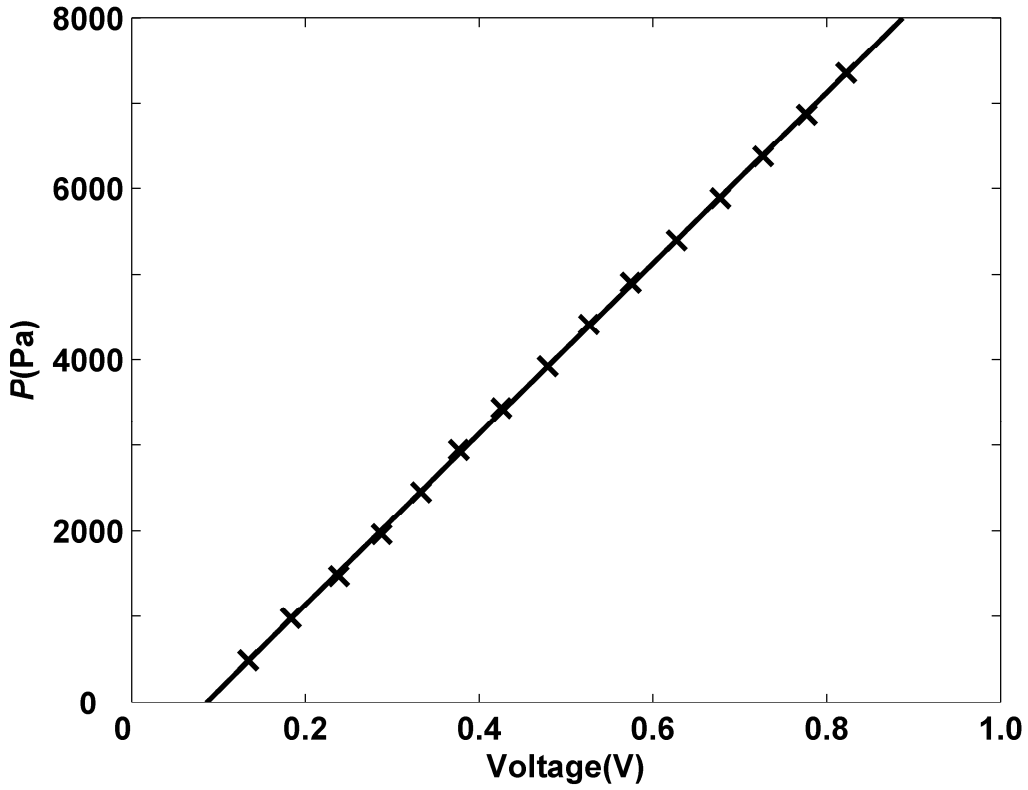

Fig. 5.4. Pressure sensor calibration line. Gradient of the line is 9980.6 and intercept is -858.14.

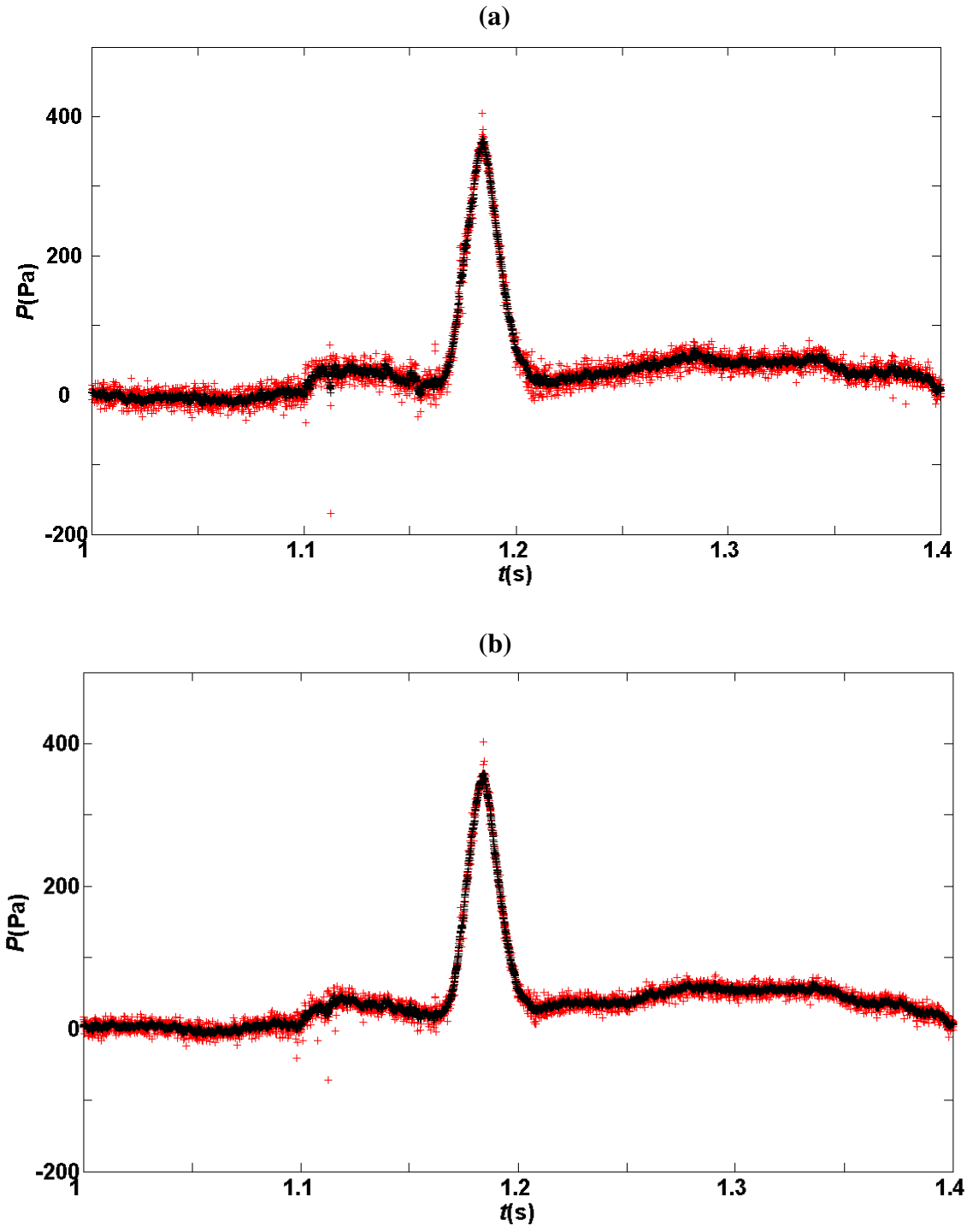

Fig. 5.5. Comparison of ensemble averages of five trials and ten trials. (a) Ensemble average of five trials; (b) ensemble average of ten trials. +, measured; +, moving average over nine points.

The pressure sensor has to be mounted at a required measurement location so the impact pressure can be measured. In the present study the pressure sensor was mounted on a plexiglas sheet. Since introducing a plexiglas plate is likely to affect the flow and therefore the pressure measurements, the effect of width of the supporting plate on the impact pressure was investigated. For the wall impingement wave condition, pressure variations at location 2b was measured for two plate widths: one with the sensor mounted on a 25 mm wide plate and the other with the sensor mounted on a 110 mm wide plate. Since the diameter of the sensor is 15 mm, the minimum width of the plate is limited to 25 mm. The ensemble averaged pressure variations of five repeats is shown in Fig. 5.6 for the two plates. Accordingly, the magnitude of the maximum pressure is almost same for both the 25 mm and 110 mm wide plates. Maximum pressure is 893 Pa for 25 mm plate and is 889 Pa for 110 mm plate, thus there is a 0.45% increase for 25 mm plate compared to 110 mm plate. How ever the overall pressure variations are different. For the wider plate, negative pressure was observed after the peak pressure. Appearance of negative pressure may symbolize the expansion of entrapped air after the initial compression. Since the wider plate is likely cause more disturbances to the incoming flow, the turbulence level and complexity of the flow is higher. Hence there are some fluctuations/oscillations in the measured pressure for the wider plate, compared to the thin plate where the pressure variation is smooth.

A breaking wave impact is said to be very turbulent and short, thus the frequency of data acquisition is important in capturing the peak pressure. In order to identify the adequacy of measurements frequency on the measured impact pressure, pressure was measured at 5 kHz, 10 kHz and 20 kHz for the wall impingement condition at location 2b. Fig. 5.7 shows the ensemble average of five repeats for each frequency. As the figure shows, even though the overall pressure distributions are qualitatively similar, 5 kHz may not be adequate to capture the peak pressure. Both 10 kHz and 20 kHz capture the peak pressure successfully. The magnitude of the peak pressure is 881 Pa, 1179 Pa and 1207 Pa for 5 kHz, 10 kHz and 20 kHz respectively. Hence for 5 kHz and 10 kHz the difference is 27% and 2% in terms of peak pressure with 20 kHz. Thus 10 kHz was selected as the data acquisition frequency in the present study.

In the vertical plane velocity measurements, it was observed that, after about 0.15m away from the leading front edge of the model, the measured velocity has some uncertainty due to the blockage of the focused measurement plane. Hence, in the comparison of pressure and velocity, only locations with accurate velocity measurements were used. Hence for both wall impingement and deck impingement waves, pressure measurement points which are located within first 0.10 m from the leading front edge of the model structure were selected. Thus for the wall impingement wave, the locations 1a, 1c, 2a, 2c, 3a, 3b and 3c were selected. For deck impingement wave condition, the locations 1a, 2a, 2b, 3a and 3b were selected. See Figs. 5.8 and 5.9 for the locations of void ratio measurements for the wall impingement wave and the deck impingement wave conditions respectively.

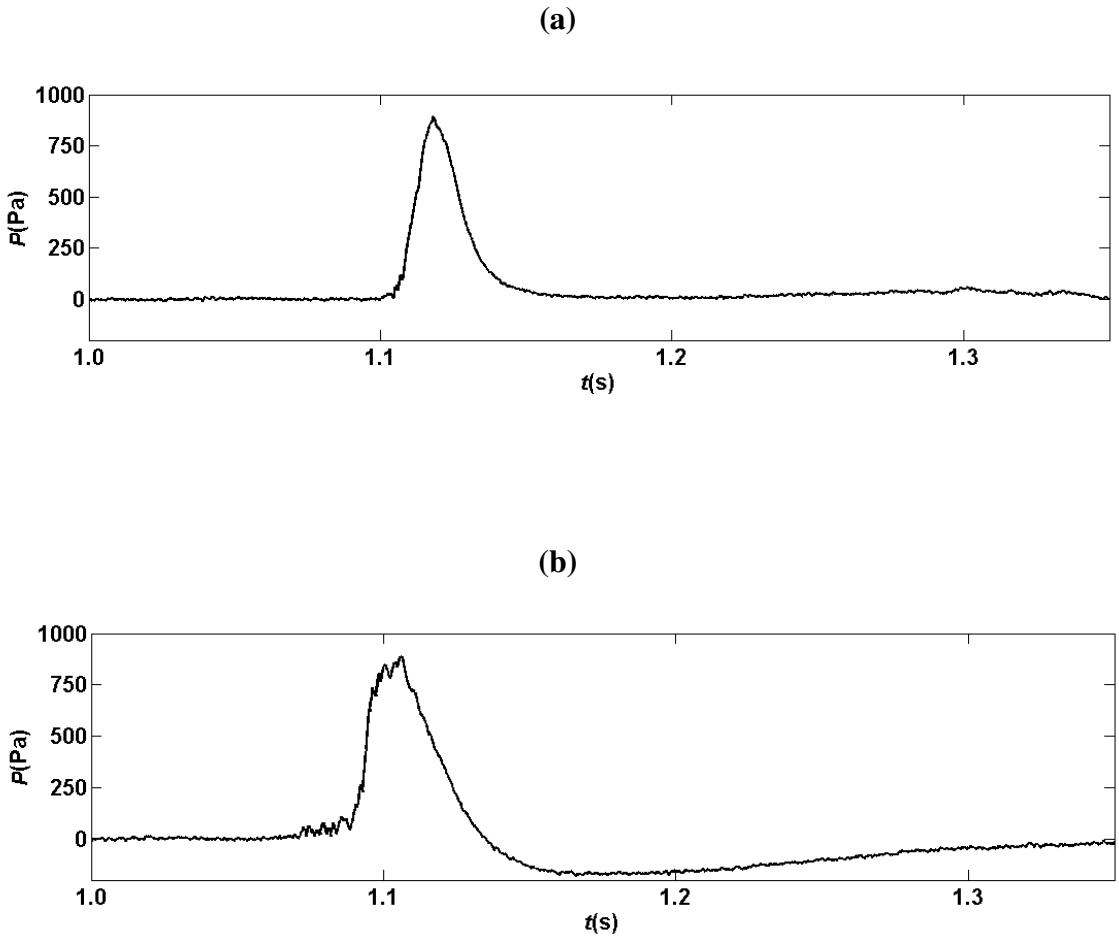

Fig. 5.6. Comparison of effect of width of plate on pressure measurements. Ensemble averaged pressure variations of five trials for (a) 25 mm wide plate; (b) 110 mm wide plate.

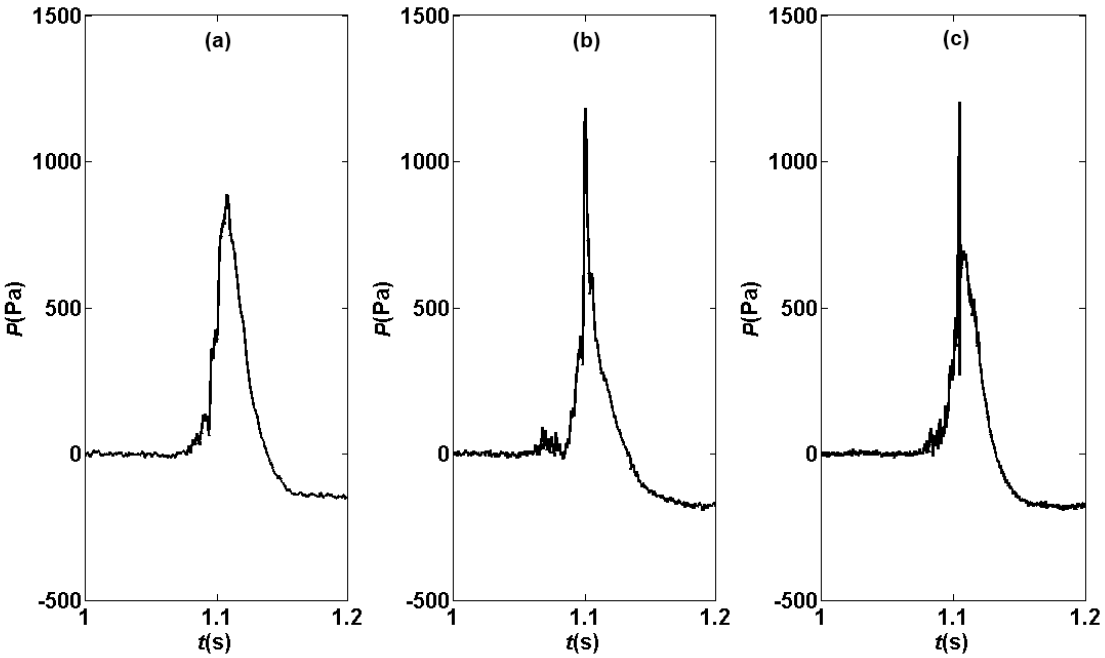

Fig. 5.7. Comparison of frequency of data acquisition on pressure measurements. Ensemble averaged pressure variations of five trials (a) 5 kHz; (b) 10 kHz; (c) 20 kHz.

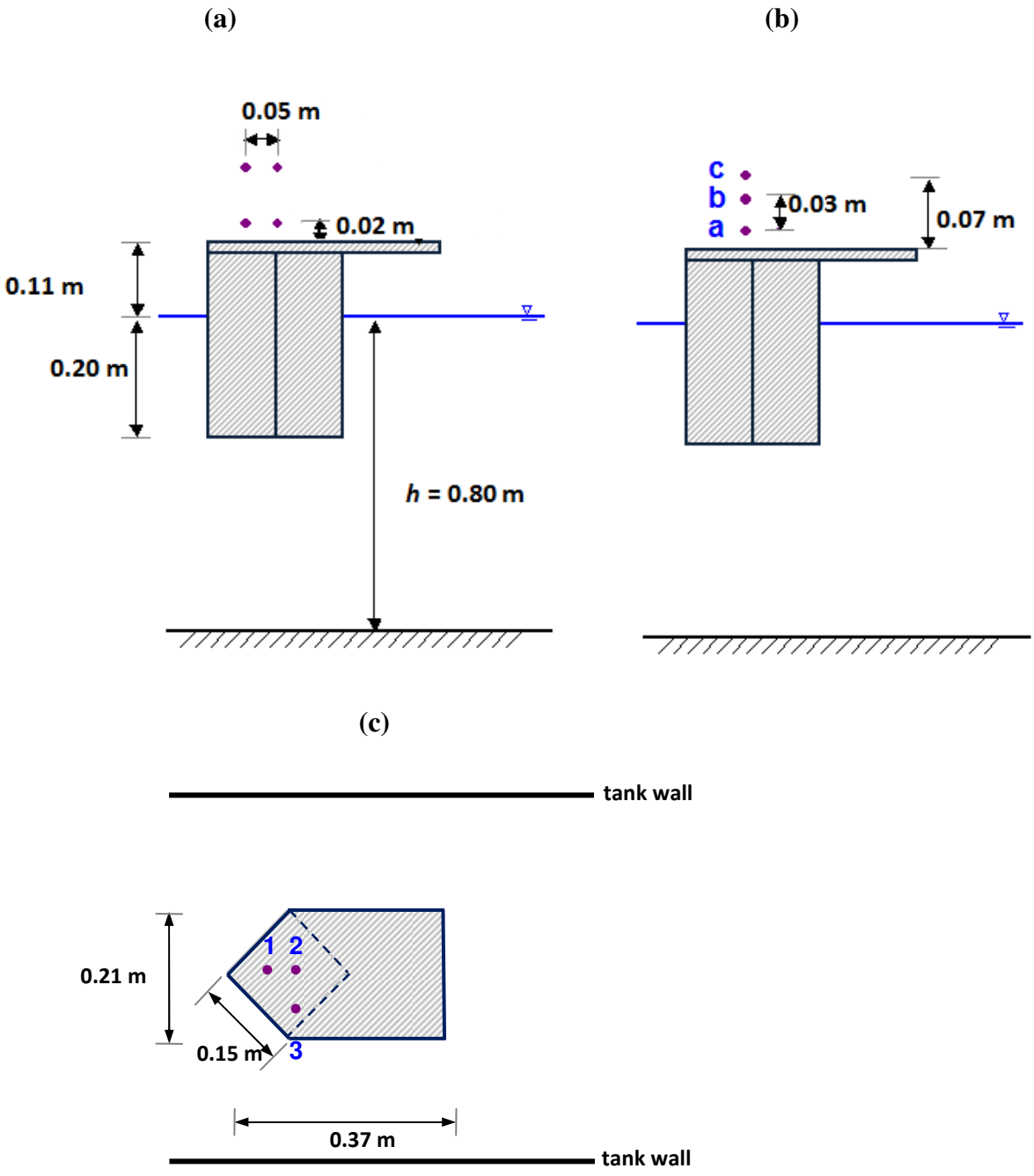

Fig. 5.8. Locations of void ratio measurements for the wall impingement wave condition. (a) Side view, vertical plane at centerline; (b) side view, vertical plane at 50 mm away from the centerline; (c) plan view; • , locations of void ratio measurements.

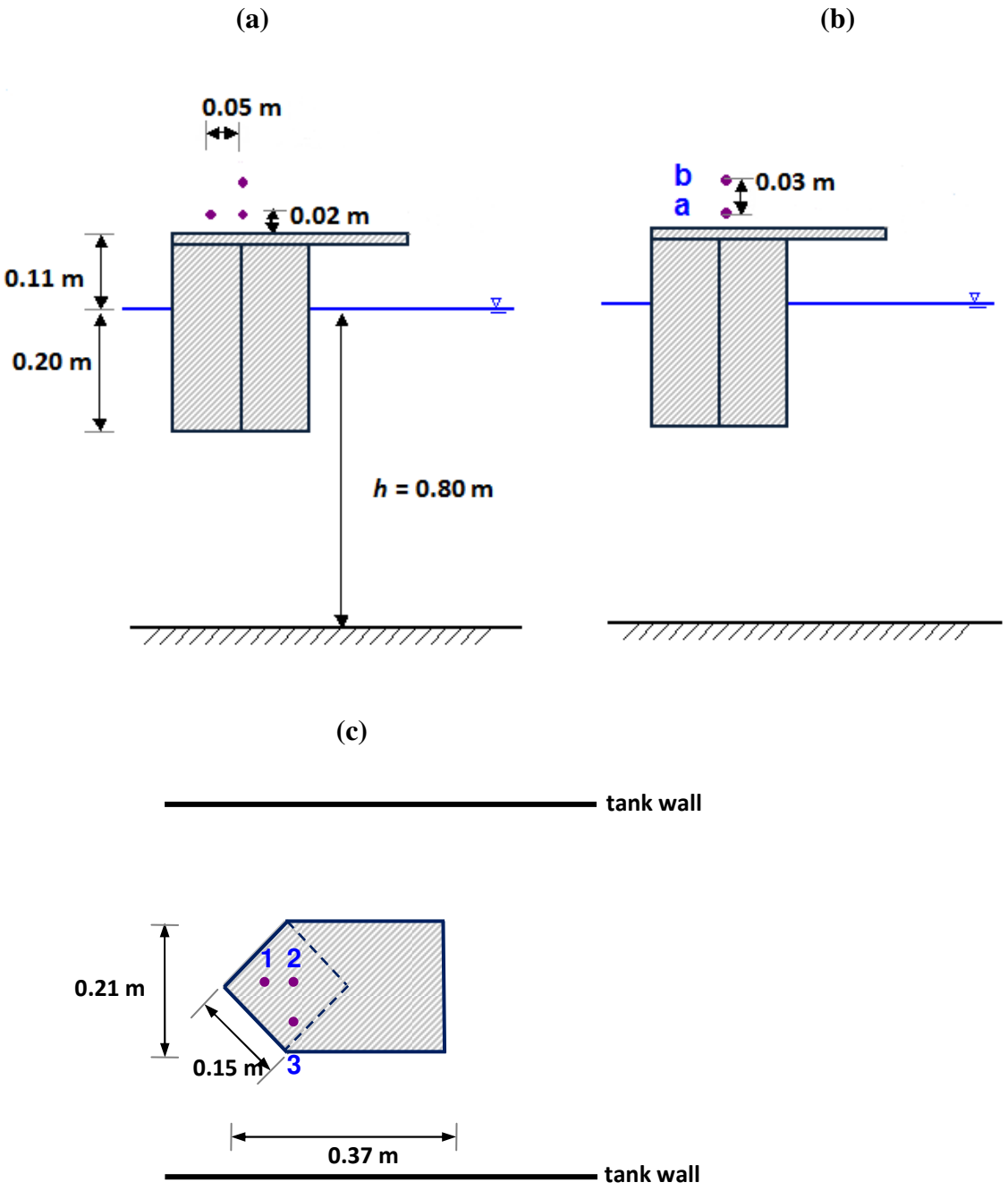

Fig. 5.9. Locations of void ratio measurements for the deck impingement wave condition. (a) Side view, vertical plane at centerline; (b) side view, vertical plane at 50 mm away from the centerline; (c) plan view; • , locations of void ratio measurements.

Void ratio data was acquired using Fiber Optic Reflectometer technique, which was introduced by Chang et al. (2003). FOR technique can be used to measure the void ratio, velocity and the concentration (Chang et al. (2002) and Chang et al. (2003)). The technique is based on the coherent mixing of scattered signals with Fresnel reflection from the tip of an optical fiber. A diode laser, with a coherence length of about 200 μm, which is driven by a constant current, emits an optical signal, which is transferred to a signal mode optical fiber. The optical fiber transmits this signal through a fiber coupler to the testing fluid. The coherently mixed signal returns back to the signal fiber through the fiber coupler. This returning signal is detected and acquired by the data acquisition board. Since the voltage of the returning signal is high for the air medium compared to that of water, it is possible to easily identify the phase of a mixture of air and water. The setup of the FOR system depicted in Chang et al. (2003) is shown in Fig. 5.10. The details of the FOR sensor setup used in the present study is shown in Fig. 5.11. Since only disturbance to the flow is intrusion of a small fiber probe, the disturbance is minimal. The details of the FOR technique can be found in Chang et al. (2003).

A sampling rate of 100 kHz for 10 s was used to obtain the void ratio for each measurement location. Following, Ryu and Chang (2008) the tests were repeated twenty times. In the acquired voltage signal, a high voltage represents air whereas a low voltage represents water, see Fig. 5.12.

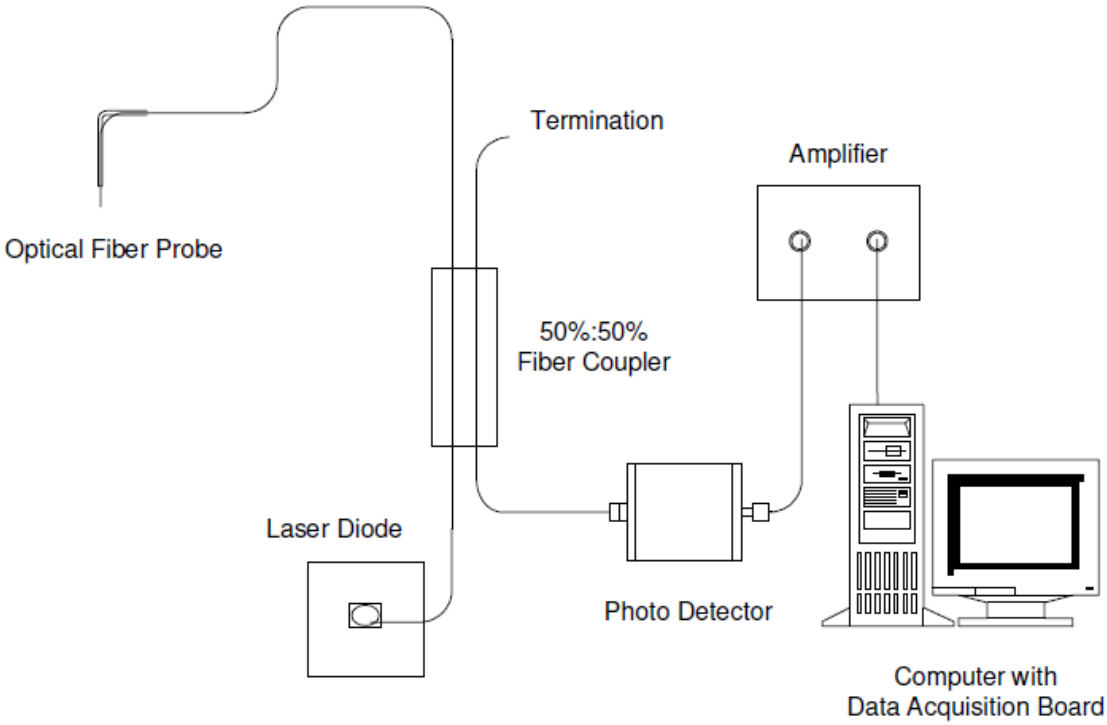

Fig. 5.10. Setup of FOR system. Chang et al. (2003).

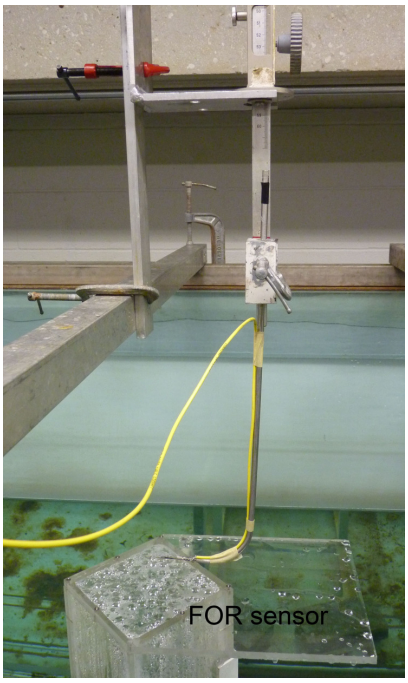

Fig. 5.11. FOR sensor setup.

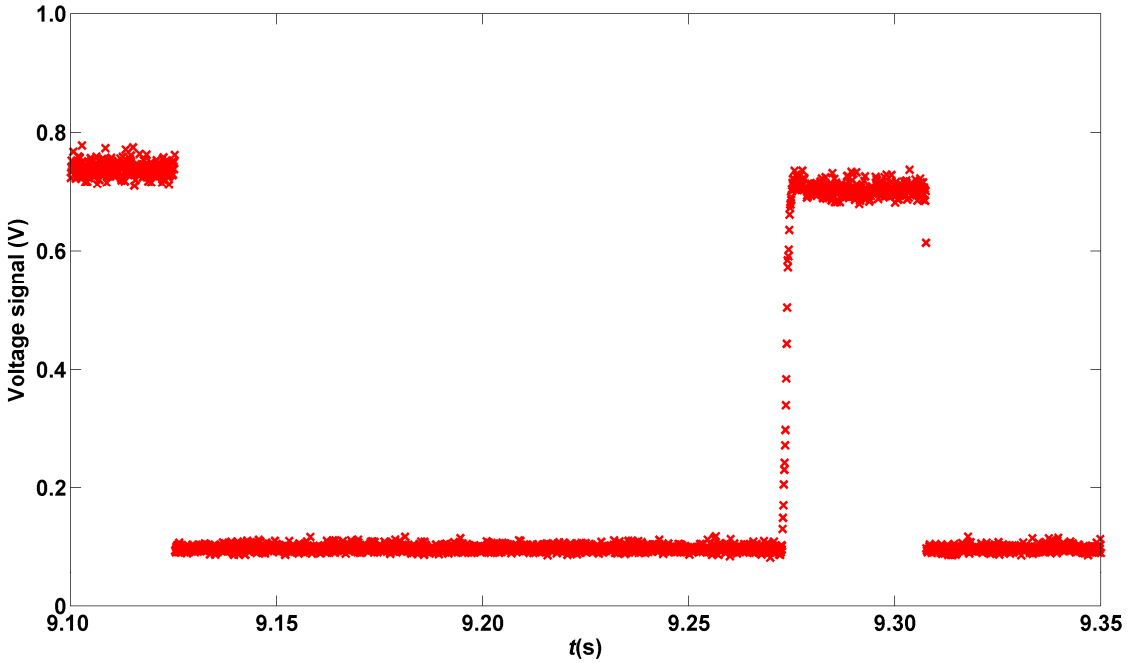

Fig. 5.12. Instantaneous void ratio voltage signal.

The void ratio is defined as the ratio of air-phase residence time (T_{air}) to the duration of air-water mixture (T_{dur}) at the location. Thus, the value of void ratio may be affected by the selected T_{dur}. To obtain the instantaneous void ratio for the twenty repeat tests at each measurement location, first the voltage was set to zero for water and to one for air. In the present study void ratio was calculated by averaging the voltage signal over a short time interval of 0.001 s, i.e. average over every hundred consecutive points. Hence the final temporal resolution is 1000 Hz which is identical to the frequency of velocity measurements.

The definition of void ratio at a given point is expressed as,

$$\alpha_i = \frac{T_{air,i}}{T_{dur,i}} \qquad (5.1)$$

α_i is the instantaneous void ratio, $T_{air,i}$ is the duration of air phase during $T_{dur,i}$, $T_{dur,i}$ is the time interval for void ratio binning, subscript *i* indicates the *i* th repeat. Therefore $\alpha_i = 1.0$ means the probe is in air and $\alpha_i = 0.0$ means the probe is in water.

5.3. Impact pressure - wall impingement case

Fig. 5.13 shows the spatial and temporal variations of normalized pressure on the vertical plane at the centerline of the deck surface for wall impingement wave condition. The figure was plotted with each panel located at the corresponding measurement point as sketched in Fig. 5.1(a). Fig. 5.14 plots the measured pressure time history at all the measurement points in Fig. 5.13 together in one chart. As depicted in the figure only one single prominent pressure peak was observed for all the measurement points, although at some points lower magnitude peaks were also observed. No obvious pressure oscillation was found in the measurements on this vertical plane for the wall impingement condition. Negative pressure was observed for a few points, indicating the expansion of entrapped air. Even though simultaneous movies were taken in the present study, the movies were not well focused for the pressure measurement location. Hence it was not possible to observe the entrapped air. Appearance of negative pressure due to the expansion of entrapped air has been observed and reported previously by other researchers (e.g., Chan and Melville, 1988; Bullock et al., 2007; Bredmose et al., 2009). The magnitude of the maximum measured pressure and the rise time for the measurement locations on the vertical plane at the centerline for the wall impingement condition is summarized on page 114.

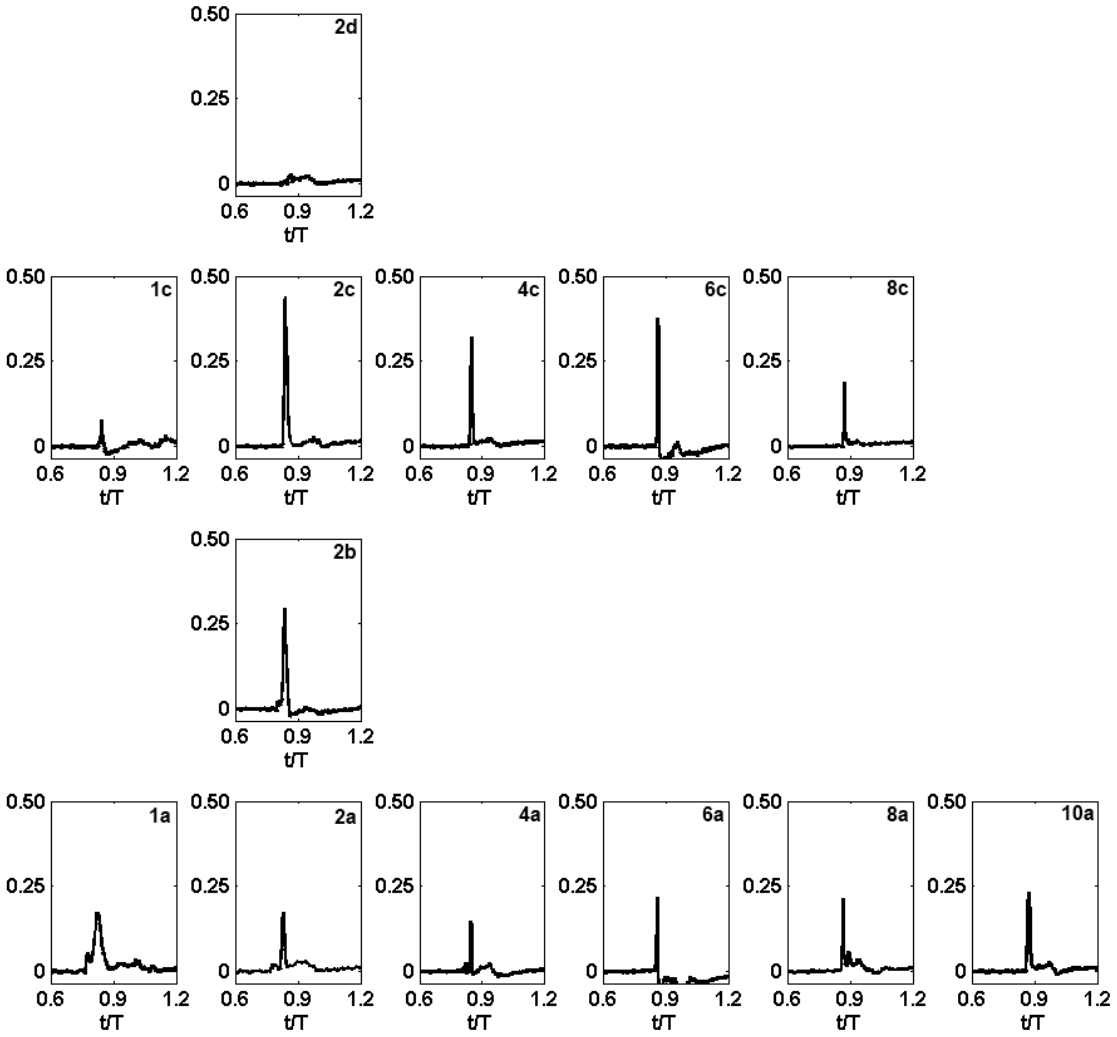

Fig. 5.13. Measured pressure (normalized by $\rho C^2 / 2$) against time (normalized by T) on the vertical plane at the centerline of the deck surface for the wall impingement wave condition. The vertical axis is $\frac{P}{0.5\rho C^2}$. The panels are arranged in accordance to Fig. 5.1(a).

According to Figs. 5.13 and 5.14, the maximum pressure of 0.44 (normalized by $0.5\rho C^2$) or 894 Pa (equivalent to 151 kPa in the prototype) appears at point 2c, located 0.10 m behind the front leading edge and 0.07 m above the deck surface. Measured pressure at $Z = 0.07$ m is higher than that at the top and bottom rows. That is consistent with what was found on the vertical-plane velocity measurements in Fig. 3.1 in which the maximum velocity is neither near the deck surface nor near the upper free surface of the overtopping water on the deck. On the other hand, higher pressure does occur near the deck surface at the sections closer to the frontal edge and the end of the deck, as shown in the bottom row ($Z = 0.02$ m) in Fig. 5.13. This is also consistent with the velocity measurements.

The exact location where the maximum pressure occurs is unknown due to the coarse measurement "grid" in the pressure measurements. The top row ($Z = 0.12$ m) has relatively low pressure; water barely reached this height. No indication of pressure was observed after 0.30 m away from the leading front edge of the model structure.

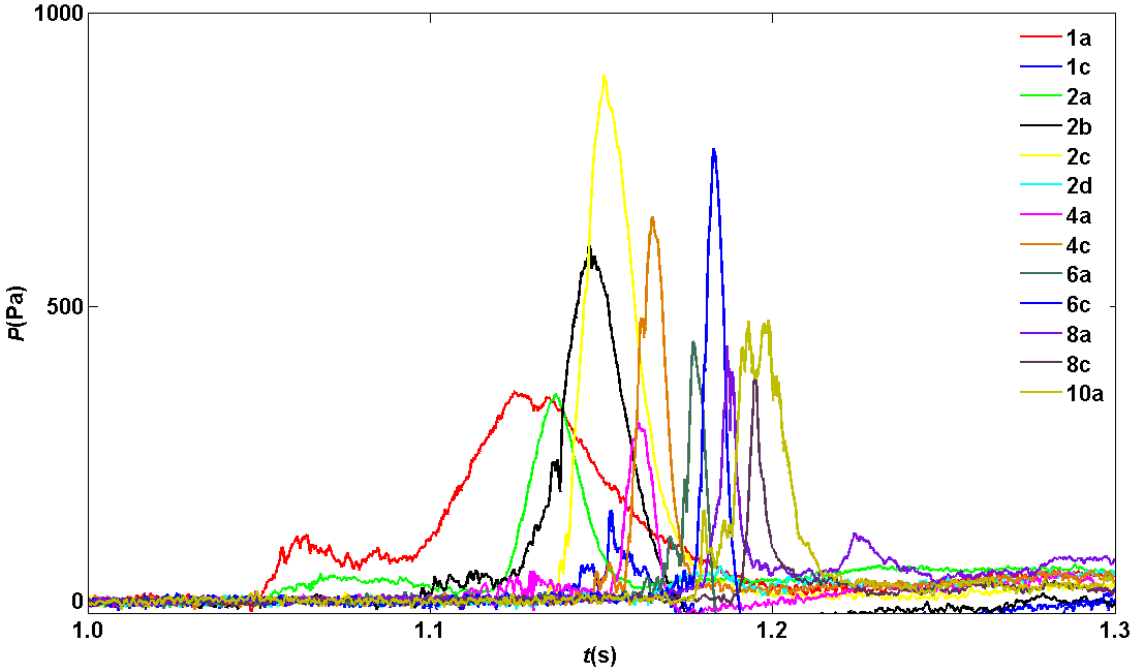

Fig. 5.14. Pressure time history for the vertical plane located at the center of the deck, for wall impingement wave condition. The legend corresponds to the measurement points in Fig. 5.1(a).

According Fig. 5.14, the overall pressure characteristics are similar for all the measurement points: pressure variations are smooth and bell shaped, pressure rises slowly, and pressure reaches the maximum and decreases gradually. All the pressure variations have a single peak. For the wall impingement condition on the vertical plane at the deck centre, no impulsive type (see Fig. 5.15(b)) pressure variations were observed. The impulsive type pressure rises instantaneously with small rising time was observed for deck impingement wave and will be discussed later. On the vertical plane at the deck centre the maximum pressure lies below 500 Pa. Notice that as given in Table 5.1 the rise time decreases towards the end of the deck from 0.0297 s (0.02T) to 0.0047 s (0.003T), where T is the wave period, even though the magnitude of the maximum impact pressure does not necessarily increase. The magnitude of the maximum impact pressure at the elevation of 0.07 m is almost twice to that at the elevation of 0.02 m for locations 2, 4, and 6. As Table 5.1 shows the gradient of the pressure rise is below 250 Pa/ms for all the measurement locations. Later it was observed that for impulsive type pressure the pressure rising gradient is above 250 Pa/ms.

(a)

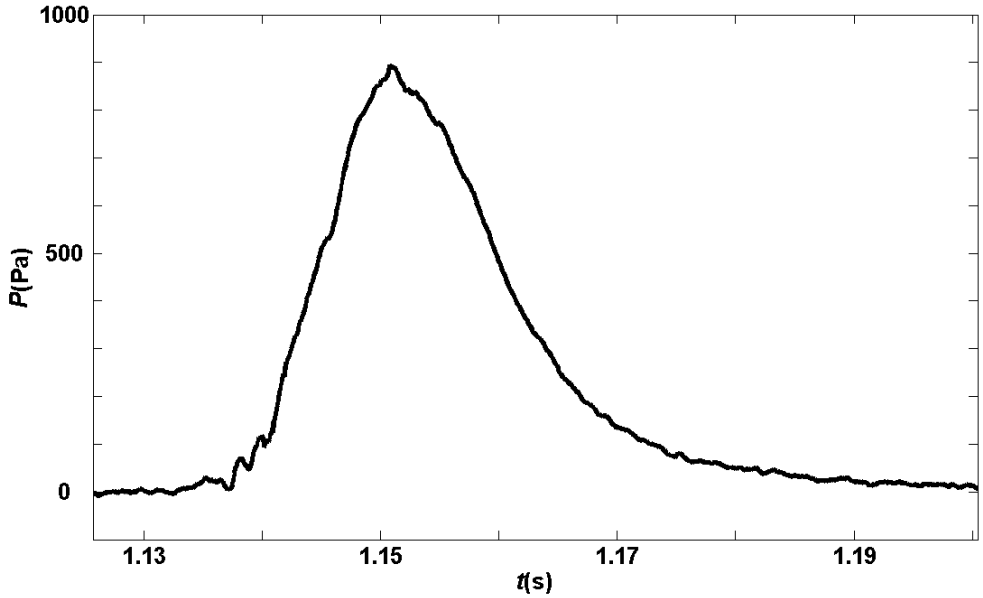

(b)

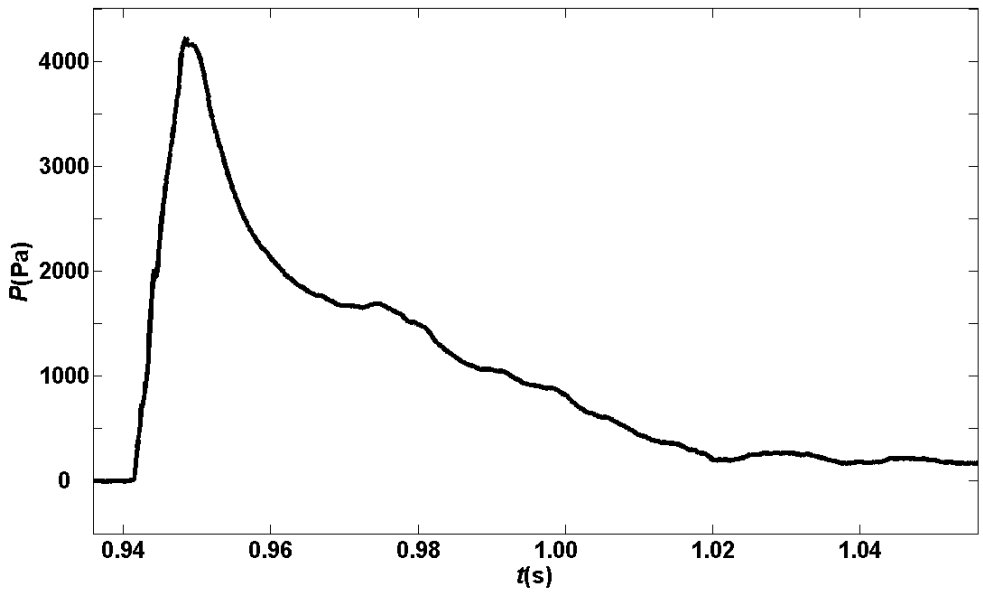

Fig. 5.15. Pressure variation: (a) non – impulsive type; (b) impulsive type.

Table 5.1. Measured maximum pressure corresponding to Fig. 5.1(a). Pressure was normalized by $0.5\rho C^2$.

Location	Maximum pressure (Pa)	Normalized maximum pressure	Rise time (s)	d*p*/d*t* (Pa/ms)
1a	357	0.18	0.0297	12
1c	155	0.08	0.0036	43
2a	352	0.17	0.0196	18
2b	603	0.30	0.0214	28
2c	894	0.44	0.0135	66
4a	303	0.15	0.0087	35
4c	653	0.32	0.0084	78
6a	440	0.22	0.0038	116
6c	769	0.38	0.0061	126
8a	434	0.21	0.0076	57
8c	385	0.19	0.0047	82
10a	475	0.23	0.0047	101

Fig. 5.16 shows spatial and temporal variations of measured (normalized by $0.5\rho C^2$) pressure on the vertical plane at 0.05 m away from the centerline of the deck for the wall impingement wave condition. The figure was plotted with each panel located at the corresponding measurement point in Fig. 5.1(b). Fig. 5.17 shows a detailed view over the peak pressure for all pressure variations in Fig. 5.16.

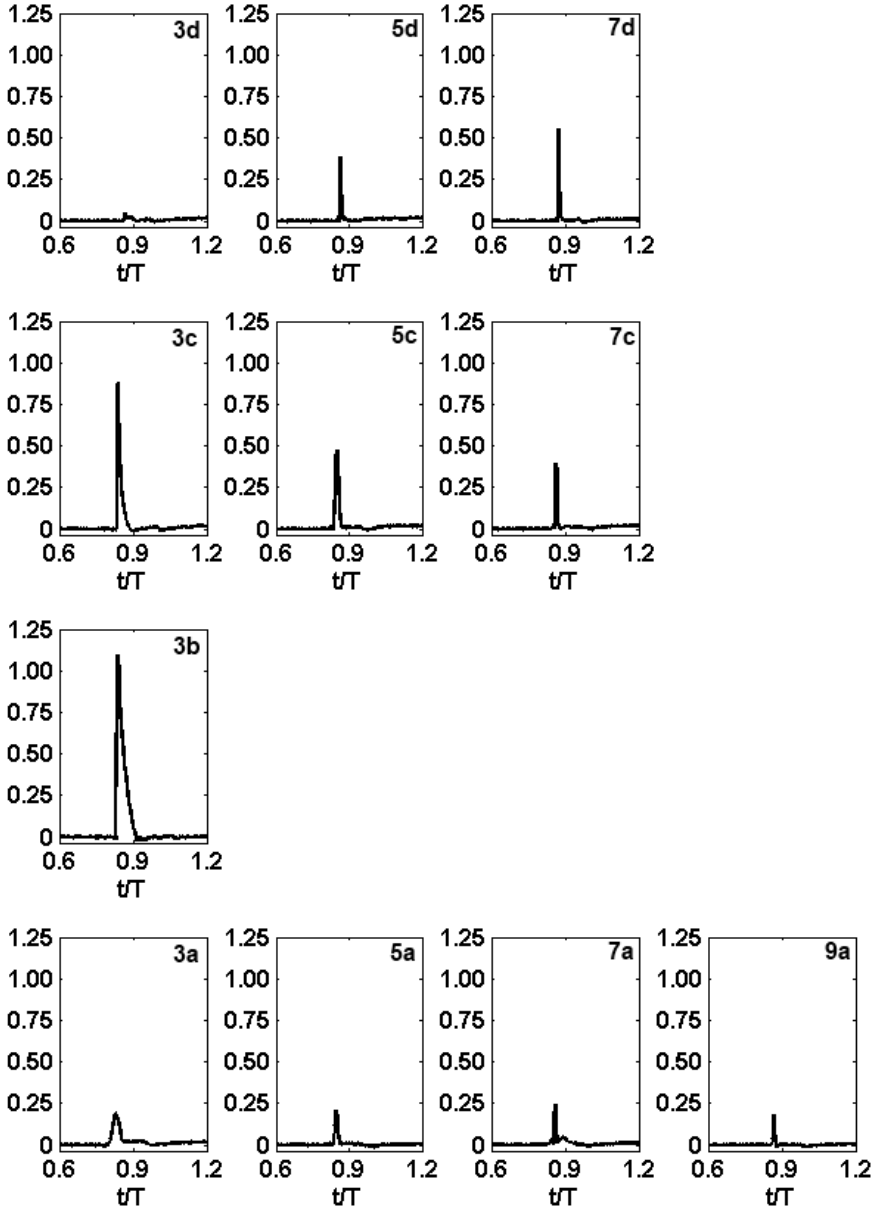

Fig. 5.16. Measured pressure (normalized by $\rho C^2 / 2$) against time (normalized by T) on the vertical plane 0.05 m away from the centerline of the deck surface for the wall impingement wave condition. The vertical axis is $\frac{P}{0.5\rho C^2}$. The panels are arranged in accordance to Fig. 5.1(b).

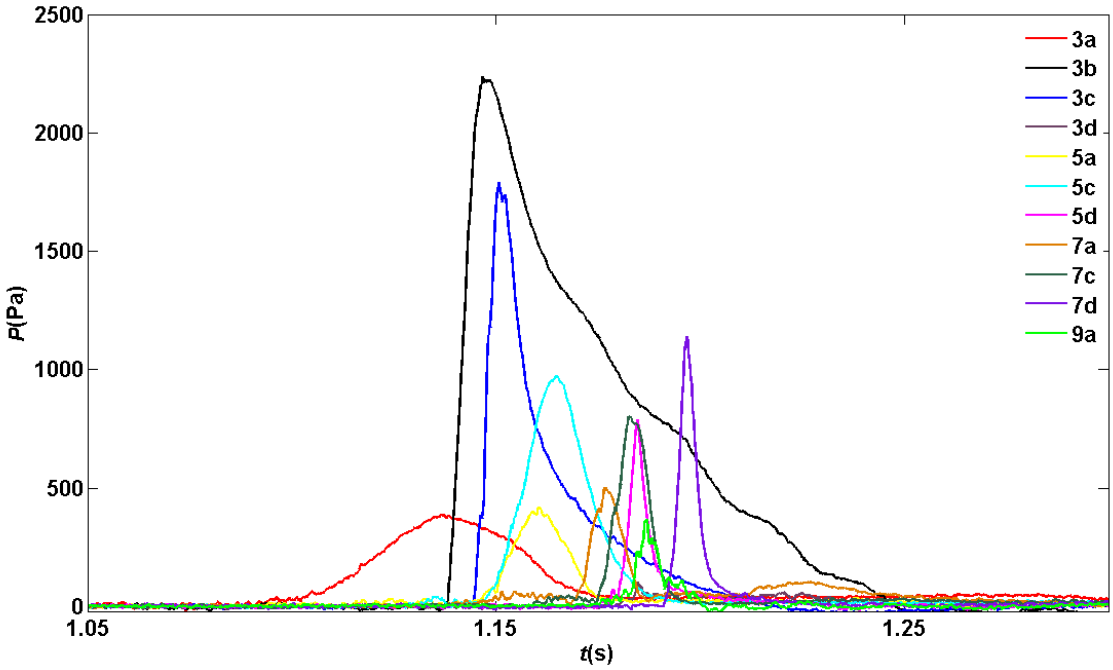

Fig. 5.17. Pressure time history for the vertical plane located at 0.05 m from the center of the deck for the wall impingement condition. The legend corresponds to the measurement points in Fig. 5.1(b).

Table 5.2. Measured maximum pressure corresponding to Fig. 5.1(b). Pressure was normalized by $0.5\rho C^2$.

Location	Maximum pressure (Pa)	Normalized maximum pressure	Rise time (s)	d*p*/d*t* (Pa/ms)
3a	389	0.19	0.0466	8
3b	2237	1.10	0.0086	260
3c	1790	0.88	0.0064	280
5a	418	0.20	0.0108	39
5c	973	0.48	0.0194	50
5d	789	0.39	0.0051	156
7a	500	0.25	0.0085	59
7c	802	0.39	0.0085	95
7d	1138	0.56	0.0057	200
9a	366	0.18	0.0044	83

Table 5.2 summarizes the magnitude of the maximum pressure, rise time and the gradient of the pressure given in Fig. 5.16.

In Figs. 5.16 and 5.17, the maximum pressure of 1.10 (normalized by $0.5\rho C^2$) or 2237 Pa (equivalent to 303 kPa in the prototype) occurred at point 3b located 0.10 m behind the front leading edge (X = 0.10 m) and 0.05 m above the deck surface (Z = 0.05 m). This location is very close to point 2c (at centerline) in both the X and Z positions except point 3b is 0.05 m away (in Y direction) from the deck centerline. However, the magnitude of pressure at point 3b is more than twice that at point 2c. This is consistent with the horizontal-plane velocity measurements in Fig. 3.2 which shows that the velocity is higher at the lateral edge of the structure and lower near the centerline. Since the highest pressure was observed near the front edge, and since many sensitive

equipment and facilities are likely to situate near the bow area, this high pressure may potentially cause intensive damages.

The measured pressure at the vertical plane 0.05 m away from the centerline indicates that the higher pressure zone is neither near the deck surface nor near the upper surface of the green water, similar to what was found in the pressure measurements on the vertical plane at the centerline.

In addition, the measured pressure in the zone closer to the upper free surface is higher (except near the deck front edge) than that near the deck surface; this is different from pressure on the vertical plane at the centerline. The maximum pressure at the bottom row, at $Z = 0.02$ m (near the deck surface) is lower than 1/4 of the maximum pressure at $Z = 0.07$ m, and lower than 1/2 of the maximum pressure at $Z = 0.12$ m (near the upper free surface). Similar to the previous observation, the peak pressure for the elevation of 0.02 m above the deck surface lies below 500 Pa. No indication of pressure was observed after 0.25 m away from the leading front edge of the model structure.

As Fig. 5.17 depicts the pressure time history for all the measurement locations has a single peak. However, on this vertical plane the pressure time history for locations 3b and 3c shows a rapid increase towards the peak pressure. This is identified as the "impulsive type pressure" variation. According to Table 5.2, the gradient of pressure rise is above 250 Pa/ms.

5.4. Impact pressure - deck impingement case

Fig. 5.18 indicates spatial and temporal variations of measured pressure normalized by $0.5\rho C^2$ on the vertical plane at the centerline of the deck for the deck impingement wave condition. The figure was plotted with each panel located at the corresponding measurement point in Fig. 5.2(a). Fig. 5.19 depicts a detailed view over the peak pressure for each pressure variation in Fig. 5.18. Table 5.3 summarizes the magnitude of the maximum pressure, rise time, and gradient of the pressure in Fig. 5.18.

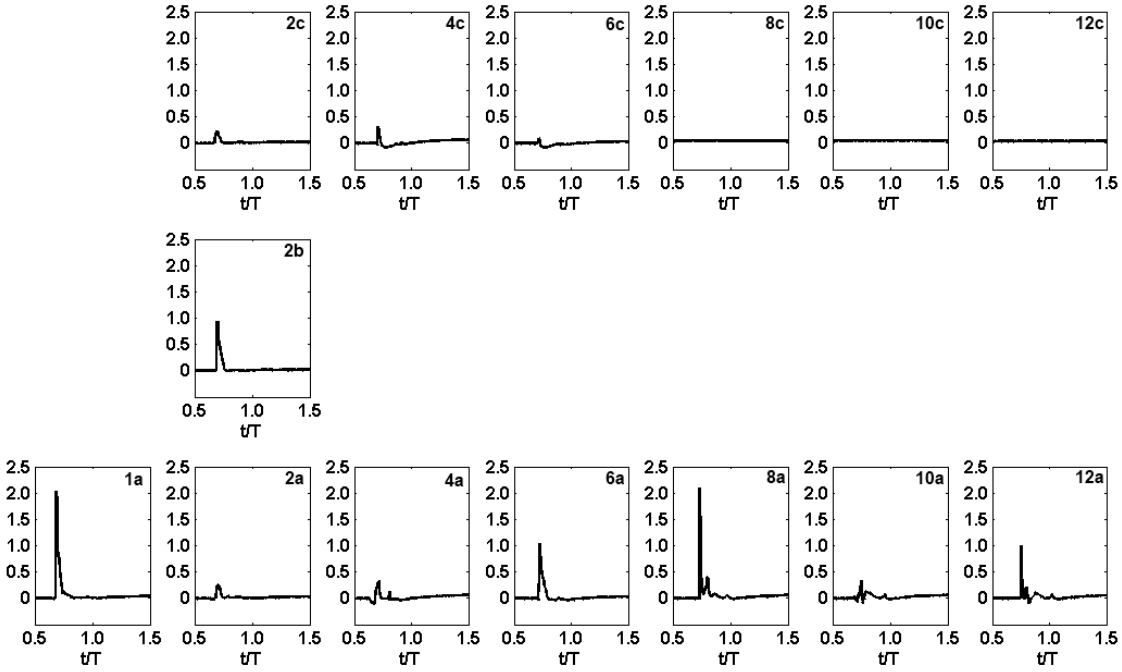

Fig. 5.18. Measured pressure (normalized by $\rho C^2 / 2$) against time (normalized by T) on the vertical plane at the centerline of the deck surface for the deck impingement wave condition. The vertical axis is $\frac{P}{0.5\rho C^2}$. The panels are arranged in accordance to Fig. 5.2(a).

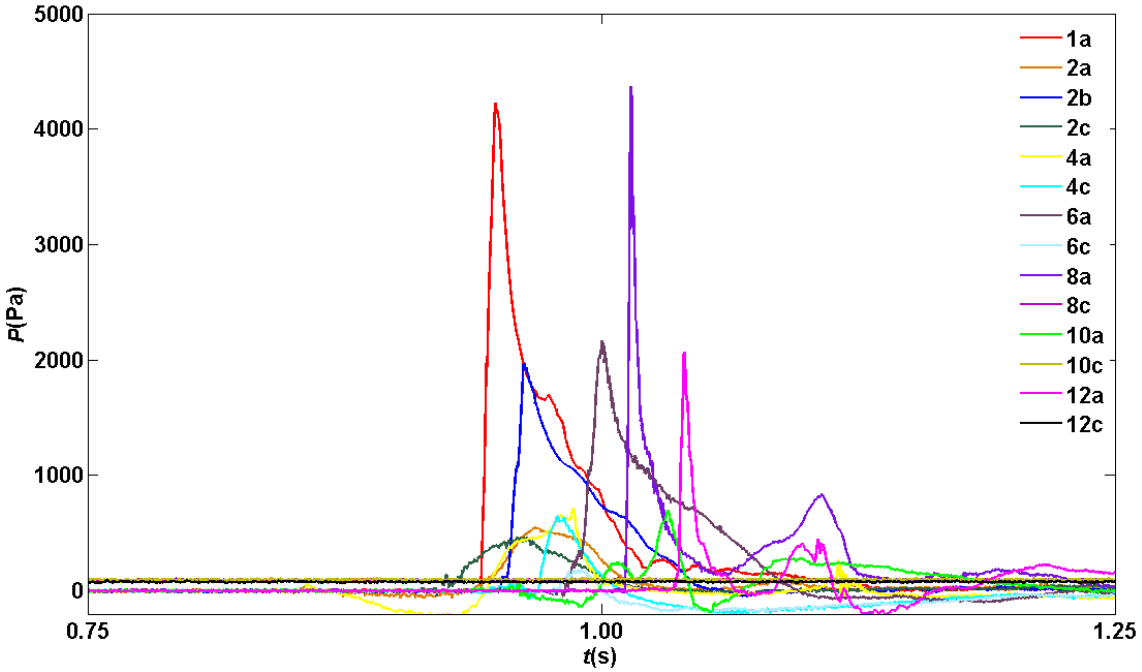

Fig. 5.19. Pressure time history on the vertical plane located at the center of the deck for the deck impingement wave condition. The legend corresponds to the measurement points in Fig. 5.2(a).

As Fig. 5.18 depicts, the maximum normalized pressure of 2.1 (normalized by $0.5\rho C^2$) or 4364 Pa (equivalent to 738 kPa in the prototype) occurred at point 8a, located 0.25 m behind the front leading edge and 0.02 m above the deck surface. A similar impact pressure peak of 4213 Pa appears at location 1a, located near the front edge at 0.05 m behind the front leading edge and 0.02 m above the deck surface. Notice that in the vertical plane velocity measurements as in Fig. 3.4, the maximum horizontal velocity of 1.44 C was observed at X = 0.24 m. This location is very close to the location where the peak pressure is observed. Further, it was observed that for the deck impingement wave condition the breaking wave impinges at 0.03 m on the deck behind

the leading edge of the model. This location is very close to where the second peak pressure was observed. Compared to the measured pressure history for the wall impingement wave condition, for deck impingement condition pressure near the deck surface is higher for all the measurement locations. No indication of wave impact is evident for 0.07 m height above deck surface.

The deck impingement wave condition could cause severe damages since higher pressure was observed compared to the wall impingement condition, especially many sensitive facilities are located on deck surface. For the deck impingement wave case, pressures were observed towards the very end of the deck, where as for the wall impingement wave, no indication of pressure was observed after 0.30 m from the front edge. Similar to the wall impingement wave, no pressure appears above 0.07 m elevation.

As Fig. 5.19 indicates, for deck impingement condition most of the locations show impulsive type pressure variations. The pressure time history shows an almost instantaneous rise. As Table 5.3 summarizes, the pressure gradient is above 250 Pa/ms for locations 1a, 8a, and 12a. Similar to the wall impingement condition, most of the pressure variations have one single peak and no oscillations.

Table 5.3. Measured maximum pressure corresponding to Fig. 5.2(a). Pressure was normalized by $0.5\rho C^2$.

Location	Maximum pressure (Pa)	Normalized Maximum pressure	Rise time (s)	d*p*/d*t* (Pa/ms)
1a	4213	2.02	0.0071	593
2a	544	0.26	0.0313	17
2b	1972	0.95	0.0088	224
2c	469	0.23	0.0332	14
4a	720	0.35	0.0426	17
4c	649	0.31	0.0096	67
6a	2158	1.04	0.0182	119
6c	184	0.09	0.0115	16
8a	4364	2.10	0.0031	1393
10a	701	0.34	0.0145	48
12a	2060	0.99	0.0045	459

Fig. 5.20 indicates spatial and temporal histories of measured (normalized by $0.5\rho C^2$) pressure on the vertical plane at 0.05 m away from the centerline of the deck for the deck impingement wave condition. The figure was plotted with each panel located at the corresponding measurement point in Fig. 5.2(b). Fig. 5.21 depicts a detailed view over the peak pressure for each and every pressure variations on Fig. 5.20. Table 5.4 summarizes the magnitude of the maximum pressure, rise time and the gradient of the pressure rise for the pressure time histories given in Fig. 5.20.

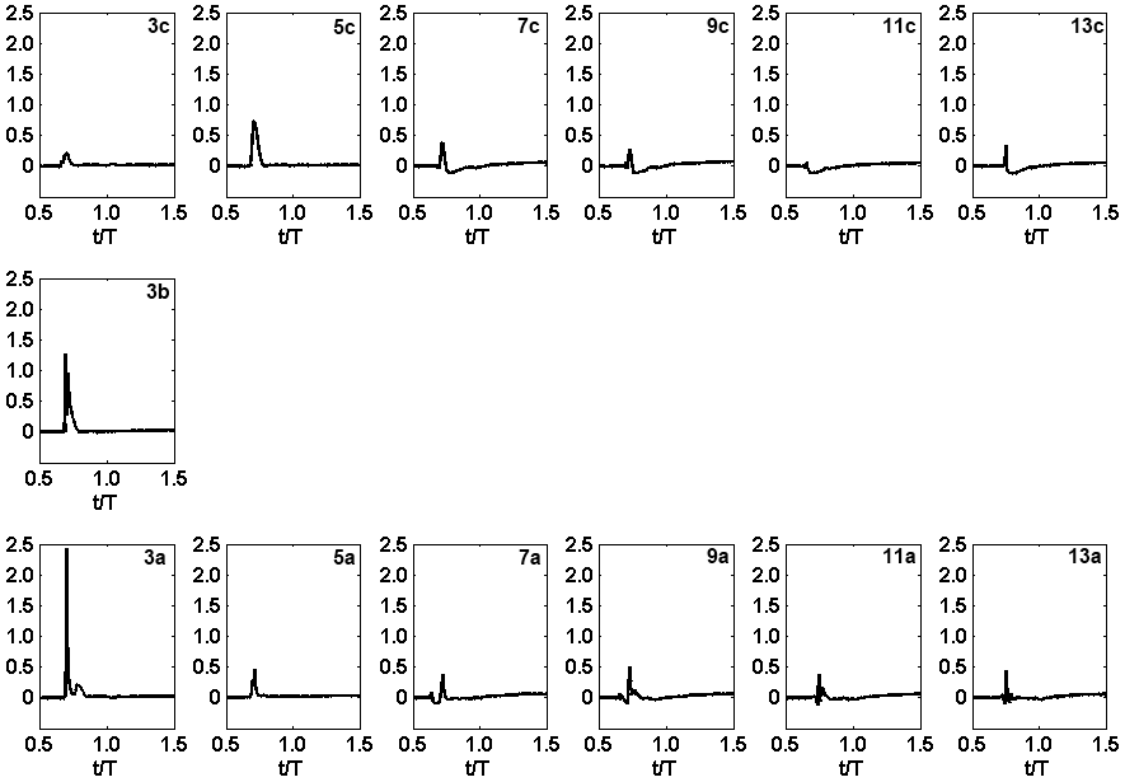

Fig. 5.20. Measured pressure (normalized by $\rho C^2 / 2$) against time (normalized by T) on the vertical plane 0.05 m away from the centerline of the deck surface for the deck impingement wave condition. The vertical axis is $\frac{P}{0.5\rho C^2}$. The panels are arranged in accordance to Fig. 5.2(b).

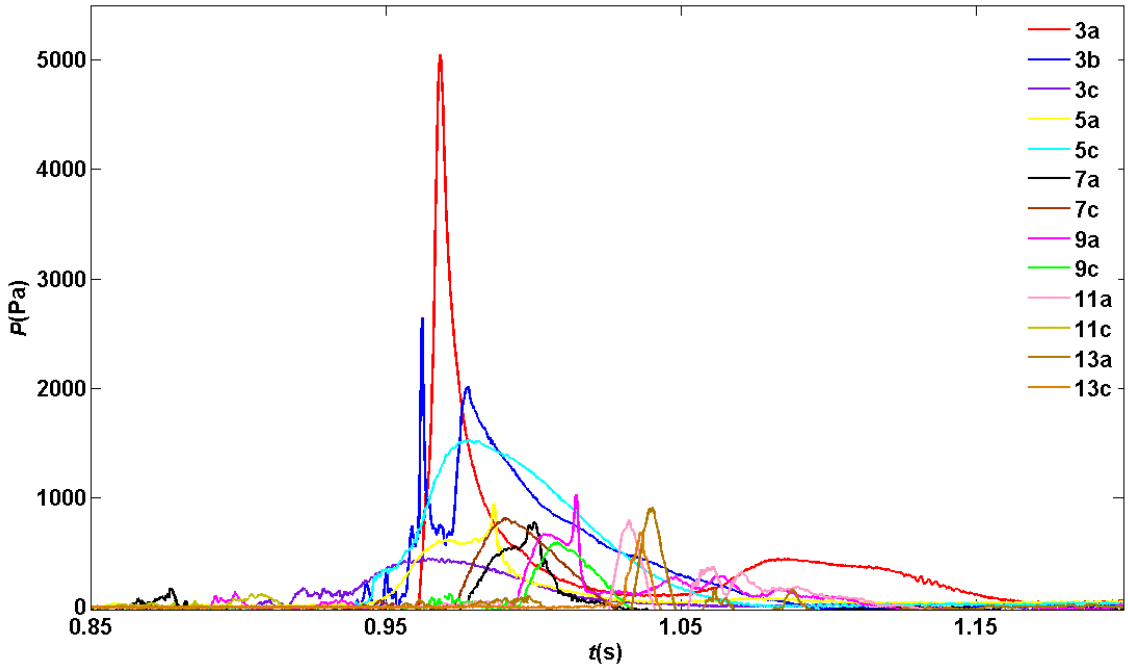

Fig. 5.21. Pressure time history for the vertical plane located at 0.05 m from the center of the deck for the deck impingement wave condition. The legend corresponds to the measurement points in Fig. 5.2 (b).

Table 5.4. Measured maximum pressure corresponding to Fig. 5.2(b). Pressure was normalized by $0.5\rho C^2$.

Location	Maximum pressure (Pa)	Normalized Maximum pressure	Rise time (s)	d*p*/d*t* (Pa/ms)
3a	5048	2.43	0.0073	689
3b	2642	1.27	0.0081	325
3c	456	0.22	0.0465	10
5a	947	0.46	0.0411	23
5c	1519	0.73	0.0374	41
7a	781	0.38	0.0249	31
7c	807	0.39	0.0176	46
9a	1027	0.49	0.0217	47
9c	593	0.28	0.0133	44
11a	796	0.38	0.0068	117
13a	909	0.44	0.0071	128
13c	683	0.33	0.0062	111

According to the experimental results given in Fig. 5.20, the maximum normalized pressure of 2.43 (normalized by $0.5\rho C^2$) or 5048 Pa (equivalent to 853 kPa in the prototype) occurred at point 3a located 0.10 m behind the front leading edge and 0.02 m above the deck surface. This location is very close to the location where the breaking wave impinges on deck surface. The magnitude of the peak pressure is higher than that observed at the centre, which agrees well with the measured velocity. Impulsive type pressure variations having pressure rise gradients above 250 Pa/ms were observed at locations close to the leading front edge of the model at 3a and 3b. Similar to the measured pressure at centre, the pressure near the deck surface is higher for all the points to that compared to the wall impingement wave. Similar to the measurement at centre indication of pressure was observed towards the very end of the deck. Similar to

the wall impingement wave, most of the pressure variations have a single peak with no oscillations.

Possibility of relating the peak impact pressure to the rise time has been investigated by several researchers such as Weggel and Maxwell (1970), Blackmore and Hewson (1984), Kirkgoz (1990), Hattori et al. (1994), and Cuomo et al. (2010). It was found that an upper envelope can be obtained for the individual peak pressure plotted against the rise time. Most of the researchers found that this relationship can be expressed in the form of,

$$P_{\max} = at_r^b \tag{5.2}$$

where, $p_{\max}$ is peak pressure, t_r is rising time, and *a* and *b* are coefficients.

A wide range of values for *a* and *b* were proposed (see Table 5.5). These variations are attributed to scale, type of fluid used, and definition of t_r etc. Although the value of coefficient *b* varies a lot, the value for coefficient *a* stays near unity.

Considering the measured pressure time histories for both the wall impingement and deck impingement wave conditions and for both vertical planes, the possibility of correlating peak pressure and rise time was examined. Based on the measurements, an envelope and a best fit curve were obtained and shown in Fig. 5.22. Even though there are some data scattering, with close examination it is possible to reveal that the high impact pressure peaks associate closely with the short rise time and vice versa. Since the above relationship is dimensional; it is difficult to compare the present results with the existing proposed equations.

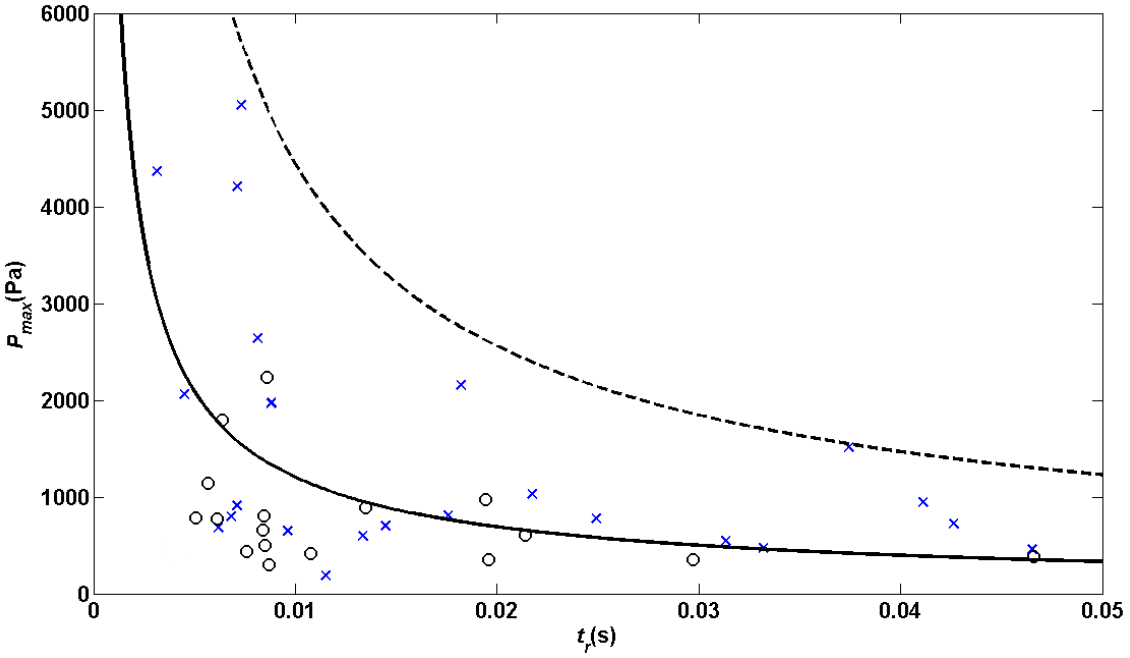

Fig. 5.22. Peak impact pressure, P_{max} variation with rise time, t_r. ○, wall impingement; ×, deck impingement; ▬ ▬ ▬, envelope 112 $t^{-0.80}$; ▬▬▬, curve fit 30 $t^{-0.80}$. R^2=0.22.

Table 5.5. Relationships of peak impact pressure and rise time.

Investigator	Equation	Equation in Pa and s	*a*	*b*
Cuomo et al. (2010)	$F_{\max} = 7t_r^{-0.60}$ $F_{\max}$ - [kN], t_r - [s]			
Hattori et al. (1994)	$P_{\max} = 400t_r^{-0.75}$ $P_{\max}$ - [gf/cm^2], t_r - [ms]	$P_{max} = 725.34t_r^{-0.75}$	725.34	-0.75
Kirkgoz (1990)	$P_{\max} = 25\times10^4 t_r^{-0.90}$ $P_{\max}$ - [Pa], t_r - [ms]	$P_{\max} = 1.3\times10^8 t_r^{-0.9}$	1.3×10^8	-0.90
Blackmore and Hewson (1984)	$P_{\max} = 3.1t_r^{-1.0}$ $P_{\max}$ - [kPa], t_r - [s]	$P_{\max} = 3.1\times10^{-3} t_r^{-1.0}$	3.1×10^{-3}	-1.00
Weggel and Maxwell (1970)	$P_{\max} = 0.0069t_r^{-1.0}$; steepness, $\frac{H_0}{T^2}$ =0.0589 $P_{\max} = 0.0033t_r^{-1.0}$; steepness, $\frac{H_0}{T^2}$ =0.2285 $P_{\max}$ - [lb/in^2], t_r - [s]	$P_{\max} = 1.0\times10^{-6} t_r^{-1.0}$ $P_{\max} = 4.8\times10^{-7} t_r^{-1.0}$	1.0×10^{-6} 4.8×10^{-7}	-1.00 -1.00

5.5. Relation between impact pressure and velocity

Fig. 5.23 shows the spatial and temporal variations of ensemble averaged void ratio for measurement locations for the wall impingement wave condition. The figure was plotted with each panel located at the corresponding measurement point as shown in Fig. 5.1. Table 5.6 summarizes the average void ratio for each void ratio variation for the present study and the available averaged void ratio for the 2D study by Ryu and Chang (2008).

As Fig. 5.23 depicts the void ratio fluctuates a lot at the locations near the leading front edge of the model. After about 0.05 m away from the leading front edge, the void ratio stays at a constant level over time. For the locations near the front of the model, the void ratio near the deck surface (at $Z = 0.02$ m) is lower than that at 0.07 m above the deck. This is compatible with the variations Ryu and Chang (2008) observed. Further, the void ratio is high near the front edge, and gradually decreases along the deck surface. As Table 5.6 shows for most of the measurement locations, the averaged void ratio lies around 0.4.

Table 5.6. Averaged void ratio for the wall impingement corresponding to Fig. 5.23.

Location	Averaged void ratio for 3D model	Averaged void ratio for 2D model (Ryu and Chang (2008))
1a	0.32	0.42
1c	0.42	0.65
2a	0.38	0.50
2c	0.48	0.63
3a	0.41	
3b	0.42	
3c	0.35	

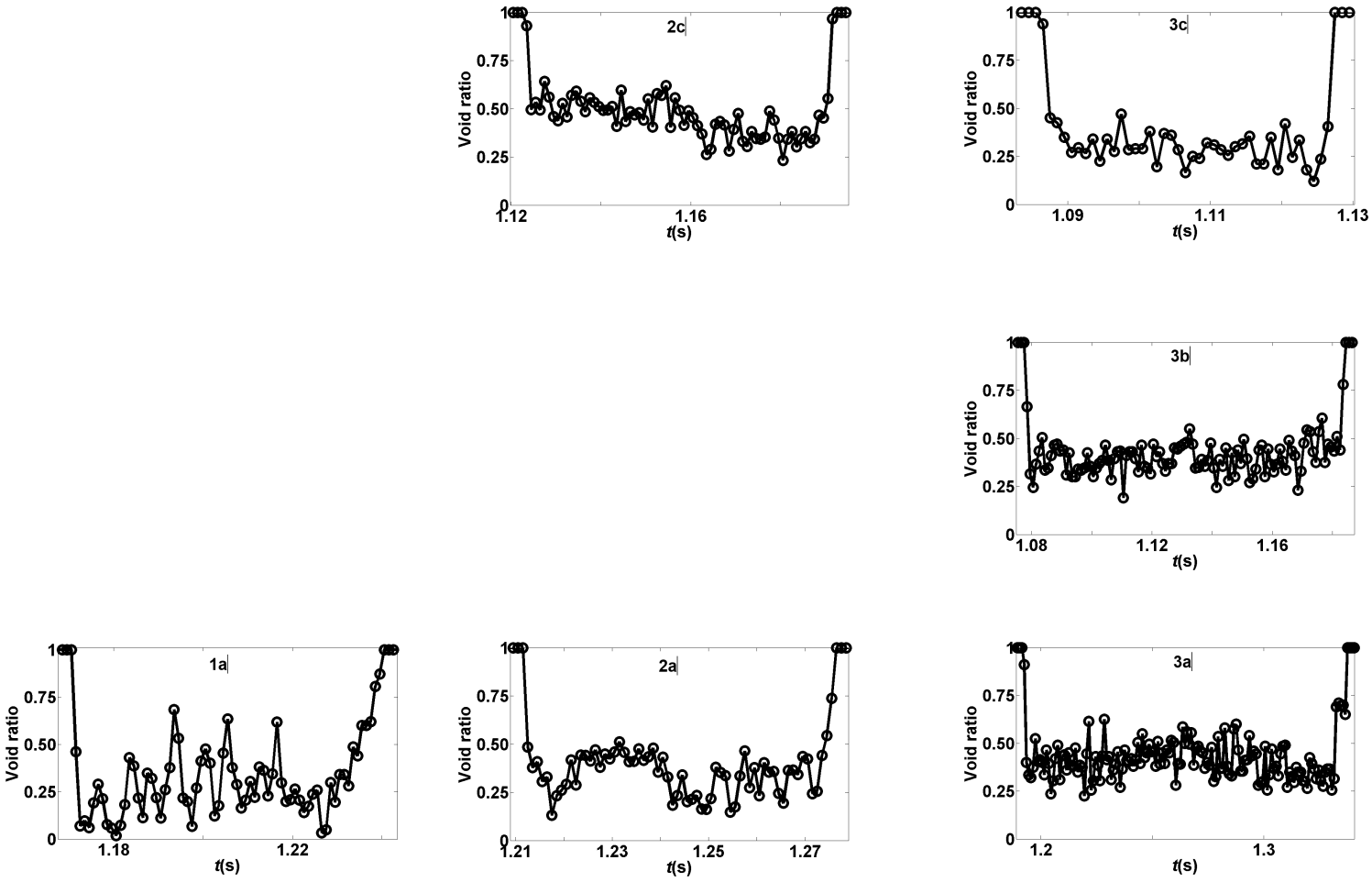

Fig. 5.23. Measured void ratio for the wall impingement wave condition. The panels are arranged in accordance to Fig. 5.1.

Fig. 5.24 shows the spatial and temporal variations of ensemble averaged void ratio for measurement locations for the deck impingement wave condition. The figure was plotted with each panel located at the corresponding measurement point as shown in Figure 5.2. Table 5.7 summarizes the average void ratio for each void ratio variation.

Similar to the wall impingement wave condition, as Fig. 5.24 depicts the magnitude of the void ratio scatters a lot. For deck impingement wave condition, the void ratio is higher near the deck surface compared to wall impingement wave. Similar to wall impingement wave the void ratio lies around a constant over time. Further, the void ratio is high near the front edge, and gradually decreases along the deck surface.

Table 5.7. Averaged void ratio for the deck impingement corresponding to Fig. 5.24.

Location	Averaged void ratio
1a	0.56
2a	0.63
2b	0.38
3a	0.44
3b	0.42
3c	0.61

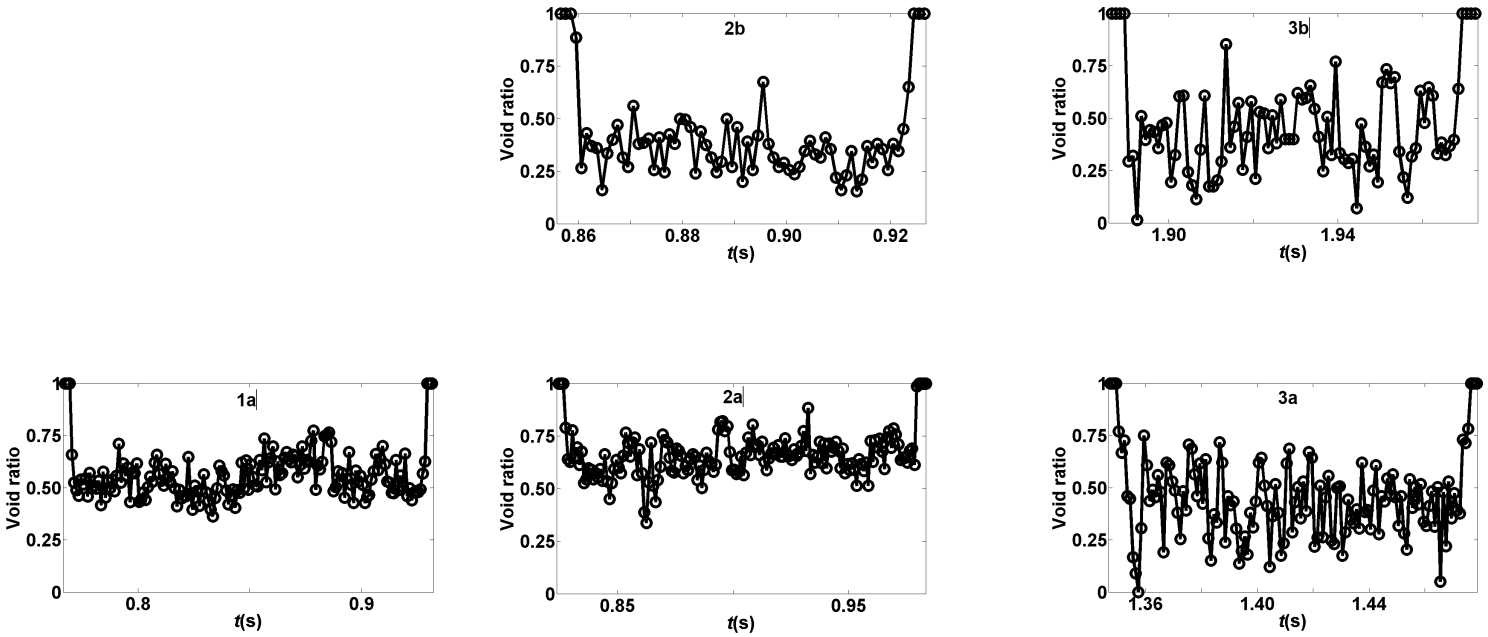

Fig. 5.24. Measured void ratio for the deck impingement wave condition. The panels are arranged in accordance to Fig. 5.2.

By examining the images and movies in the BIV velocity measurements, it was found that, for both wall impingement and deck impingement wave conditions, water flowing above the deck surface behaves like a water jet. The horizontal velocity becomes dominant once the flow reaches the deck level. Hence the green water impact phenomenon may have a considerable resemblance to a jet impinging perpendicularly at a plate. It is known that the peak pressure of a jet impinging on a plate perpendicularly may be formulated as

$$P = c_i \rho U^2 \qquad (5.3)$$

where P is pressure, c_i is called the impact coefficient, ρ is the fluid density, and U is the horizontal velocity. For example, based on empirical relations obtained from experiments Suhara et al. (1973) propose an impact coefficient c_i = 1.4.

The measured velocities and pressure in the present study were used to examine the relationship in Equation (5.3). However, the vertical-plane velocity measurements may suffer from the flow-blocking-camera problem after green water advanced onto the deck and deflected by the angled front of the 3D structure. To make sure the velocity measurements are coincident to the pressure measurements, only points selected near the leading front edge of the model were used in the examination. As a result, we only selected the two front most points to ensure that the velocity measurements correctly correspond to the exact measurement positions. Thus we only selected points 1, 2 and 3 at the elevations a, b, and c in Figs. 5.1 and 5.2.

Since the green water flow above the deck surface is a multi-phased flow, the fluid density may need to be corrected before applying Equation (5.3). Equation (5.3) is

applicable for a single-phased flow. In green water flow the fluid density needs to be corrected by introducing void fraction; i.e., the actual density becomes $(1-\alpha)\rho$. The equation can thus be rewritten as

$$P = c_i(1-\alpha)\rho U^2 \qquad (5.4)$$

in which α is the void fraction of the bubbly flow with α=0 indicating 100% water and α=1 indicating 100% air.

Since the pressure and horizontal velocity are both a function of time, we used the maximum pressure ($P_{\max}$) and maximum horizontal velocity (U_{max}) to estimate the impact coefficient c_i in Equation (5.4). This is based on the assumption that $P_{\max}$ occurs at the moment coincident to the occurrence of the maximum horizontal velocity U_{max} . This may not be always true since $P_{\max}$ should occur at the moment of maximum momentum $(1-\alpha)U^2$.

Fig. 5.25 shows the relation between $P_{\max}$ and $\rho U_{\max}^2$ for the wall impingement wave condition. The slope in the figure is c_i=0.74. The R^2 value is 0.87. Since for wall impingement wave, for the locations of void ratio measurements, the averaged void ratio lies around a constant value, $P_{\max}$ and $\rho U_{\max}^2$ has a good linear relation.

Fig. 5.26 shows the relation between $P_{\max}$ and $(1-\alpha)\rho U_{\max}^2$ for the wall impingement wave condition. The slope in the figure is c_i=1.28≈1.3, i.e.,

$$P_{\max} = 1.3(1-\alpha)\rho U_{\max}^2 \qquad (5.5)$$

The R^2 value in the fit is 0.94, indicating the relation is quite linear. The impact coefficient is very close to 1.4 reported in Suhara et al. (1973).

Relation between $P_{\max}$ and $(1-\alpha)\rho U_{\max}^2$ for the wall impingement wave condition using 2D measured void ratio is shown in Fig. 5.27. The slope in the figure is c_i =1.39≈1.4, i.e.,

$$P_{\max} = 1.4(1-\alpha)\rho U_{\max}^2 \tag{5.6}$$

The R^2 value in the fit is 0.89

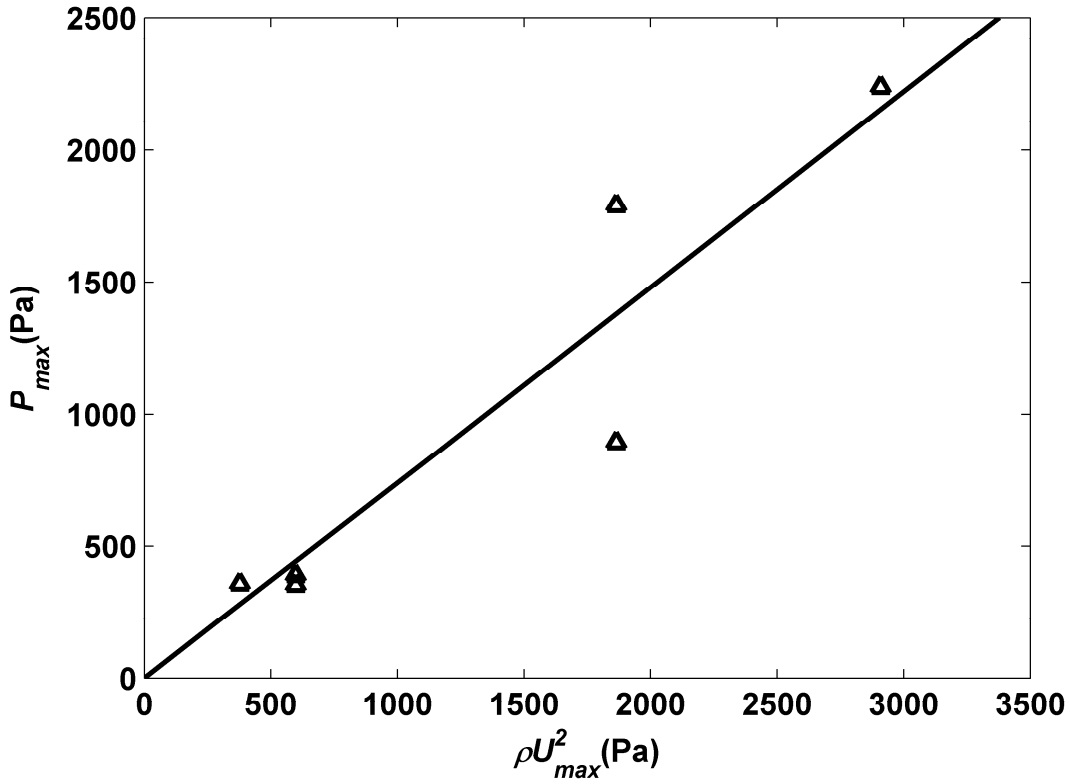

Fig. 5.25. $P_{\max}$ versus $\rho U_{\max}^2$ for the wall impingement wave condition. The slope in the fit is 0.74 and the R^2 value is 0.87.

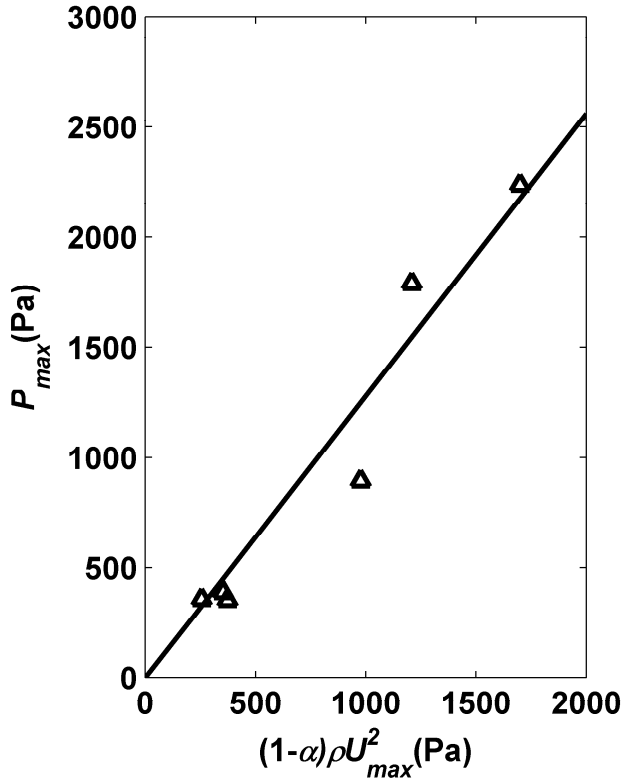

Fig. 5.26. $P_{\max}$ versus $(1-\alpha)\rho U^2_{\max}$ for the wall impingement wave condition. The slope in the fit is 1.28 and the R^2 value is 0.94.

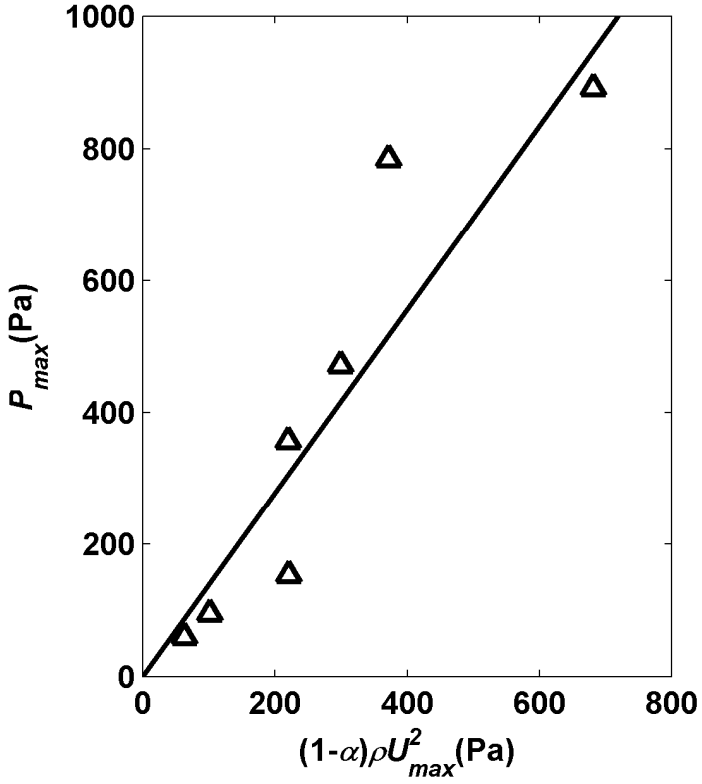

Fig. 5.27. $P_{\max}$ versus $(1-\alpha)\rho U_{\max}^2$ for the wall impingement wave condition using 2D measured void ratio. The slope in the fit is 1.39 and the R^2 value is 0.89.

Similar analysis was done considering the measurements for the deck impingement wave condition. See Fig. 5.28. However, for the deck impingement wave, it was not possible to obtain a simple linear variation for calculated pressure and measured pressure. It was observed that for wall impingement wave, most of the pressure variations were non impulsive. Hence a constant coefficient of c_i =1.28 exists. Where as, for the deck impingement wave, the measured pressure variations were impulsive for most of the locations. Hence the coefficient c_i is above 1.28 and varies from measurement point to point. Table 5.8 and Table 5.9 summarizes the calculated c_i for wall impingement wave and deck impingement wave respectively.

Table 5.8. Values of coefficient c_i for the wall impingement wave.

Location	P_{max} measured (Pa)	P_{max} calculated (Pa)	c_i
1a	357.37	255.29	1.40
2a	352.44	373.12	0.94
2c	893.95	976.97	0.92
3a	389.18	352.40	1.10
3b	2237.08	1699.39	1.32
3c	1790.12	1208.39	1.48

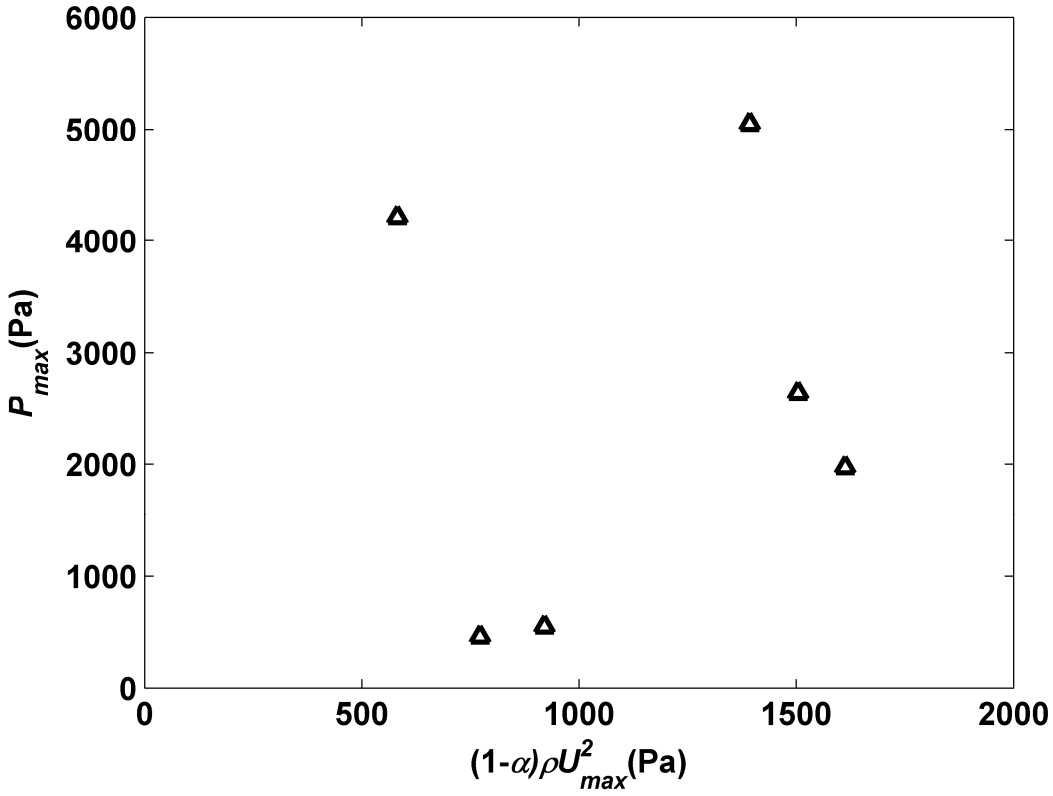

Fig. 5.28. $P_{\max}$ versus $(1-\alpha)\rho U_{\max}^2$ for the deck impingement wave condition.

Table 5.9. Values of coefficient c_i for the deck impingement wave.

Location	P_{max} measured (Pa)	P_{max} calculated (Pa)	c_i
1a	4213.02	582.07	7.24
2a	544.02	920.46	0.59
2b	1971.73	1612.67	1.22
3a	5047.87	1392.75	3.62
3b	2641.95	1503.89	1.76
3c	456.24	772.46	0.59

Chan and Melville (1988) summarized the typical range of impact coefficients based on their and others research work. The impact coefficients were calculated using the normalized peak pressure $P_m / \rho C^2$ and shown in Table 5.10. Plates and cylinders were used in the work, and only the water density was considered. As the table shows, the impact coefficient varies considerably between 0.5 and 40, even though the experimental setup is quite similar among the different studies.

In the present study, the maximum observed $P_m / \rho C^2$ is 0.44, based on the wall impingement case in Table 5.1. However, the observed pressure is unlikely to be the maximum pressure in the flow since the distribution of pressure measurement points is quite sparse in the present study, and therefore, the value of 0.44 is likely lower than the real value. In other words, the value of $P_m / \rho C^2$ must be greater than 0.44. Interestingly, all the lower bound values in Table 5.10 are greater than 0.44.

In Table 5.10, the phase speed *C* was used, not the maximum velocity U_{max} used in Equations (5.3-5.4). The void fraction effect on the fluid density is also not considered in the table. If we convert U_{max} in Equation (5.4) to *C* and approximate U_{max} by $1.2C$ for the wall impingement case as mentioned in Section 3.1, the impact coefficient would change from 1.28 to 1.84, i.e.,

$$P_{\max} = 2.0(1-\alpha)\rho C^2 \qquad (5.7)$$

The value 2.0 compares well with at least half of the studies in Table 5.10.

Similarly, for the deck impingement wave condition, if we convert U_{max} in Equation (5.4) to *C* and approximate U_{max} by 1.44C

The range of impact coefficient would change from 0.59-7.24 to 1.22-15. The range of values compare well with Table 5.10.

Table 5.10. Comparison of normalized peak pressure by Chan and Melville (1988).

Investigator	Typical range of peak pressure ($\frac{P_m}{\rho C^2}$)	Structure
Kjeldsen & Myrhaug (1979)	1-2	Vertical plate suspended above SWL (deep water)
Kjeldsen (1981)	1-3	Inclined plate suspended above SWL (deep water)
Ochi & Tsai (1984)	1.4	Surface-piercing cylinder (deep water)
Bagnold (1939)	11-40 (highest 90)	Surface-piercing plate on a sloping beach
Hayashi & Hattori (1958)	3-15	Surface-piercing plate on a sloping beach
Weggel & Maxwell (1970)	8-20 (highest 40)	Surface-piercing plate on a sloping beach
Kirkgoz (1982)	8-20	Surface-piercing plate on a sloping beach
Blackmore & Hewson (1984)	0.5-4	Seawall (prototype structure)
Chan & Melville (1984)	2-10	Surface-piercing cylinder (deep water)
Chan & Melville (1988)	3-10 (highest 21)	Surface-piercing plate (deep water)

Since it was observed that the value of coefficient c_i depends on whether the pressure variation is impulsive or non impulsive, the gradient of the pressure increase was plot against c_i. See Figure 5.29. As the Figure 5.29 depicts c_i and d*p*/*dt* have a linear relationship with R^2 value of 0.85.

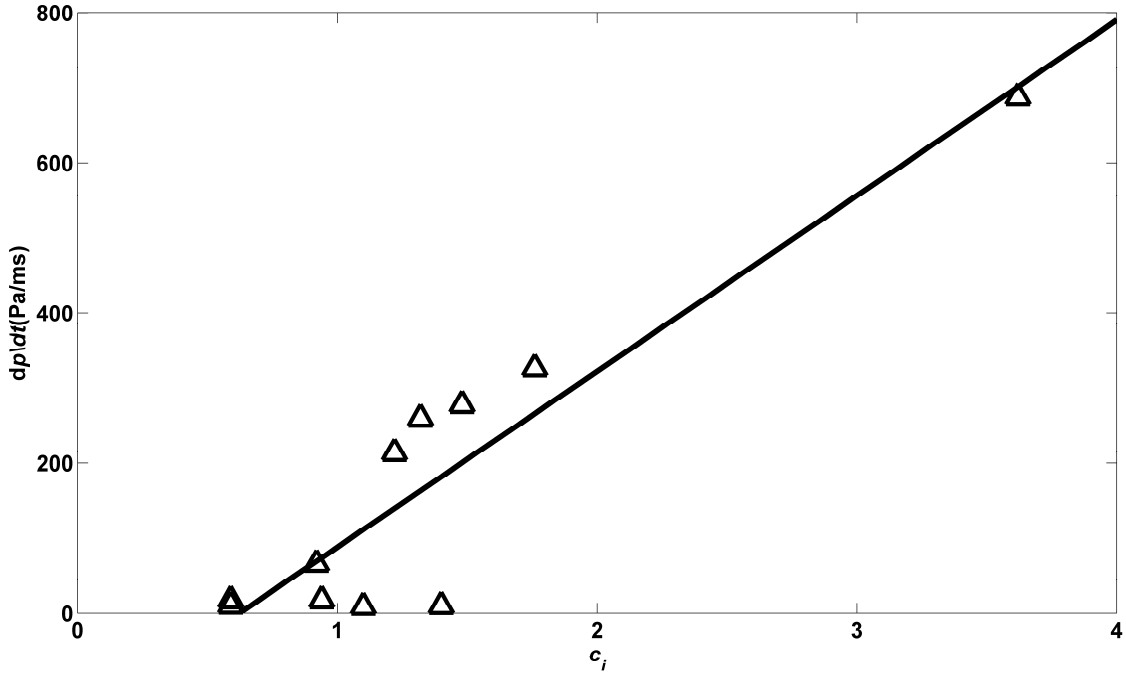

Fig. 5.29. Variation of $\frac{dp}{dt}$ versus c_i. R^2 value is 0.85.

CHAPTER VI

SUMMARY AND RECOMMENDATIONS FOR FUTURE STUDY*

6.1. Summary

The evolution and maximum velocities of green water flow on a three-dimensional structure were successfully measured in the laboratory using the BIV technique. Froude scaled waves based on the maximum wave condition in Hurricane Ivan were used in the experiment. Two wave conditions were tested: one with waves impinging on the vertical wall of the model at the still water level and the other with waves impinging on the horizontal deck surface. In order to obtain the three-dimensional features of the event, velocity measurements were made on both the vertical plane (side view) along the structure centerline and the horizontal plane (plan view) above the structure deck surface. Illumination in both measurement planes was carefully set up so the back-lit effect was controlled.

---

* Part of the data reported in this chapter is reprinted with permission from "Three-dimensional green water velocity on a model structure" by Chang, Ariyarathne and Mercier (2011). Experiments in Fluids, DOI: 10.1007/s00348-011-1051-0, Copyright [2011] Springer.

Some findings are summarized as follows:

(1) The maximum velocities in the green water flow occurred at the front of the flow. The finding is similar to what was observed by Ryu et al. (2007a) in two-dimensional model structure tests.

(2) Due to deflection of the flow by the front of the structure, the horizontal profile of the green water front had a bell shape. The velocity at the centerline was slightly greater than that immediately away from the centerline. This resulted in a protruding "water tongue" at the centerline in the wall impingement case.

(3) The deck impingement case resulted in a higher velocity above the deck in comparison to the wall impingement case. The maximum velocity was 1.44*C* in the deck impingement case with *C* being the phase speed of the breaking wave. That is 16% higher than that in the wall impingement case. However, the maximum elevation of splash-up in the deck impingement case was only 0.08 m above the deck level, approximately only one-half of the splash-up height in the wall impingement case.

(4) Based on observation made from the horizontal measurement plane, the maximum velocities were located near the outer edges of the structure in both the deck and wall impingement cases. In addition, based on observation made from the vertical measurement plane, the maximum velocities were not on the upper surface of the green water flow but beneath the surface.

(5) By comparing the present 3D results with the 2D measurement results in Ryu et al. (2007a), it was found that the maximum horizontal velocities are similar and close to 1.2*C*. However, the vertical velocities are quite different during the run-up stage. The

maximum observed vertical velocity was 1.7C in the present 3D study, whereas it reached 2.9C in Ryu et al.'s 2D study. The 2D study is therefore considered as a conservative condition.

(6) Three approaches were used to examine the applicability of dam-break theory to the prediction of green water velocity over the deck. Two are based on the deck exceedance (one at the dam and the other at far upstream) and the third one is based on matching the measured green water front velocity with the front velocity of the dam-break flow. The theory fails to predict the profile of green water, regardless the approaches. However, all three approaches give good engineering accuracy in predicting the maximum (i.e., front) green water velocity. Among the three dam-break flow approaches, the one matching the front velocity gives the most favorable and accurate prediction.

(7) Two types of pressure variations were observed: impulsive type, where the pressure rises instantaneously with low rising time and non-impulsive type, where pressure variation has a smooth bell shape. For the wall impingement wave, most of the pressure time histories have non-impulsive variations whereas for deck impingement wave most of the pressure histories are of impulsive type. Higher impact pressure was observed for deck impingement compared to wall impingement. Maximum impact pressure was successfully related to the rise time.

(8) Maximum impact pressure on the deck due to green water flow was found to be in the order of magnitude of $0.5\rho C^2$ with ρ being the density of water. If void fraction (α) is accounted for, the maximum pressure becomes highly correlated with the

kinetic energy $(1-\alpha)\rho U_{\max}^2$. For the wall impingement wave constant impact coefficient was found as 1.3. The impact coefficient changes to 2.0 if the maximum pressure is correlated with $(1-\alpha)\rho C^2$. How ever, for deck impingement wave a constant impact coefficient does not exist. It was found that the gradient of pressure rise is linearly related to the impact coefficient.

6.2. Recommendations for future study

In the present study the model was built using 1:169 Froude scale. A model with a larger scale would have given more accurate results, since with a larger scale the error due to scale effects will be less and results would be closer to reality.

In this study two plunging breaking waves were tested, and it was observed that the deck impingement wave could result in more adverse damages. In the future more detailed measurements of velocity, pressure and force are to be obtained for deck impingement wave.

In velocity measurements only the velocity near the wave front was successfully obtained using the BIV technique. PIV technique could be used to obtain the velocity at other areas, so a more complete velocity field could be acquired.

The model was kept stationary in this study, it will be more realistic if the model is allowed to have movements, and especially if surge, heave and pitch motions could be added.

In the present study pressure measurements were taken using a coarse grid, it will be better to have a grid with small gap in between the measurement locations, so the location of maximum pressure could be easily identified.

REFERENCES

Azarmsa, S.A., Yasuda, T., Mutsuda, H., 1996. Cause and characteristics of impact pressure exerted by spilling and plunging breakers on a vertical wall. Proceedings of the 25th International Conference on Coastal Engineering, ASCE, pp. 2442-2455, New York.

Bagnold, R.A., 1939. Interim report on wave-pressure research. Proceedings – Institution of Civil Engineers 12, 201-226.

Blackmore, P.A., Hewson, P.J., 1984. Experiments on full scale wave impact pressures. Coastal Engineering 8, 331-346.

Blenkinsopp, C.E., Chaplin, J. R., 2010. Bubble size measurements in breaking waves using optical fiber phase detection probes. Oceanic Engineering 35, 388-401.

Bredmose, H., Peregrine, D.H., Bullock, G. N., 2009. Violent breaking wave impacts. Part 2: modeling the effect of air. Journal of Fluid Mechanics 641, 389-430.

Buchner, B., 1995a. The impact of green water on FPSO design. Offshore Technology Conference, OTC 7698, pp. 45-57, Houston.

Buchner, B., 1995b. On the impact of green water loading on ship and offshore unit design. The 6th International Symposium on Practical Design of Ships and Mobile Units (PRADS 95), pp. 430-443, Seoul.

Buchner, B., 1996. The influence of the bow shape of FPSOs on drift forces and green water. Offshore Technology Conference, OTC 8073, pp. 389-400, Houston.

Buchner, B., 2002. “Green water on ship-type offshore structures” PhD thesis, Delft University of Technology, Netherlands.

Bullock, G.N., Crawford, A.R., Hewson, P.J., Walkden, M.J.A., Bird, P.A.D., 2001. The influence of air and scale on wave impact pressures. Coastal Engineering 42, 291-312.

Bullock, G.N., Obhrai, C., Peregrine, D.H., Bredmose, H., 2007. Violent breaking wave impacts. Part 1:results from large-scale regular wave tests on vertical and sloping walls. Coastal Engineering 54, 602-617.

Chan, E-S., 1994. Mechanics of deep water plunging-wave impacts on vertical structures. Coastal Engineering 22, 115-133.

Chan, E.S., Cheong, H.F., Tan, B.C., 1995. Laboratory study of plunging wave impacts on vertical cylinders. Coastal Engineering 25, 87-107.

Chan, E.S., Melville, W.K., 1984. Deep water breaking wave forces on surface piercing structures. Abstracts in depth, International Congress on Theoretical and Applied Mechanics, Denmark.

Chan, E.S., Melville, W.K., 1988. Deep-water plunging wave pressures on a vertical plane wall. Proceedings of Royal Society of London 417, 95-131.

Chang, K.-A., Lim, H.J., Su, C.B., 2002. A fiber optic Fresnel ratio meter for measurements of solute concentration and refractive index change in fluids. Measurement Science and Technology 13, 1962-1965.

Chang, K.-A., Lim, H.J., Su, C.B., 2003. Fiber optic reflectometer for velocity and fraction ratio measurements in multiphase flows. Review of Scientific Instruments 74, 3559-3565.

Chanson, H., Aoki, S., Maruyama, M., 2002. Unsteady air bubble entrainment and detrainment at a plunging breaker: dominant time scales and similarity of water level variations. Coastal Engineering 46, 139-157.

Chanson, H., Lee, J.F., 1997. Plunging jet characteristics of plunging breakers. Coastal Engineering 31, 125-141.

Chanson, H., Manasseh, R., 2003. Air entrainment processes in a circular plunging jet: void-fraction and acoustic measurements. Journal of Fluids Engineering 125, 910-921.

Cox, D.T., Ortega, J.A., 2002. Laboratory observations of green water overtopping a fixed deck. Ocean Engineering 29, 1827-1840.

Cox, D.T., Scott, C.P., 2001. Exceedance probability for wave overtopping on a fixed deck. Ocean Engineering 28, 707-721.

Cuomo, G., Allsop, W., Bruce, T., Pearson, J., 2010. Breaking wave loads at vertical seawalls and breakwaters. Coastal Engineering 57, 424-439.

Deane, G., 1997. Sound generation and air entrainment by breaking waves in the surf zone. Journal of Acoustical Society of America 102, 2671-2689.

Deane, G.B., Stokes, M.D., 2002. Scale dependence of bubble creation mechanisms in breaking waves. Nature 418, 839-844.

Duan, W.Y., Xu, G.D., Wu, G.X., 2009. Similarity solution of oblique impact of wedge-shaped water column on wedged coastal structures. Coastal Engineering 56, 400-407.

Faltinsen, O.M., Greco, M., Landrini, M., 2002. Green water loading on a FPSO. Journal of Offshore Mechanics and Arctic Engineering 124, 97-103.

Fekken, G., Veldman, A.E.P., Buchner, B., 1999. Simulation of green water loading using the Navier-Stokes equations. Proceedings of the 7th International Conference on Numerical Ship Hydrodynamics 6, pp. 3.1-3.12, Nantes.

Hamoudi, B., Varyani, K.S., 1998. Significant load and green water on deck of offshore unity/vessels. Ocean Engineering 25, 715-731.

Hattori, M., Arami, A., Takamasa, Y., 1994. Wave impact pressure on vertical wall under breaking waves of various types. Coastal Engineering 22, 79-114.

Hayashi, T., Hattori, M., 1958. Pressure of the breaker against a vertical wall. Coastal Engineering in Japan 1, 25-37.

Hull, P., and Muller, G., 2002. An investigation of breaker heights, shapes and pressures. Ocean Engineering 29, 59-79.

Khayyer, A., Gotoh, H., 2009. Modified moving particle semi-implicit methods for the prediction of 2D wave impact pressure. Coastal Engineering 56, 419-440.

Kirkgoz, M.S., 1982. Shock pressure of breaking waves on vertical walls. Journal of Waterways Port, Coastal and Ocean Division 108, 81-95.

Kirkgoz, M.S., 1990. An experimental investigation of a vertical wall response to breaking wave impact. Ocean Engineering 17, 379-391.

Kirkgoz, M.S., 1991. Impact pressure of breaking waves on vertical and sloping walls. Ocean Engineering 18, 45-59.

Kirkgoz, M.S., 1992. Influence of water depth on the breaking wave impact on vertical and sloping waves. Coastal Engineering 18, 297-314.

Kirkgoz, M.S., 1995. Breaking wave impact on vertical and sloping coastal structures. Ocean Engineering 18, 35-48.

Kjeldsen, S.P., 1981. Shock pressures from deep water breaking waves. International Symposium on Hydrodynamics, pp. 567-584, Norway.

Kjeldsen, S.P., Myrhaug, D., 1979. Breaking waves in deep water and resultant wave forces. In Proceedings of 11th Offshore Technology Conference, OTC 3646, pp. 2515-2522, Houston.

Kleefsman, K.M.T., Fekken, G., Veldman, A.E.P., Iwaanowski, B., Buchner, B., 2005. A volume-of-fluid based simulation method for wave impact problems. Journal of Computational Physics 206, 363-393.

Lamarre, E., Melville, W.K., 1992. Instrumentation for the measurement of void-fraction in breaking waves: laboratory and field results. Ocean Engineering 17, 204-215.

Lauber, G., Hager, W.H., 1998. Experiments to dam break wave: horizontal channel. Journal of Hydraulic Research 36, 291-307.

Lugni, C., Brocchini, M., Faltinsen, O.M., 2006. Wave impact loads: the role of the flip-through. Physics of Fluids 18, 122101-1-122101-17.

Mori, N., Chang, K-A., 2003. Introduction to MPIV. User manual and program available online at http://www.oceanwave.jp/softwares/mpiv/ (22 May 2011).

Mori, N., Cox, D.T., 2003. Dynamic properties of green water event in the overtopping of extreme waves on a fixed dock. Ocean Engineering 30, 2021-2052.

Mori, N., Suzuki, T., Kakuno, S., 2007. Experimental study of air bubbles and turbulence characteristics in the surf zone. Journal of Geophysical Research 112, C05014, doi:10.1029/2006JC003647.

Nielsen, K.B.T., Mayer, S., 2004. Numerical prediction of green water incidents. Ocean Engineering 31, 363-399.

Ochi, M.K., Tsai, C.H., 1984. Prediction of impact pressure induced by breaking waves on vertical cylinders in random seas. Applied Ocean Research 6, 157-165.

Pham, X.P., Varyani, K.S., 2005. Evaluation of green water loads on high-speed containership using CFD. Ocean Engineering 32, 571-585.

Ray, S.D., 2002. Applied Photographic Optics, Focal Press, Oxford, U.K.

Ritter A., 1892. Die fortpflanzung der wasserwellen. Vereine Deutscher Ingenieure Zeitswchrift 36(33), 947-954.

Rojas, G., Loewen, M.R., 2007. Fiber-optic probe measurements of void fraction and bubble size distributions beneath breaking waves. Experiments in Fluids 43, 895-906.

Ryu, Y., Chang, K-A., 2008. Green water void fraction due to breaking wave impinging and overtopping. Experiments in Fluids 45, 883-898.

Ryu, Y., Chang, K-A., Lim, H., 2005. Use of bubble image velocimetry for measurement of plunging wave impinging on structure and associated green water. Measurement Science and Technology 16, 1945-1953.

Ryu, Y., Chang, K-A., Mercier, R., 2007a. Runup and green water velocity due to breaking wave impinging and overtopping. Experiments in Fluids 43, 555-567.

Ryu, Y., Chang, K-A., Mercier, R., 2007b. Application of dam-break flow to green water prediction. Applied Ocean Research 29, 128-136.

Schonberg, T., Rainey, R.C.T., 2002. A hydrodynamic model of green water incidents. Applied Ocean Research 24, 299-307.

Shigematsu, T., Liu, P.L.F., Oda, K., 2004. Numerical modeling of the initial stages of dam break waves. Journal of Hydraulic Research 42, 183-195.

Suhara, T., Hiyama, H., Koga, Y., 1973. Shock pressure due to impact of water jet and response of elastic plates. Transactions of West-Japan Society of Naval Architects No 46, 151-161.

Wan, D.C., Wu, G.X., 1999. The numerical simulation of the green water effect. Proceedings of 14th International Workshop on Water Waves and Floating Bodies, pp151-154, Michigan.

Wang D.W., Mitchel, D.A., Teague, W.J., Jarosz, E., Hulbert, M.S., 2005. Extreme waves under Hurricane Ivan. Science 309, 896.

Weggel, J.R., Maxwell, H.C., 1970. Numerical model for wave pressure distributions. Journal of Waterways, Harbors and Coastal Engineering Division 96, 623-642.

Wienke, J., Oumeraci, H., 2005. Breaking wave impact force on a vertical and inclined slender pile-theoretical and large-scale model investigations. Coastal Engineering 52, 435-462.

Xu, L., Barltrop, N., 2008. Bow impact loading on FPSOs 2-Theoretical investigation. Ocean Engineering 35, 1158-1165.

Xu, L., Barltrop, N., Okan, B., 2008. Bow impact loading on FPSOs 1-Experimental investigation. Ocean Engineering 35, 1148-1157.

Yilmaz, O., Incecik, A., Han, J.C., 2003. Simulation of green water flow on deck using non-linear dam breaking theory. Ocean Engineering 30, 601-610.

Zhou, D., Chan, E-S., and Melville, W.K., 1991. Wave impact pressures on vertical cylinders. Applied Ocean Research 13, 220-234.

VITA

Name:	Hanchapola Appuhamilage Kusalika Suranjani Ariyarathne
Address:	CE/TTI 808-C, 3136 TAMU, College Station, TX 77843-3136
Email Address:	kusalika@yahoo.com
Education:	B.S., Civil Engineering, University of Peradeniya, Sri Lanka, 2001
	M.S., Oceanography, University of Peradeniya, Sri Lanka, 2005
	M.S., Civil Engineering, Texas A&M University, 2007
	Ph.D., Civil Engineering, Texas A&M University, 2011